

# **Irradiation-induced crystal defects in silicon carbide**

**Ph.D. Thesis**

**Zsolt ZOLNAI**

**Supervisor: Dr. Tivadar LOHNER**

Research Institute for Technical Physics and Materials Science of the  
Hungarian Academy of Sciences, MTA MFA

**University consultants: Prof. Péter DEÁK  
Dr. György HÁRS**

Budapest University of Technology and Economics  
Department of Atomic Physics, BUTE DAP

**MTA MFA – BUTE DAP**

**2005**

# Contents

<b>1</b>	<b>Introduction to SiC.....</b>	<b>1</b>
1.1	The brief history of SiC.....	1
1.2	Applications of SiC – a short overview.....	1
1.2.1	SiC – a widely used material.....	1
1.2.2	Wide bandgap semiconductors.....	2
1.2.3	SiC for microelectronics applications.....	3
1.3	Crystal Structure and Polytypism.....	4
1.4	Production and doping of SiC single crystals.....	7
1.4.1	Bulk growth of SiC.....	7
1.4.2	Epitaxial growth of SiC.....	7
1.4.3	Growth of different polytypes.....	8
1.4.4	Doping of SiC by ion implantation.....	8
<b>2</b>	<b>Point defects in SiC.....</b>	<b>11</b>
2.1	Classification of point defects.....	11
2.2	Shallow and deep levels.....	12
2.3	Defect charge states and formation energies.....	13
2.4	The role of deep levels.....	15
2.5	Electron irradiation.....	16
<b>3</b>	<b>Principles of EPR and related techniques.....</b>	<b>19</b>
3.1	A magnetic moment in magnetic field.....	19
3.2	The principle of EPR.....	21
3.3	Spin relaxation.....	23
3.4	The effective spin Hamiltonian.....	25
3.4.1	Spin-orbit coupling.....	26
3.4.2	Fine structure.....	26
3.4.3	Hyperfine interaction.....	27
3.4.4	The effective spin Hamiltonian formalism.....	28
3.4.5	Symmetry properties.....	29
3.4.6	Experimental details.....	31
3.5	Photo-EPR.....	32
3.6	Photoluminescence.....	34
<b>4</b>	<b>EPR of irradiation-induced point defect centers in 4H-SiC.....</b>	<b>36</b>
4.1	Annealing behavior of the carbon vacancy in electron-irradiated 4H-SiC.....	37
4.1.1	Introduction.....	37

4.1.2 Experimental details.....	39
4.1.3 Results and discussion.....	39
4.1.4 Conclusions.....	43
4.2 The carbon vacancy-carbon antisite pairs in electron-irradiated 4H-SiC.....	44
4.2.1 Introduction.....	44
4.2.2 Results and discussion.....	44
4.2.3 Conclusions.....	50
4.3 Silicon vacancy related $T_{V2a}$ center in 4H-SiC.....	51
4.3.1 Introduction.....	51
4.3.2 Experimental details.....	52
4.3.3 Results and discussion.....	52
4.3.4 Conclusions.....	56
<b>5 Ion implantation.....</b>	<b>57</b>
5.1 Nuclear energy loss and defect formation.....	57
5.2 Channeling in the crystal.....	60
5.3 Dechanneling by defects.....	62
5.4 Electronic energy loss.....	64
<b>6 Profiling crystal defects by Ion Backscattering Spectrometry combined with Channeling (BS/C).....</b>	<b>66</b>
6.1 Accelerator, scattering chamber, and detector system.....	66
6.2 Backscattering spectrometry/channeling.....	68
6.2.1 Kinematic factors: qualitative analysis.....	68
6.2.2 Stopping power: depth profiling.....	70
6.2.3 Differential cross-sections: quantitative analysis.....	70
6.2.4 Straggling, multiple scattering and doppler broadening: limits in depth resolution.....	73
6.3 Disorder analysis.....	74
<b>7 BS/C Studies on ion-implanted SiC.....</b>	<b>77</b>
7.1 Damage accumulation in 4H-SiC induced by 3.5 MeV He ions during Backscattering Spectrometry/Channeling (BS/C) measurements.....	78
7.1.1 Introduction.....	78
7.1.2 Experimental details.....	78
7.1.3 Results and discussion.....	79
7.1.4 Conclusions.....	82
7.2 Investigation of aluminum implantation induced damage in the silicon and carbon sublattices of 6H-SiC.....	83

7.2.1 Introduction.....	83
7.2.2 Experimental details.....	83
7.2.3 Results and discussion.....	84
7.2.4 Conclusions.....	87
7.3 The influence of crystallographic orientation and ion fluence on damage accumulation in nitrogen implanted 6H-SiC.....	88
7.3.1 Introduction.....	88
7.3.2 Experimental details.....	88
Results and discussion.....	90
7.3.3 BS/C spectra.....	90
7.3.4 Electronic stopping power for channeled high-energy light ions in SiC.....	93
7.3.5 Disorder profiles.....	95
7.3.6 Computer simulation of damage accumulation.....	96
7.3.7 Disorder accumulation on the basis of the direct-impact, defect-stimulated amorphization model.....	99
7.3.8 Reducing the damage by channeling and annealing.....	101
7.3.9 Conclusions.....	105
<b>Summary.....</b>	<b>106</b>
<b>Utilization of the new scientific results.....</b>	<b>108</b>
<b>List of publications.....</b>	<b>109</b>
<b>Number of independent citations.....</b>	<b>111</b>
<b>Appendix 1: Data evaluation in electron paramagnetic resonance.....</b>	<b>112</b>
<b>Appendix 2: Mechanisms of irradiation-induced amorphization in ceramics: the direct- impact, defect-stimulated (D-I/D-S) amorphization model for SiC.....</b>	<b>115</b>
<b>References.....</b>	<b>117</b>
<b>List of used acronyms.....</b>	<b>125</b>
<b>Acknowledgements.....</b>	<b>126</b>

## **Preface**

Nowadays electronics have a major impact on everyday life and today's society. The beginning of the modern electronics technology goes back to the invention and elaboration of the semiconductor-based transistor by Bardeen and Brattain [P.1] and by Shockley [P.2] in 1948. Thereafter electronics industry has grown and become one of the world's largest. The increasing demands for smaller electronic devices with improved performance at lower costs drive the conventional silicon-based technology to its limits. To satisfy the requirements from the industry and to extend the applications of semiconductor devices, new materials and fabrication techniques have to be used.

At an early stage germanium (Ge) was mainly used as the semiconductor material, but eventually silicon (Si) achieved lead in semiconductor processing due to the relative ease to produce high quality crystals. Later, in the 1960s, compound semiconductors, such as III-V materials, like gallium arsenide (GaAs) were intensively studied for the use in microwave and optoelectronic applications. Since the 1980s the interest in the development of wide bandgap materials has increased drastically, as their unique physical properties make them very attractive for high-temperature, high-power and high frequency application fields, where the requirements are beyond the limits of Si or GaAs technology. One of the most promising wide bandgap semiconductors for such an application is silicon carbide (SiC) with exceptional material properties, like high-electron mobility, high-breakdown field, high saturated electron-drift velocity and high thermal conductivity [P.3]. Beyond microelectronics applications, the small cross-section for interaction with neutrons, low activation under neutron irradiation and good thermal conductivity lead to its potential use in structural components for fusion reactors [P.4], and as cladding material for gas-cooled fission reactors [P.5].

Due to continuous improvement in crystal growth techniques and experimental methods in the investigation of crystalline materials, as well as in theoretical work based on modern physics and high computational power, the science of semiconductors has grown to an enormous size and has reached a state of maturity. However, still many material-related issues have to be solved before new alternatives can compete in the market. A number of problems in the development of any crystalline semiconductor material are tightly connected with the understanding of defects in the material. Defects can trap free carriers, influence carrier generation and recombination and reduce the carrier lifetime, or act as scattering centers to limit the mobility. Usually defects are associated with harmful effects on device operation, but this is not always the case – low lifetimes are sometimes required for fast-switching diodes, and also, semi-insulating material for substrate applications is impossible to realize without deep level defects.

Defects can be found already in as-grown crystals, but are also formed during common device processing steps, such as ion implantation, irradiation and etching. They can migrate and anneal at high temperatures, or sometimes can transform into complexes. The examples above obviously confirm the general importance of defect studies.

Each semiconductor possesses a variety of atomic size point defects associated with it, each with unique properties found only for that particular material. In case of SiC, because of the binary compound nature and its crystalline structure giving rise to different inequivalent lattice sites a large variety of defects exist in the material. The large number of possible configurations makes defect studies rather complicated. To date only few point defect centers

have been unambiguously identified in SiC using the combination of different electrical, magnetic, and spectroscopic techniques like deep level transient spectroscopy (DLTS), electron paramagnetic resonance (EPR) or photoluminescence (PL). Therefore the investigation of electronic and magnetic properties of point defects in SiC in order to understand their role in device operation is one of nowadays' state of the art topics [P.3, P.6].

Contrary to the conventional Si-based semiconductor processing, the doping of SiC cannot be performed by thermal diffusion because of very low diffusion coefficients of dopants [P.7]. Considerable thermal diffusion can be achieved only above 2000 °C that is close to the decomposition and phase transition temperature for SiC. Due to this limitation nowadays ion implantation to high fluences is the only accessible selective doping technique for SiC. However, this technological process leads to the formation of structural defects. In this case different disorder accumulation processes take place depending on the implantation conditions, like ion mass, fluence, fluence rate, temperature, and the orientation of the ion beam with respect to the crystallographic axes of the semiconductor. The understanding of the irradiation-induced crystalline-to-amorphous phase transition of SiC and its possible recrystallization by post-implantation annealing is of major concern [P.8]. The main goal is to minimize the amount of ion implantation-induced defects at a certain fluence of dopant atoms.

The aim of this thesis is to provide more understanding on electron and ion irradiation-induced defects in SiC.

My results are divided into two parts. The first part deals with primary point defects, induced by MeV energy electron irradiation into SiC. In this case, due to the low energy transferred by the bombarding electrons to the target nuclei the role of cascade processes in defect formation is negligible. Finally a variety of single point defects of low concentration are formed in a large volume of the sample. Some of these defects bonds unpaired electrons, giving rise to paramagnetic ground states that can be excited under external magnetic fields using a microwave source for excitation. The first part of the thesis reports on magnetic properties and thermal stability of vacancy- and antisite-related defects in 4H-SiC investigated by continuous-wave X-band electron paramagnetic resonance (EPR) and photo-excitation-induced electron paramagnetic resonance (photo-EPR) techniques. I have done the major part of this work at the Institute of Physics and Measurement Technology (IFM) at Linköping University in Sweden thanks to the opportunity to work there one year via the EU program Marie Curie Training Sites.

The second part of the thesis summarizes my studies on ion implantation-induced disorder formation in SiC. During the implantation of heavier ions with energy of the order 100 keV, energy deposition into the nuclear subsystem of the target leads to the formation of atomic collision cascades. The realization of device applications often requires implantation to considerable high fluences that is accompanied by cascade-overlap. These processes increase the probability to form extended defects besides the accumulation of single point defects. If the implantation is performed along low index crystallographic directions, ion channeling occurs resulting in deeper dopant penetration and lower defect generation. Therefore, harmful damaging effects can be suppressed by mean of channeling. The shape of the ion profiles obtained by channeling implantation is very sensitive to the implantation fluence due to ion-damage scattering processes. The details of the formation of damage in

SiC, especially for channeling implantation conditions, is thus of considerable technological, as well as scientific, interest.

In the second part of this work, the disorder accumulation in function of the fluence and the orientation of the implanted ions with respect to the  $\langle 0001 \rangle$  axial direction of SiC is discussed. A widely used experimental technique to measure the implantation-induced disorder in crystalline solids is Rutherford Backscattering Spectrometry in combination with channeling technique (RBS/C). Usually the method operates with a  $^4\text{He}^+$  analyzing ion beam in the energy range 1-2 MeV. In conventional RBS/C the Rutherford cross-section of He ions for the target C atoms is about 7 times lower than for the target Si atoms, and therefore only the Si sublattice of SiC can be investigated. In this thesis a unique case of the technique is applied: 3.5 MeV  $^4\text{He}^+$  ion backscattering in combination with channeling (BS/C). At this energy the cross-section for C exceeds the Rutherford value by about a factor of 6, and therefore the method yields information simultaneously from both the Si and C sublattices of SiC with good sensitivity and good depth resolution for quantitative analysis of the depth distribution of disorder.

In my BS/C studies on SiC, firstly the disorder accumulation, caused by the analyzing  $^4\text{He}^+$  beam itself has been followed, and the measurement fluence and fluence rate were optimized to avoid artifacts during BS/C measurements. Ion implantation has been performed with 500 keV  $\text{N}^+$  and with 200 keV  $\text{Al}^+$  ions, which are commonly used n- and p-type dopants in SiC. Ion irradiation and BS/C measurements were performed using the Heavy Ion Cascade Implanter and the 5 MV EG-2R Van de Graaff accelerator at the Research Institute for Technical Physics and Materials Science and at the Research Institute for Particle and Nuclear Physics of the Hungarian Academy of Sciences in Budapest, Hungary.

This Ph.D. thesis is organized as follows:

Chapter 1 gives an introduction to the fundamental physical properties, the production and application power of SiC. This is followed by a brief summary describing the main features of atomic size defects in the material (Chapter 2). Defect formation during electron irradiation is also discussed here.

In Chapter 3, the principle of electron paramagnetic resonance (EPR) and related optical and magnetic resonance defect characterization techniques are discussed. This is followed by my EPR studies on the carbon vacancy ( $V_C$ ) related EI5 and EI6, the carbon vacancy-carbon antisite ( $V_C\text{-C}_{\text{Si}}$ ) related P6/P7 and the silicon vacancy ( $V_{\text{Si}}$ ) related  $T_{V2a}$  paramagnetic defect centers in SiC (Chapter 4).

Chapter 5 gives an introduction to ion-solid interactions and damage formation processes during ion implantation. The channeling phenomenon in crystalline structures is also discussed here. Chapter 6 deals with the BS/C experimental technique, particularly at 3.5 MeV  $^4\text{He}^+$  energy. Finally, in Chapter 7 the results of my 3.5 MeV  $^4\text{He}^+$  BS/C analysis on He-Al- and N-implanted SiC are summarized.

# Chapter 1

## Introduction to SiC

### 1.1 The brief history of SiC

Silicon carbide was first observed in 1824 by the Swedish scientist, Jöns Jacob Berzelius [1.1] in an attempt to synthesize diamond, while naturally occurring SiC has been discovered by Henri Moissan in 1905, who found small hexagonal platelets in a meteorite [1.2]. The mineral is now called Moissanite in his honor, and this has also become the name of commercial gemstones made from SiC. However, SiC is very rare in nature and has not been found freely yet, this is probably one cause of its relatively late discovery. The history of man-made SiC starts in 1891, when Acheson produced SiC in an electric melting furnace, mainly for grinding and polishing purposes [1.3]. Later, in the 1950s, when research on solid-state electronic devices has started, SiC was one of the semiconductor materials studied. In 1955 Lely [1.4] introduced a crystal growth technique to produce high quality bulk SiC, but the problem of producing large-area defect-free single crystals has not been solved, making device fabrication impossible. Later, in 1978 the so-called seeded sublimation epitaxy or modified Lely method was developed by Tairov and Tsvetkov [1.5], advancing the research field. Recently the most commonly used technique for epitaxial growth of SiC is the vapor-phase epitaxy (VPE) method usually realized in a chemical vapor deposition (CVD) reactor.

Due to the increased interest that SiC received, series of conferences was introduced, such as the International Conferences on Silicon Carbide and Related Materials (ICSCRM) and the European Conferences on Silicon Carbide and Related Materials (ECSCRM). The rapid growth in SiC research is reflected in the number of contributions, which increased from 28 at the first ICSCRM conference held in Washington, D.C. in 1987 (by that time called as First International Conference on Amorphous and Crystalline Silicon Carbide and Related Materials) to 430 at the latest one in Lyon, France 2003, making this conference the largest meeting of its kind worldwide.

### 1.2 Applications of SiC – a short overview

#### *1.2.1 SiC – a widely used material*

The excellent material qualities of SiC result in a great potential in applications. Before the emergence of microelectronics applications based on SiC, the attention was given mainly to its unique mechanical properties (for data see Table 1.1), so in the beginning SiC was used as an abrasive in sand paper, in polishing agents or in cutting tools. SiC is one of the hardest materials known to man, only diamond and boron nitride (with Mohs hardness of 9.5) are harder. The short bond length of 1.89 Å between Si and C atoms result in high bond strength and excellent hardness. However, this makes SiC wafers difficult to cut and polish. The strong bonds do also create a large bandgap that gives SiC's high refractive index accompanied by a broad transparency over the visible spectrum, optical brilliance, and resistance to chemical and abrasive attack. Recently high-purity, almost colorless Moissanite crystals become available, leading to the development of SiC gemstone industry that should have a beneficial influence on SiC semiconductor industry in the future [1.6].



Due to relatively low density, SiC can be used even in space applications, e.g. for ultra-lightweight mirrors [1.7]. It is also appropriate for bearings with the hardness and toughness [1.8]. SiC possesses extreme thermal stability and sublimates at 2830 °C while stoichiometric melting occurs just above 3200 °C under 100000 atm pressure. It does also conduct heat as well as copper and three times better than Si. In addition, excellent high-temperature fracture, creep, corrosion and thermal shock resistance as well as safety advantages arising from low induced radioactivity under neutron irradiation favoring the selection of SiC fiber/SiC composites for fusion power plant applications [1.9]. In the ITER (International Thermonuclear Experimental Reactor) project SiC is a promising candidate to withstand high temperature harsh environments as first wall cladding material [1.10].

### **1.2.2 Wide bandgap semiconductors**

In addition to the wide range applications of SiC described above, recently the most promising area is semiconductor processing.

Generally, semiconductors are classified by their electrical conductivity at room temperature, which varies in the range of  $10^{-9}$ – $10^3$  ( $\Omega\text{cm}$ )<sup>-1</sup> [1.11]. The width of the bandgap ( $E_g$ ) is another characteristic property. For semiconductors the bandgap is usually between a few tenths of eV up to 2-3 eV. Materials with larger bandgap are generally considered as insulators, however, the limit is not very sharp, and several semiconductors have bandgap energies well above 3 eV. These materials are called wide bandgap semiconductors, and include, for example, SiC ( $E_g = 2.3$ – $3.2$  eV), diamond ( $E_g = 5.5$  eV), some of the III-nitrides, such as GaN ( $E_g = 3.4$  eV) or AlN ( $E_g = 6.2$  eV), or some of the II-VI compounds like ZnS ( $E_g = 3.6$  eV).

The wide bandgap materials are in many respects superior to silicon due to their physical and electrical properties. Table II shows some characteristic properties of different wide bandgap semiconductors, selected from the viewpoint of microelectronics applications. Silicon and GaAs are also included for comparison. Having a large bandgap (2.3–6.2 eV), it is much more difficult to thermally excite electrons from the valence band to the conduction band. For example in SiC the probability of thermal excitation of an electron over the bandgap is  $10^{-26}$  at room temperature, i.e. there are no thermally excited electrons in the conduction band. In a device this causes the reduction in leakage currents and an increase in thermal stability since intrinsic-type conduction will dominate at higher temperatures (When it happens the devices fail, since there is no longer p-n junction to block the voltages.). The wide bandgap is also accompanied by considerably higher breakdown voltage as compared to silicon. This means that for power devices with similar blocking voltage capabilities, the one made of silicon must have about 100 times lower doping level in a 10 times thicker layer, as compared to a SiC device. Thick layers with low doping levels will have high resistance, increasing the power loss and heat generation in the device. Therefore, the use of wide bandgap materials, like SiC, gives the possibility to increase the blocking voltages for high power devices, as well as to make devices smaller and to reduce power losses. For switching devices, the high saturation drift velocity of carriers in combination with the high breakdown voltage, makes the wide bandgap semiconductors superior to most of the common semiconductor materials when it comes to impedance matching, output power and switching loss. As the power losses are much lower than in silicon, and the thermal conductivity and thermal stability are much higher, the need for surrounding cooling system is reduced. Thus, in summary, products using wide bandgap electronic devices can be made much smaller and much more efficient.

Property	Si	GaAs	4H-SiC	6H-SiC	2H-GaN	2H-AlN	Diamond
Bandgap at 300 K (eV)	1.11	1.43	3.26	3.02	3.39	6.2	5.45
Lattice parameters (Å)	5.43	5.65	a = 3.08 c = 10.08	a = 3.08 c = 15.12	a = 3.19 c = 5.18	a = 3.11 c = 4.98	3.56
Max. operating temp. (°C)	350	460	1200	1200			1100
Melting point (°C)	1410	1240	Sublimes > 2800	Sublimes > 2800		2275	Graphitization > 1500
Electron mobility ( $10^{-4}$ m <sup>2</sup> /Vs)	1400	8500	900	600	900	1100	2200
Hole mobility ( $10^{-4}$ m <sup>2</sup> /Vs)	600	400	40	40	150		1600
Breakdown electric field ( $10^8$ V/m)	0.3	0.4	2.2	2.5	3.3	11.8	10
Thermal cond. (W/m K)	150	54	490	490	130	200	2000
Saturation drift velocity ( $10^5$ m/s)	1.0	2.0	2.7	2.0	2.9	1.8	2.7
Dielectric constant	11.8	12.8	10	9.7	8.9	8.5	5.5
Mohs hardness	7	4-5	9.2-9.3				10

**Table 1.1** Properties of some wide bandgap semiconductors [1.12 – 1.18]. Si and GaAs are included for comparison.

### 1.2.3 SiC for microelectronics applications

SiC is the only studied wide bandgap semiconductor having silicon dioxide (SiO<sub>2</sub>) as native oxide, similarly to silicon. SiO<sub>2</sub> as a dielectric is needed for surface passivation of SiC devices, as well as for a gate material in metal-oxide-semiconductor field-effect transistors (MOSFETs) and related structures. Silicon dioxide can be formed by simple wet or dry oxidation of SiC. Since here the oxidation rate is lower as compared to Si, typical temperatures higher than 1000 °C are needed for reasonable processing times for growth of SiO<sub>2</sub>. Despite significant progress in recent years resulted in good quality bulk SiO<sub>2</sub> on SiC, insufficient quality of the SiO<sub>2</sub>/SiC interface is of major concern. Recently carbon dangling bonds have been identified as bulk and/or interface defects in 4H-SiC/SiO<sub>2</sub> systems. These defects introduce interface states and can electrically compensate n-type or p-type doped layers [1.20, 1.21]. Contrary to Si, in SiC the stable passivation of dangling bonds by hydrogen seems to be problematic. Thermal annealing at relatively low temperatures (<700 °C) in H<sub>2</sub>/N<sub>2</sub> atmosphere can passivate the dangling bond centers, but the passivation is not stable. Thermal treatments at temperatures greater than 800 °C release the hydrogen, regenerating the dangling bond defect. High interface state densities are thought to be the cause of unacceptable low inversion layer mobilities (~50-100 cm<sup>2</sup>/Vs) as compared to bulk mobility (~500-1000 cm<sup>2</sup>/Vs) in operating SiC MOSFETs. Therefore any effort to improve

the quality of the SiO<sub>2</sub>/SiC interface is a promising purpose and will be the focus for development for many years to come.

The chemical inertness and high temperature stability make SiC one of the few candidates that can operate in the exhausts of internal combustion engines or furnaces. Sensors made of SiC can detect nitric oxides, hydrocarbons, and oxygen [1.22] making them useful for regulating the combustion process and reducing harmful emission. One of the possible applications of SiC, as a material suitable for high frequency operation, is the generation of microwaves, for example in lightning and microwave ovens [1.23]. Other applications are for microwave emitters in mobile phone base stations, digital television broadcasting, or radar.

Another commercial use of SiC is as a substrate for GaN growth, since no commercially viable GaN substrate exists for homoepitaxial growth. GaN, as a direct bandgap semiconductor is used for blue and ultra violet light emitting diodes as well as for blue solid state lasers [1.24], which can help to increase the amount of information possible to store on the future CD and DVD applications.

On the other hand, due to limited knowledge on SiC, just a few products from SiC have yet been commercially realized. One of them is a high-power SiC Schottky diode [1.25] operating at 600 V and 12 A. Even though it is more expensive than a traditional diode it has been demonstrated to lower the cost of a power supply through the possibility of using a smaller and less expensive inductor. This is one example where the higher cost of using SiC in a part could be regained in a lower total cost.

### 1.3 Crystal Structure and Polytypism

In this section we will discuss SiC's crystalline structure and its polytypic nature. The influence of polytypism on the physical properties of SiC is also presented.

Silicon carbide is a binary compound containing equal amount of Si and C, where Si-C bonds are nearly covalent, with an ionic contribution of 12% (Si positively, C negatively charged). The smallest building element of any SiC lattice is a tetrahedron of a Si (C) atom surrounded by four C (Si) atoms (see Fig. 1.1) in strong sp<sup>3</sup>-bonds. Therefore the first neighbor shell configuration is identical for all atoms in any crystalline structure of SiC. The tetrahedral bond angle,  $\Theta$ , as depicted in Fig. 1.1, is 70.529° for the ideal bond configuration.

One of the most characteristic properties of SiC is polytypism – a one dimension-type polymorphism. To date more than 200 different polytypes of SiC are known to exist [1.26]. There is only one cubic polytype sometimes referred as  $\beta$ -SiC, all the others then called  $\alpha$ -SiC.

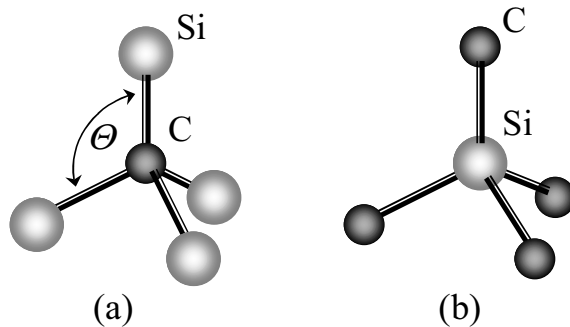


**Figure 1.1** Basic elements of SiC crystals: Tetrahedrons containing (a) one C and four Si (b) one Si and four C atoms.

The crystalline structure of any of SiC polytypes can be viewed as the stacking sequence of close-packed spheres, where each plane of spheres represents a Si-C biplane, the Si atoms lying exactly above the C atoms along the stacking axis (c-axis). When identical spheres are packed together as close as possible in a single layer, each sphere has six touching neighbors (see spheres in Fig. 1.2a). The most compact stacking of such layers results when each layer is placed in the indentations left by the previous layer. For each layer there are two possibilities, which are indicated by rectangles and triangles and denoted as B and C in Fig. 1.2a. Due to this freedom, there is in principle an infinite number of different ways of stacking the layers. Each polytype of SiC can be characterized by the stacking sequence of layers A, B and C. For instance, stacking the layers in ABC order will produce zincblende structure, while stacking sequence of AB – wurtzite.

A commonly used nomenclature is the Ramsdell notation [1.27], describing each polytype with a number, followed by a letter. The number denotes the count of double layers in one period, and the letter stands for the symmetry, which can be cubic (C), hexagonal (H), or rhombohedral (R). The 2H-polytype has wurtzite crystal structure, while 3C-SiC possesses zincblende lattice. Other polytypes are mixtures of zincblende and wurtzite structures, most popular of them are 4H, 6H, and 15R-SiC, with corresponding stacking sequences of ABCB, ABCACB, and ABCACBCABACBCB, respectively (see Table 1.2 and Fig. 1.2b).

Another way to describe the structure of polytypes is tracing the path of covalent bonds between Si and C atoms on the projected atomic positions onto a (11-20) plane as shown in Fig. 1.2b. At the turning points of the zigzag patterns in the non-cubic SiC polytypes the local environment of the Si-C pair is said to be hexagonal (h), while between the turning points the local environment is called cubic (k). As it was already mentioned the nearest neighbor (NN) atomic shell is identical for the Si or C atoms both for cubic and hexagonal sites. Contrary, the coordination of the next nearest neighbor (NNN) shells differs. Note, that for mixed-structure polytypes cubic and hexagonal lattice sites can also split up into inequivalent quasicubic ( $k_i$ ) and hexagonal ( $h_i$ ,  $i = 1, 2, \dots$ ) sites, if their third, or further neighbors are different. In 4H-SiC, however, only single h and k sites are present, while in 6H-SiC there is one hexagonal and there are two different cubic sites, marked as  $k_1$  and  $k_2$  on Fig. 1.2b. In principle a correspondence between the polytypes, and the number of their inequivalent lattice sites can be stated (see Table 1.2).

Now it is also possible to derive the “hexagonality” of a SiC polytype, which is the percentage of the hexagonal sites out of a whole crystal. Since 3C-SiC has only cubic sites, the hexagonality is obviously zero, whereas for 2H is 100%. In mixed-structure polytypes the hexagonality varies between the two extremes, see Table 1.2.

In general, different polytypes have widely ranging physical properties [1.28], therefore SiC can be thought as a whole class of materials. For instance, all of the 200 known polytypes have an indirect bandgap, but it vary in a wide range from 2.3 (3C) to 3.33 eV (2H) as the hexagonality increases from 0 to 100 %. The well-known Choyke-Hamilton-Patrick rule predicts a linear relationship between the bandgap and the degree of hexagonality up to 50 % [1.29].



i.e. the spiral growth around screw dislocations. However, the origin of polytypism has not yet come across clearly.

## **1.4 Production and doping of SiC single crystals**

Even though crystal growth is not the object of my thesis, SiC wafers used in this work are produced by different techniques and therefore some insight to their production could be useful.

### **1.4.1 Bulk growth of SiC**

The production of large-area defect-free single crystalline SiC substrates, i.e. bulk crystals, with well-controlled doping concentrations is one of the essential parts of realizing the full potential of SiC electronic applications. On such substrates it is possible to grow so-called epitaxial layers with uniform thicknesses and homogeneous doping over large areas.

For SiC the dominating bulk growth technique is the so-called seeded sublimation growth, i.e. the modified Lely technique. Here in a closed system a solid source consisting of SiC powder is used and a temperature gradient transports material from the source to the seed. The growth temperatures are very high, 2000 – 2500 °C. The size of commercially available wafers increase continually and in year 2005 wafers with a diameter of 4 inch are already on the market, however, the production of larger wafers has been also reported. In case of seeded sublimation growth the use of a solid source and the closed system makes it sensitive to depletion of the source, specifically for the Si component. To overcome this problem the high temperature chemical vapor deposition (HTCVD) technique was developed [1.32]. Here gases, typically silane ( $\text{SiH}_4$ ) and ethylene ( $\text{C}_2\text{H}_4$ ), containing Si and C are fed into the susceptor, then decompose as they are heated and form solid particles as a mixture of Si and C. As they are heated further they sublime in a similar manner as in the sublimation growth and are transported to the seed. Since here the purification of gases is easier, the benefit of HTCVD technique is the production of high-purity material for specific applications.

Note that for most common semiconductor materials, bulk crystals are pulled from a melt (see e.g. the Czochralski technique for silicon). For SiC this method shows some extraordinary difficulties due to its thermal resistance against stoichiometric melting. However, in the presence of excess Si the carbon can be dissolved from the mixture. Liquid phase epitaxy (LPE) is a method based on this process and can be considered as another alternative to seeded sublimation growth [1.33]. A major advantage with LPE seems to be the polytype stability and the low density of defects formed during growth.

### **1.4.2 Epitaxial growth of SiC**

Bulk crystals of SiC are several cm thick thus here a trade-off between the growth rate and crystal quality must be done. The quality obtained is not good enough to be used as an active layer in a device. To solve this problem, thin layers in the 1-300  $\mu\text{m}$  range are grown on top of the substrates by epitaxial growth. For this purpose, vapor phase epitaxy (VPE) is the only considered technique for SiC. This is commonly realized in a CVD reactor where the substrate is placed and source gases ( $\text{SiH}_4$ , and  $\text{C}_3\text{H}_8$  or  $\text{C}_2\text{H}_4$ ), containing Si and C are fed through [1.34]. An off-orientation of the surface normal of the substrate to the c-axis is preferred towards the  $\langle 11\text{-}20 \rangle$  direction to be able to replicate the polytype [1.35]. An angle of  $3.5^\circ$  is employed for 6H-SiC, while  $8^\circ$  off-angle is needed for 4H-SiC. The lower

requirement on growth rate allows the epitaxial growth to occur at a lower temperature of 1450–1650 °C and closer to equilibrium, leading to a higher crystalline quality [1.36] suitable for active layer fabrication in devices.

Note that in principle, a perfect crystal is impossible to manufacture. Even if it does not contain any impurities as extrinsic defects, some amount of intrinsic crystal defects is always present to maintain the thermodynamic equilibrium. Generally, a major distinction is made between point defects and extended defects. In SiC the most important extended defects are dislocations, stacking faults and the so-called micropipes. These kinds of defects are beyond the scope of this thesis and will not be discussed here. However, interested readers can find excellent comprehensive works in the field [1.30, 1.37].

Doping of SiC during the CVD growth process can be easily obtained by adding to silane and ethylene a third precursor gas, containing the atoms of the dopant species. For n-type doping of SiC, nitrogen gas ( $N_2$ ) is used, and for p-type material, trimethylaluminum ( $Al(CH_3)_3$ ) with Al as a dopant. Other dopants are boron and phosphorus, which give p- and n-type doping, respectively. A large range of doping concentrations ( $10^{14}$  to  $10^{19} cm^{-3}$ ) can be achieved for both n- and p-type. N has been shown to substitute C (i.e. to bond Si) in the crystal lattice [1.38], while Al substitutes Si (i.e. bonds C) [1.39].

#### ***1.4.3 Growth of different polytypes***

Even though there exist more than 200 different polytypes of SiC, they are not equally easy to grow. The seeded sublimation growth technique is primarily suitable for the production of 4H and 6H-SiC. The largest bandgap in a thermally stable polytype is 3.26 eV in 4H-SiC. The saturation drift velocity of carriers is higher in 4H than in 6H-SiC, making the propagation of electronic signals faster in 4H-SiC. Therefore there is a strong emphasis on studying the properties of the 4H polytype. The technology for growing large pieces of 4H for substrate production is also favorable, although the 6H polytype is easier to grow.

3C-SiC allows highest saturation drift velocity and mobility, making it most suitable especially for fast switching power devices. Some efforts have been made to produce bulk crystals of 3C-SiC, but for a long time no breakthrough has been achieved. This might be due to comparatively high temperatures needed for the sublimation, and that the 3C polytype is thermodynamically stable at lower temperatures. However, recently the production of 4-inch diameter, 200  $\mu m$  thick 3C bulk layers with good crystalline quality was reported [1.40]. The layers were deposited by CVD on Si substrates at relatively low temperature ( $t < 1450$  °C), below the melting point of Si.

2H-SiC is not thermally stable at common growth temperature [1.41] and cannot be grown in large-area stable pieces, therefore it could be only of scientific interest. Another frequently referred polytype is 15R-SiC which usually appears in common growth conditions, but is not exposed to a great attention.

This thesis deals with the 4H and 6H polytypes, which are seem to be the most promising candidates for future applications.

#### ***1.4.4 Doping of SiC by ion implantation***

When doping a semiconductor material during the crystal growth, large-area homogeneously doped wafers can be obtained with well-controlled doping concentration. However, in planar device structures a lateral separation between different parts has to be

achieved. These parts have different tasks when the device is in operation. Some improve the conduction of electrons through the device, some serve as contacts and some as a buffer or high resistance between conducting areas. Hence, these parts have different electrical properties, depending on the choice of material and doping, and therefore in such cases selective area doping is needed.

In case of conventional semiconductors, e.g. Si, selective area doping is possible through thermal diffusion in combination with masking techniques. In Si the diffusion processes for common donor (P, As) and acceptor (B, Al) impurities are well established.

A summary of diffusion data in Si and SiC can be found in Table 1.3. The melting point for Si is about 1400 °C, whereas SiC sublimes above 2800 °C. Dopant diffusion can be investigated at temperatures close to the phase transition temperature of the semiconductor (see Table 1.3). Due to the high band energy and the small inter-atomic distances in SiC, the diffusion of larger atoms is strongly prohibited. Only small atoms like hydrogen, lithium, boron and beryllium have a fast diffusion branch and have considerably fast migration in SiC [1.42]. As Table 1.3 shows the migration energy barriers in SiC are significantly higher as compared to that in Si. This gives a strong temperature dependence of the effective diffusion coefficient in SiC leading to negligible dopant diffusion at temperatures below 1400 °C, i.e. the melting point for Si. Because of high temperatures above 2000 °C are needed, thermal diffusion cannot be considered as a practical doping process for SiC. But diffusion mechanisms still have to be investigated as dopants are redistributed during the high-temperature processes of epitaxial growth (1450 – 1650°C) and post-implantation annealing (1500 – 2000°C).

In semiconductor processing ion implantation is the key technology for doping, besides crystal growth and thermal diffusion. Ion implantation means that electrically accelerated energetic ions are shot into the crystal. The ion energy is usually in the range 100 keV–1 MeV. Implantation, as a thermally non-equilibrium process has the advantage that basically all stable elements of the periodic table can be implanted. Therefore in case of SiC this is the only technique suitable for selective doping with N, Al, B or P. In addition, doping concentrations and doping profiles can be adjusted reproducibly and varied over a wide range. However, as a disadvantage, ion implantation causes damage to the crystal structure, depending on the ion mass, ion energy, the implanted fluence and the fluence rate (the number of implanted ions per unit area and unit time, ions cm<sup>-2</sup>s<sup>-1</sup>). To reduce the induced damage and to electrically activate the implanted dopant species, usually high-temperature post-irradiation annealing has to be performed. The high temperature stability of SiC is a disadvantage in this case since implantation also produces some high temperature stable defects. These will be very difficult to remove, by annealing, once they are created.

As it can be seen from the previous sections, SiC research and processing is a complex field with many open questions. Every problem mentioned above – even more or less significant – has to be solved in order to be able to fabricate continuously operating, non-deteriorate and reliable structures. To accomplish this purpose a very important obstacle to be eliminated is to understand the structure and properties of point defects and to tailor the depth distribution of dopants and ion irradiation-induced damage in the material. Now we turn to the main scope of this thesis and first give a short introduction to the nature of point defects and defect creation mechanisms taking place during electron irradiation into SiC.



Material	Dopant	Act. energy (eV)	Effective diffusion coefficient		
			Fast branch (cm <sup>2</sup> /s)	Slow branch (cm <sup>2</sup> /s)	Temperature range (°C)
SiC	N	7.6 – 9.3	-	$5 \times 10^{-12}$	1800 – 2450
	Al	4.9 – 6.1	-	$3 \times 10^{-14} - 6 \times 10^{-12}$	1800 – 2300
	B	5.1 – 5.5	$2 \times 10^{-9} - 1 \times 10^{-7}$	$2.5 \times 10^{-13} - 3 \times 10^{-11}$	1800 – 2300
	Ga		-	$2.5 \times 10^{-14} - 3 \times 10^{-12}$	1800 – 2300
	Si	$7.6 \pm 1$	$\sim 1 \times 10^{-16} - 1 \times 10^{-14}$		2000 – 2200
	C	$7.6 \pm 1$	$7.2 \times 10^{-15} - 3.9 \times 10^{-14}$		2100 – 2350
Si	P	3.4 – 4.4	$1 \times 10^{-14} - 6 \times 10^{-11}$	-	1100 – 1400
	As	3.4 – 4	$5 \times 10^{-16} - 6 \times 10^{-12}$	-	1100 – 1400
	Al	3 – 4.1	$1 \times 10^{-13} - 2 \times 10^{-10}$	-	1100 – 1400
	B	$\sim 3.5$	$3 \times 10^{-14} - 5 \times 10^{-11}$	-	1100 – 1400
	Si	3.9 – 5.1	$\sim 4 \times 10^{-18} - 5 \times 10^{-14}$		950 – 1200

**Table 1.3** Activation energy [1.18, 1.45] and effective diffusion coefficient [1.42] for various impurities in SiC and Si. The self-diffusion coefficients for silicon [1.43] and carbon [1.43, 1.44] in SiC and for silicon in Si [1.45] are also included.

## Chapter 2

### Point defects in SiC

#### 2.1 Classification of point defects

Let us concentrate on point defects in SiC. In principle, the binary compound nature and the existence of inequivalent lattice sites in different polytypes give rise to a large variety of possible defects. In SiC point defects can be classified as follows:

- a) a vacancy, when an atom is removed from its original lattice site. It should be either silicon vacancy ( $V_{Si}$ ) or carbon vacancy ( $V_C$ ).
- b) an interstitial, when an atom occupies a site different from its regular. The interstitial atom can be the same species as the host lattice, and then it is called as self-interstitial, or a foreign atom, then called as interstitial impurity. A silicon (carbon) interstitial can be signed as  $Si_i$  ( $C_i$ ), respectively.
- c) a Frenkel pair is formed when a vacancy is located close to a self-interstitial.
- d) an antisite, when an atom of one sublattice is placed in the other. It could be silicon antisite ( $Si_C$ ) or carbon antisite ( $C_{Si}$ ).
- e) an impurity, a foreign atom, occupying a regular lattice site. For instance, an aluminum atom in Si site ( $Al_{Si}$ , as an acceptor), or a nitrogen atom in C site ( $N_C$ , as a donor).

In addition, combinations of these simple point defects are often possible, e.g.  $V_{Si}-V_C$  divacancies,  $C_{Si}-V_C$  vacancy–antisite pairs,  $N-V_{Si}$  vacancy–impurity pairs, or even more complex defects can be formed. All these defects can occupy both cubic and hexagonal sites in mixed-structure SiC polytypes. Thus, for example,  $(C_{Si}-V_C)(h)$ , and  $(C_{Si}-V_C)(k)$  can exist in 4H-SiC, or  $V_C(h)$ ,  $V_C(k_1)$ , and  $V_C(k_2)$  in 6H-SiC, respectively.

Defects realized by the presence of foreign atoms are called extrinsic defects. These are for example donors or acceptors, or foreign interstitials. On the other hand, defects arising through the rearrangement of the host atoms of the original lattice are called intrinsic defects. These could be e.g. self-interstitials, vacancies or antisites. Of course, in complex defects both intrinsic and extrinsic defects could be mixed together (like in  $N-V_{Si}$ ).

The existence of the difference between inequivalent lattice sites in SiC can give rise to, for example, different ionization energies with the same atom species of substitutional donor or acceptor atoms [2.1]. Properties of intrinsic point defects are generally also site dependent. Defects, occupying both k and h sites have different energy levels in the bandgap, which usually can be detected, e.g. by optical or electron paramagnetic resonance (EPR) techniques. Fig. 2.1 shows schematic pictures of different point defect configurations in silicon carbide [2.2].

It is worth to note that generation of defects, as lattice imperfections is usually accompanied by the relaxation of the surrounding atoms, in order to attain the minimum-energy configuration in the obtained new circumstances. Either inward or outward relaxation can occur around the defect center, resulting in a volume change of the tetrahedron defined by

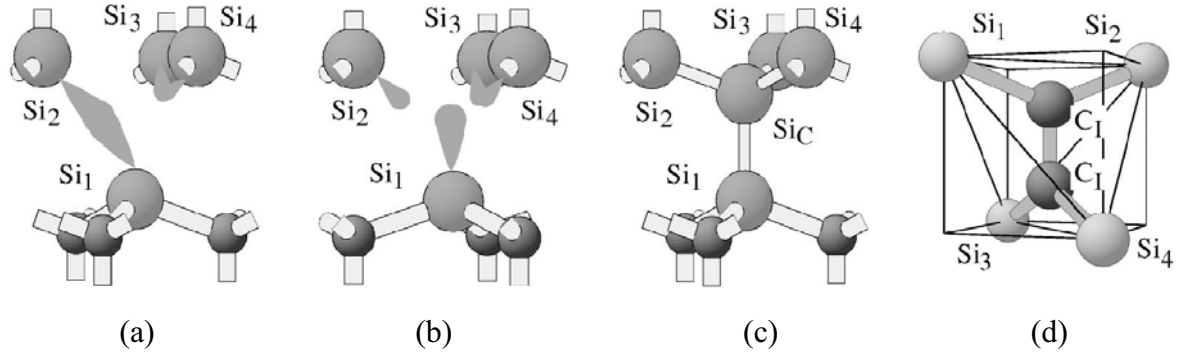


**Figure 2.1** Calculated geometry of point defects in SiC taken from Ref. [2.2]: the carbon vacancy at (a) cubic and (b) hexagonal lattice site, (c) the silicon antisite and (d) the carbon split interstitial in cubic SiC oriented along the  $\langle 100 \rangle$  axis,  $C_{sp\langle 100 \rangle}$ .

the nearest-neighbor (NN) atoms. The original point group symmetry can also be changed around a defect during the relaxation process, if in an electronically degenerate initial (undistorted) state the degeneracy is removed and the total energy of the system is lowered. In many cases this so-called Jahn-Teller distortion [2.3] can lower the original symmetry.

So far a few isolated point defects have been unambiguously identified in SiC. Usually a combination of several experimental techniques as well as theoretical calculations is necessary to get to final conclusions. The fundamental research on defects in SiC is thus one of nowadays' most actual research fields.

## 2.2 Shallow and deep levels

In addition to the classifications above, it is common to group defects according to the localized bandgap states they give rise to. States that have energies close to either the valence ( $E_V$ ) or conduction band edges ( $E_C$ ) are usually called shallow levels, whereas states with energies that are far from both the bands are called deep levels.

The classical examples of shallow defects are impurities with (shallow) donor or (shallow) acceptor states, due to the loosely bound electron or hole around them. They are usually well described in terms of the Effective Mass Theory (EMT) [2.4], which predicts a hydrogen-like series of states in the bandgap close to  $E_C$  or  $E_V$ . The main feature of EMT is the assumption of a screened Coulomb potential for the carrier due to the charged core of the defect. The effect of the crystal lattice is accounted for by the macroscopic dielectric constant  $\epsilon$  describing the screening and the effective mass  $m^*$  for the dynamic properties of the carrier. A characteristic feature of shallow defect states is that the wavefunction of the loosely bound carrier is quite delocalized and extends over several hundred neighboring atoms.

For deep level defects, EMT cannot be adopted, as the defect wavefunction decreases exponentially away from the defect and has smaller extension as compared to shallow levels. The defect potential can be viewed as a rectangular well, compared to Coulomb attractive well shown in Fig. 2.2. Such a strong localization can be treated using tight-binding theory, and the entire band structure must be involved in a theoretical description of these levels, since they interact both with the valence and conduction bands. However, no equally applicable general theory, like EMT has been developed for deep levels. The major reason for

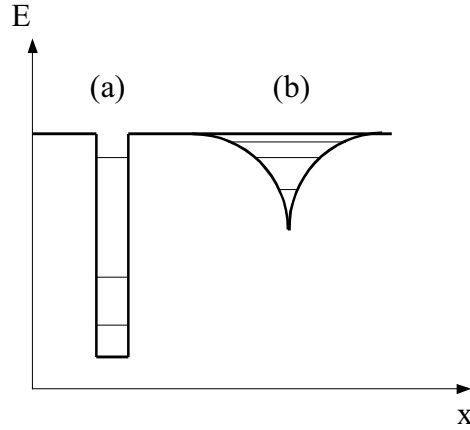


**Figure 2.2** *Electron eigenstates in a (a) rectangular and (b) Coulomb-attractive well.*

this is the huge variety of possible defect configurations, from vacancies over certain substitutional impurities (like vanadium) to complexes. Here the calculations are more complicated than that for the EMT model, and it can be understandable considering the fact that the quantum mechanical problem of the hydrogen atom with one proton and one electron is the most complicated case that can be analytically solved.

We shall not discuss here more on the theory of deep centers instead some of their important properties will be briefly summarized.

### 2.3 Defect charge states and formation energies

Let us consider a deep center, with the energy level  $E_T$  located in the bandgap and with a uniform concentration of  $N_T$  defects  $\text{cm}^{-3}$  over the semiconductor material (see Fig. 2.3). There are four processes describing the dynamic behavior of the deep state, namely the individual capture and emission processes of both electrons and holes, with corresponding emission and capture coefficients (probability per unit time) of  $e_n$ ,  $e_p$ ,  $c_n$ , and  $c_p$  (see Fig. 2.3).

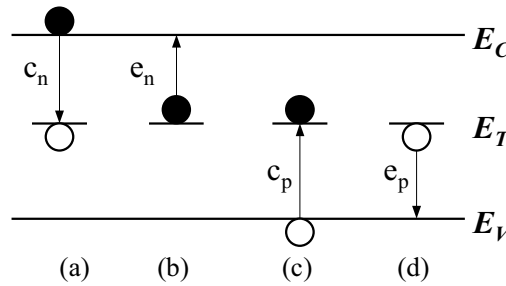


**Figure 2.3** *Emission and capture processes to and from a deep level located in the bandgap of a semiconductor.*

Let us mark the capture of an electron from  $E_C$  to  $E_T$  as event (a) and the emission of an electron from  $E_T$  to  $E_C$  as event (b). Similarly, the capture of a hole from  $E_V$  to  $E_T$  is event (c) and the emission of a hole from  $E_T$  to  $E_V$  is event (d). Now four different processes can be considered (see Fig. 2.3):

1. recombination: event (a) is followed by event (c)
2. generation: event (b) is followed by event (d)
3. trapping electrons: event (a) is followed by event (b)
4. trapping holes: event (c) is followed by event (d)

The occupancy of the state  $E_T$  is determined by competing emission and capture processes. Electrons can be emitted and holes can be captured at the  $n_T$  states occupied by electrons and holes can be emitted and electrons can be captured at the  $(N_T - n_T)$  states occupied by holes. If the trap has a degeneracy factor  $g_0$  when empty and  $g_1$  when occupied by one electron, it can be shown that in thermal equilibrium the electron and hole emission is written as:

$$\frac{e_n}{c_n} = \frac{g_0}{g_1} \exp\left(\frac{E_T - E_F}{kT}\right) \quad \text{and} \quad \frac{e_p}{c_p} = \frac{g_1}{g_0} \exp\left(\frac{E_F - E_T}{kT}\right) \quad (2.1)$$

where  $E_F$  is the Fermi level in the material. Roughly speaking, if  $E_F > E_T$ , then  $c_n > e_n$  and  $e_p > c_p$  so that the state is occupied by electrons, whereas when  $E_F < E_T$  the state is empty.

Many defects can introduce more than one deep level in the bandgap. These are usually denoted  $+/++$ ,  $0/+$ ,  $-/0$ ,  $--/-$ , etc., where the first symbol represents the charge state of the defect when an electron is bound to it, and the second one is the charge state of the empty level. The difficulties arise from inserting levels representing many-particle states into a picture showing single particle energies (the band structure). Even though the resulting figures are formally incorrect, they are still satisfactory for the illustration of processes like photoionization. In order to gain information about the equilibrium concentrations of different charge states of a specific defect, the formation energies for all possible charge states have to be calculated. Considering a charged defect, the formation energy can be expressed as [2.5]:

$$E_f = E_{tot}(q) + q(E_V + \mu_e) - n_{Si}\mu_{Si} - n_C\mu_C \quad (2.2)$$

Here  $\mu_e$  is the electron chemical potential, (i.e. the Fermi level), measured relative to the valence band maximum  $E_V$ ,  $E_{tot}$  is the calculated total energy of the crystal, containing  $n_C$  carbon and  $n_{Si}$  silicon atoms and the defect. If the defect binds an extra charge of  $q$ , this has to be transferred from a reservoir to the level of the electron chemical potential ( $\mu_e$ ). The last two terms in Eq. 2.2 describe the energy which  $n_{Si}$  silicon and  $n_C$  carbon atoms have in the ideal SiC crystal. The formation energies arising from Equation 2.2 can be plotted as functions of  $\mu_e$  for all charge states. This is shown in Fig. 2.4, calculated for carbon vacancy defects in 4H-SiC [2.5]. When  $\mu_e$  is low, positive charge states are favored, meanwhile at high values of  $\mu_e$  the vacancy is able to bind extra electrons and negative charge states are more favorable. The ionization levels are defined as those values of  $\mu_e$  where the formation energy lines of two stable charge states intersect. The realization of a specific charge state for a given Fermi level  $\mu_e$  requires that the formation energy of the defect in the corresponding charge state is lower than for the other possible charge states. Therefore a change in the Fermi level position can lead to the change of the dominant charge state of the defect.

The above picture can be extended for different kinds of defect centers in the material. The concentration of any defect in thermal equilibrium can be expressed as:

$$C = zN_S \exp(-E_f / k_B T) \quad (2.3)$$

where  $z$  is the number of different possible configurations for the defect per the sublattice site, and  $N_S$  is the number of sublattice sites per unit volume. According to Equation 2.3, in

thermal equilibrium, defects of low formation energies are present in high concentrations, whereas defects of high formation energies in low concentrations, respectively.

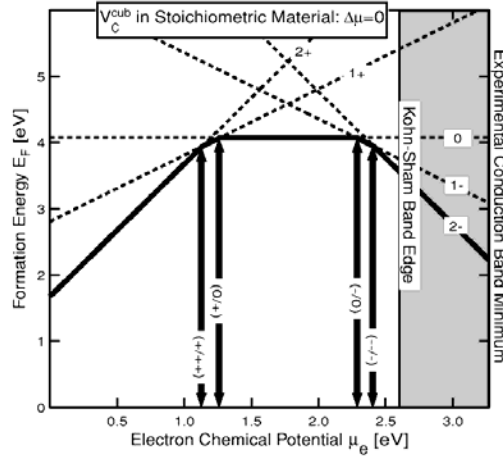


**Figure 2.4** Formation energies for different charge states (dashed lines) of carbon vacancies at the cubic lattice site of stoichiometric SiC taken from Ref [2.5]. The thick solid line corresponds to the lowest formation energy as a function of the electron chemical potential.

The important property of deep levels is the ability to influence carrier lifetime significantly even at low concentrations. According to Shockley-Reed-Hall [2.6,2.7] statistics, the minority carrier lifetime (for a single deep trap) is given by:

$$\tau = \frac{c_p(p_0 + p_1) + (n_0 + n_1)}{c_n c_p N_T(n_0 + p_0)} \quad (2.4)$$

Here  $n_0$  and  $p_0$  are the electron and hole densities at thermal equilibrium, and  $n_1$  and  $p_1$  are the electron and hole densities for the case that the Fermi level  $E_F$  is at the energy position  $E_T$  of the deep level.

It can be shown [2.8] that  $\tau$  depends sensitively on the position  $E_T$  of the deep level in the bandgap. If we consider two defect centers with energy level difference of 0.4 eV, the lifetime at room temperature will be determined by the deeper level even if its concentration is 6 orders of magnitude lower than the concentration of the shallower level. This is mainly due to the exponentially decreasing probability of thermal reemission from the defect for deeper levels.

## 2.4 The role of deep levels

Presence of deep-level defects as efficient carrier traps can seriously affect the performance of some semiconductor devices, which depend on long minority carrier lifetimes. However, these centers can be beneficial as well, particularly in high-speed electronic devices, in which fast switching requires the efficient removal of minority carriers.

Another field to use deep-level defects is the production of semi-insulating SiC (SI-SiC) substrates, e.g. for metal-semiconductor-field-effect transistor (MESFET) structures. In order for a semiconductor to be semi-insulating, the Fermi level has to be close to the middle of the bandgap. In the first generation of SI-SiC substrates, deep amphoteric levels of vanadium are used for compensating shallow impurities and extremely high resistivity can be obtained. However, as found recently, SiC MESFETs using heavily vanadium-doped SI-SiC substrates have serious problem with carrier trapping to deep level centers, leading to the instability of devices. This creates the interest of replacing vanadium by intrinsic defects.

Recently, both types of high-purity SI wafers grown by HTCVD [2.9] and PVT [2.10] are shown to have good SI properties and have become commercially available. However, the question, what kind of intrinsic defects cause high resistivity in these SI-SiC substrates is still debated and is in the scope of state of the art studies. In Chapter 4 we will briefly return to this question.

## 2.5 Electron irradiation

One way to introduce defects into the material is to irradiate it by energetic particles. In general, the creation of defects is not always a detrimental effect. Besides the beneficial applications mentioned above, irradiation-induced defect studies are also very important for the identification of as-grown defects, separating spectroscopic or magnetic resonance signals arising from contributions of intrinsic defects and residual impurities. In this section we discuss some details of physics behind electron irradiation. As my results related to this part deal with defects in SiC irradiated by 2.5 MeV electrons, henceforward this energy value is considered in the mathematical expressions.

An incident energetic particle that enters a solid interacts with electrons and nuclei. The energy loss of the particle depends on the nature of the particle and its energy. Elastic collisions with the nuclei lead to atomic displacements, whereas the interaction with electrons of the solid determines the penetration depth of the particle. The former process is often called as nuclear stopping, and the latter as electronic stopping. Schematic picture of a simple binary elastic collision is depicted in Fig. 2.5.

Let  $E$  be the kinetic energy of an incident particle with mass  $m$ . The amount of kinetic energy  $T$  transmitted to the atom of mass  $M$  depends strongly on the angular deflection of the incident particle. For electrons with energy of 2.5 MeV and corresponding velocity of  $\sim 0.98 c$  ( $c$  is the velocity of light), relativistic corrections are necessary in the description of the motion. Conservation of kinetic energy and momentum gives the following result for transferred energy in the laboratory frame of reference [2.11]:

$$T = 2 \frac{m}{M} E \left( 2 + \frac{E}{mc^2} \right) \cos^2 \varphi \quad (2.5)$$

For  $E = 2.5$  MeV in a head-on collision ( $\theta = 180^\circ$ ,  $\varphi = 0^\circ$ , and  $P = 0$ )  $T$  is 80 eV and 190 eV for Si and C atoms, respectively. The atom of the crystal lattice lies in a potential well of depth  $E_d$ , called the threshold energy of atomic displacement. In a simplest approximation, the

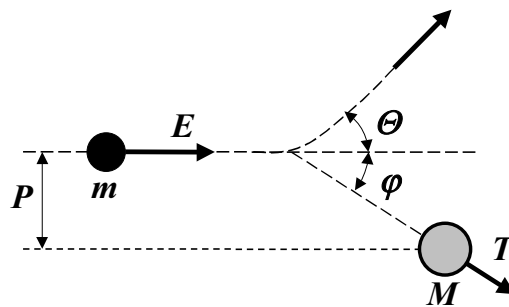


**Figure 2.5** Schematic model of the collision between an incident particle of mass  $m$  and energy  $E$  with an atom with mass  $M$

probability to displace an atom is 1 for  $T > E_d$  and 0 for  $T < E_d$ . A displacement is a three-step process, first the four bonds must be broken – requiring four times the bond energy, secondly the atom must be removed from the lattice site and placed as an interstitial and finally the lattice will relax around the vacancy and the interstitial. In SiC, silicon and carbon will have four equal bonds, and thus the energy required to break them will be equal for both. However, molecular dynamics calculations show that stable displacements are created preferentially in the C sublattice. Hensel and Urbassek have shown [2.12] that this is not a mass effect (the mass of the Si atom is more than twice that of the C atom), but is related to the different interatomic potentials, i.e. the small dislocation threshold and atomic radius of C in comparison to Si (covalent atomic radii of Si and C are 1.17 Å and 0.77 Å, respectively [2.13]).

Recent deep level transient spectroscopy [2.14] and photoluminescence [2.15] experiments as well as earlier works based on measurement of the frequency-response of light emitting SiC diodes [2.16] have revealed a  $E_d$  value of ~20 eV for the C sublattice of SiC. Concerning the Si sublattice, electron paramagnetic resonance [2.17] and photoluminescence [2.15] experiments were performed, however, the extracted  $E_d$  values are scattered in a wider range of 20-40 eV. All of the experiments were performed on sub-threshold electron-irradiated SiC samples when the initial energy of electrons is adjusted in small steps up to the threshold for the creation of displacement-related defects. Usually carbon-related defects appear first about 100 keV electron energy whereas silicon-related defects emerge above 200 keV. From the threshold electron energy  $E_{th}$  the value of  $T_{th} = E_d$  can be derived using Equation 2.5.

Due to the tetrahedral bonding in SiC, the energy required to remove an atom from its lattice site will vary depending on irradiation direction. Drawing the values of  $E_d$  for recoils along different crystallographic directions gives the so-called displacement energy surface. Molecular dynamics calculations predict the displacement energy surface of SiC to be largely anisotropic [2.18]. The largest difference has been shown between the  $\langle 0001 \rangle$  and  $\langle 000\bar{1} \rangle$  directions.  $E_d$  is much higher for Si along  $\langle 0001 \rangle$  than along  $\langle 000\bar{1} \rangle$  and vice versa for C. Because of this high anisotropy, a difference between defect generation rates is expected for  $\langle 0001 \rangle$  and  $\langle 000\bar{1} \rangle$  directions at electron energies close to the displacement threshold. This has been confirmed for carbon-related defects in electron irradiation experiments in the energy range of 80-300 keV using DLTS technique for defect monitoring [2.14]. As the electron energy increases above 300 keV, the sub-threshold anisotropy become less and less significant and defect generation rates for different irradiation directions converges to the same value. It can be attributed to the larger energy transferred to the target atoms and that the electrons even of large scattering angles ( $\Theta$ ) and therefore stronger deflections from the  $\langle 0001 \rangle$  axis will have enough energy to displace lattice atoms. This way the system “forgets” the initial accurate orientation of the momentum to be transferred. Further increasing the electron energy will result in the starting of displacement cascades. A displacement cascade can be started by a primary-knock-on Si or C atom (PKA), provided that the energy transmitted to the PKA exceeds  $E_d$  by at least two times. In case of 2.5 MeV electrons, the transmitted energy is still close to  $E_d$ , and displacement cascades do not dominate defect formation. Only point defects are created due to spatially separated PKAs.

Assuming a screened Coulomb interaction potential for an elastic collision between 2.5 MeV electrons and Si or C nuclei, the total cross-section,  $\sigma_{tot}$  for an electron to scatter is



the order of  $\sim 0.1 \text{ nm}^2$ . Considering random scattering in the target, it is possible to calculate the average mean free path  $\lambda$  between elastic collisions:

$$\lambda = \frac{1}{N_{\text{SiC}} \sigma_{\text{tot}}} \quad (2.6)$$

where  $N_{\text{SiC}} = 9.64 \times 10^{22} \text{ cm}^{-3}$  is the atomic density of SiC. The above expression results in  $\lambda \approx 10 \text{ }\mu\text{m}$ . Therefore the damaged zone left behind by one electron is rather dilute.

Another process slowing down the incoming electrons is the inelastic electronic stopping. This is the (average) rate of energy loss per unit path length, due to Coulomb collisions with the atomic electrons that result in the ionization and excitation of atoms. The electronic stopping term  $S_e$  for electrons can be quickly estimated e.g. by the program code ESTAR [2.19] resulted in  $0.8 \text{ eV nm}^{-1}$  for  $2.5 \text{ MeV}$  electrons. The corresponding penetration depth is the order of  $1 \text{ mm}$ , allowing particles to get across the whole sample.

Note for electron irradiation and high-energy proton implantation in the low-fluence region the total amount as well as the concentration of defects in SiC increase linearly with fluence [2.14, 2.20]. In this case simple accumulation of point defects occurs. At higher electron fluences Matsunaga has found the saturation of defect induced lattice disorder [2.21]. This suggests that the recombination of point defects should also play an important role.

In summary, electron irradiation in MeV energy range will introduce point defects in low concentration over a  $\sim \text{mm}$  depth range. The total number of defects will be quite high due to the large volume of damaged material. The absence of extended cascade processes and the strong spatial separation between the introduced point defects gives low probability of interactions between primary defects to form complexes and/or larger clusters during the irradiation. Low defect concentrations in combination with homogeneous defect distributions prevent the crystal structure from the accumulation of strain accompanied by strong lattice relaxation. These circumstances are ideal for a number of defect characterization techniques. One of these techniques, electron paramagnetic resonance (EPR), is very sensitive to the local surrounding environment of point defects as well as the orientation of the crystal. Since EPR is a bulk method it requires a high total number of the kind of defects investigated (PL or DLTS techniques are more sensitive by orders of magnitude). Therefore to obtain strong and sharp EPR lines related to point defects, high-fluence electron-irradiated samples are good candidates. Nevertheless, EPR yields integrated information from the entire sample, therefore the depth distribution of defects cannot be investigated (the total amount can be estimated using well-calibrated standards). Now, let us discuss the details of the EPR technique.

## Chapter 3

### Principles of EPR and related techniques

#### 3.1 A Magnetic moment in magnetic field

The existence of the quantity that is the key factor in electron paramagnetic resonance (EPR), the electron spin,  $S$ , has been observed first in the Stern-Gerlach experiment in 1922 [3.1] when a beam of silver atoms was split into two components by an inhomogeneous magnetic field. Later, the understanding on magnetism has been greatly improved both experimentally and theoretically, mainly due to Gorter [3.2] and van Vleck [3.3] in the 1930s and 1940s. Based on these establishments, the first successful EPR experiment has been reported by Zavoisky in 1945 [3.4].

The quantum mechanical spin operator,  $\hat{S}$ , as an internal degree of freedom for an electron, has been introduced by Dirac who has shown that  $\hat{S}$  possesses the properties of an angular momentum. The magnitude of this angular momentum is given by the square root of the eigenvalue of  $\hat{S}^2$  that is  $\sqrt{S(S+1)}$ . If the angular momentum is projected onto a specific direction, the set of its eigenvalues is denoted as  $\{M_S\}$  running between  $+S$  and  $-S$  in integral steps. For an electron  $S=1/2$  and consequently,  $M_S = \pm 1/2$ .

The magnetic moment corresponding to the angular momentum of a free electron can be written as [3.5]:

$$\mu_e = -g_e \mu_B S \quad (3.1)$$

where  $\mu_B$  is the Bohr magneton and  $g$  is the free electron g-factor with a value of 2.0023. The negative sign in Equation 3.1 indicates that for an electron the magnetic moment is antiparallel to the spin.

Similarly to electrons, atomic nuclei also have spins if the numbers of protons and of neutrons are not both even. Here the magnitude of the angular momentum operator,  $\hat{I}$ , is  $\sqrt{I(I+1)}$ ; the set of projections onto a specified direction is  $\{M_I\}$ , taking integral values from  $+I$  to  $-I$ . The nuclear magnetic moment operator is [3.5]:

$$\mu_N = g_N \mu_N I \quad (3.2)$$

where  $e_p$  and  $m_p$  are the proton charge and mass, and  $g_N$  is the nuclear g-factor, respectively. Note,  $g_N$  is characteristic of a particular isotope, and gives a value of  $-1.1106$  for  $^{29}\text{Si}$  and  $1.4044$  for  $^{13}\text{C}$ , respectively (more about isotopes in SiC will be discussed in Section 3.3.3).

Consider a magnetic moment  $\vec{\mu}$  in a magnetic field  $\vec{B}$  with an angle  $\vartheta$  between the directions of the two vectors. Classically, the energy of the system can be written as [3.5]:

$$E = -\vec{\mu} \cdot \vec{B} = -\mu B \cos \vartheta \quad (3.3)$$

where  $\mu$  and  $B$  are the magnitudes of the corresponding vectors. In quantum mechanics  $\vec{\mu}$  is replaced by its appropriate operator and the energy  $E$  is replaced by the Hamiltonian  $\hat{H}$ . For a free electron, if  $\vec{B}$  is parallel to the z-axis (and  $S$  is projected onto the z-axis),  $\hat{H}$  can be written as [3.5]:

$$\hat{H} = g_e \mu_B \hat{S}_z B \quad (3.4)$$

The substitution of  $\{M_S\}$ , as the eigenvalues of  $\hat{S}_z$  into Equation 3.4 will give the eigenvalues of  $\hat{H}$ , i.e. the energy states  $E$  of the system [3.5]:

$$E = g_e \mu_B B M_S \quad (3.5)$$

Since  $M_S = \pm 1/2$ , there are two energy states which degenerate in zero field and their separation increases linearly with the magnetic field. The Hamiltonian in Equation 3.4 describes the so-called linear Zeeman interaction between the external magnetic field and the electron spin.

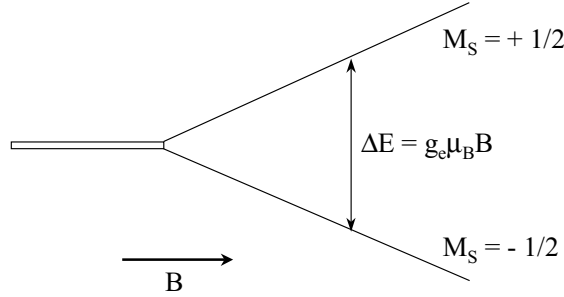


**Figure 3.1** Energy levels for an electron spin  $S = 1/2$  in an applied magnetic field  $B$ .

Fig. 3.1 shows the energy levels for an electron spin in function of the applied magnetic field  $B$ . Using the Bohr frequency condition, the quantum of radiation can be derived for the separation  $\Delta E$  of the two levels [3.5]:

$$\Delta E = h\nu = g_e \mu_B B \quad (3.6)$$

This is the basic resonance condition for a free electron. Scaling the resonant frequency by the magnetic field Equation 3.6 gives almost exactly  $28 \text{ GHz (T)}^{-1}$ . For a field 0.34 T used in a typical EPR experiment, the required frequency is about 9.5 GHz. The corresponding wavelength is  $\sim 32 \text{ mm}$  which is in the microwave region (X-band) of the electromagnetic spectrum.

A similar treatment for protons at a magnetic field 0.34 T gives a resonant frequency of 14.5 MHz, being almost 3 orders of magnitude lower than the resonant frequency for electrons. Consequently, at a fixed magnetic field the separation of the energy levels for protons can be considered as a small perturbation to the separation of the energy levels for electrons.

In thermal equilibrium the ratio of the populations of the upper and lower spin states  $N_u$  and  $N_l$  can be described by Boltzmann statistics [3.5]:

$$\frac{N_u}{N_l} = \exp(-\Delta E / kT) \quad (3.7)$$

From Equation 3.7 the fractional excess population of the lower level is [3.5]:

$$\frac{N_l - N_u}{N_l + N_u} = \frac{1 - \exp(-\Delta E / kT)}{1 + \exp(-\Delta E / kT)} \quad (3.8)$$

Equation 3.8 for a field of 0.34 T at 300 K gives a value of  $7.6 \times 10^{-4}$  for electrons, whereas  $1.2 \times 10^{-6}$  for protons. It means that in X-band EPR experiments we can usually take any nuclear spin state to be equally populated.

### 3.2 The principle of EPR

Let us imagine a classical magnetic moment  $\vec{\mu}$  with a corresponding angular momentum  $\vec{S}$  placed in a magnetic field  $\vec{B}_0$ . Then  $\vec{\mu}$  will obey Newton's third law for rotational motion [3.5]:

$$\frac{d\vec{\mu}}{dt} = g_e \mu_B (\vec{B}_0 \times \vec{\mu}) \quad (3.9)$$

If  $\vec{B}_0$  is oriented along the z-axis and its magnitude is  $B_0$ , the solution of Equation 3.9 for the Cartesian coordinates of  $\vec{\mu}$  is [3.5]:

$$\mu_x = \cos \omega_0 t, \quad \mu_y = \sin \omega_0 t, \quad \mu_z = \text{const} \quad (3.10)$$

$$\text{and} \quad \omega_0 = g_e \mu_B B_0 \quad (3.11)$$

Equations 3.10 and 3.11 describe the precession of  $\vec{\mu}$  about the z-axis at frequency  $\omega_0$ . This motion is called Larmor precession, and  $\omega_0$  is the Larmor frequency.

Consider now an additional small magnetic field  $\vec{B}_1$  ( $|\vec{B}_1| \ll |\vec{B}_0|$ ) perpendicular to the z-axis and being the magnetic component of an electromagnetic field in the microwave spectral region. If  $\vec{B}_1$  is rotating in the xy-plane around the static field  $\vec{B}_0$  with frequency  $\omega$  that is different from  $\omega_0$ , in average the magnetic moment  $\vec{\mu}$  will not seriously be affected by  $\vec{B}_1$  because of continuously changing phase shift between them. However, if  $\omega = \omega_0$ , then  $\vec{\mu}$  and  $\vec{B}_1$  are in phase, therefore  $\vec{\mu}$  experiences a constant field  $\vec{B}_1$ . The response of  $\vec{\mu}$  is a precession about  $\vec{B}_1$  with frequency  $\omega_1 = g_e \mu_B B_1$ . Since  $B_1 \ll B_0$ ,  $\omega_1$  will be much less than  $\omega_0$ . The effect of the two precessions is that the magnetic moment, during numerous Larmor precessions spiral down until its projection has the same magnitude in the -z direction, that it had originally in the +z direction. Thus  $\vec{B}_1$  changes the value of the projection of  $\vec{\mu}$  in the direction of  $\vec{B}_0$ .

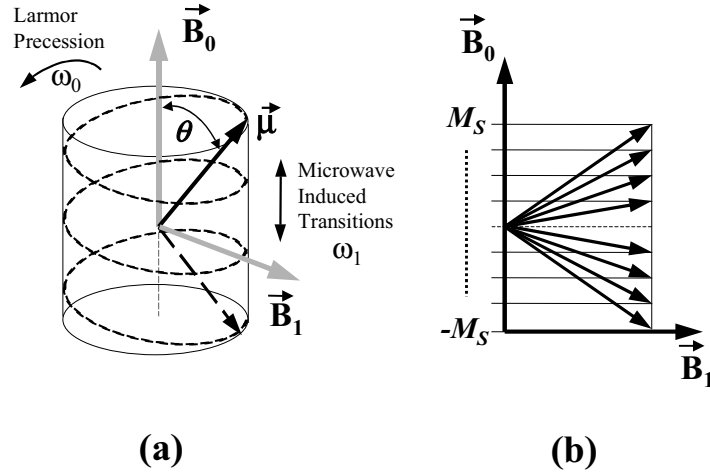


**Figure 3.2** (a) Spiral movement of a classical magnetic moment as the combination of two precessions around both the magnetic fields  $B_0$  and  $B_1$ ; (b) the quantized projections  $\{M_S\}$  of the quantum mechanical angular momentum operator  $\hat{S}$  onto the magnetic field  $\vec{B}_0$ .

In a real experiment, the exchange of energy between radiation and matter occurs discretely according to quantum mechanics. It means that while the angle  $\Theta$  between  $\vec{\mu}$  and  $\vec{B}_1$  in Fig. 3.2a can take any value in classical physics, it can take only certain discrete values in quantum mechanics. Every discrete value of the projection of  $\vec{\mu}$  corresponds to an eigenstate  $|M_S\rangle$  and an eigenvalue of  $M_S$  of the angular momentum operator  $\hat{S}$  (see Fig. 3.2b). The effect of the oscillating  $\vec{B}_1$  can be considered within first-order time-dependent perturbation theory. The result is that  $\vec{B}_1$  causes transitions from a state  $|M_S\rangle$  to another state  $|M'_S\rangle$  of the system. It can be shown [3.5] that the probability  $W_{M,M\pm 1}(t)$  of finding an initial state  $|M_S\rangle$  in the state  $|M_S \pm 1\rangle$  after a short time period of  $t$  is:

$$W_{M,M\pm 1}(t) = \frac{\mu_B^2 g^2}{4} B_1^2 [S(S+1) \pm M_S(M_S \pm 1)] \frac{\sin^2\left(\frac{1}{2}\left(\omega - \frac{\mu_B g_e}{\hbar} B_0\right)t\right)}{\left[\frac{1}{2}\left(\omega - \frac{\mu_B g_e}{\hbar} B_0\right)\right]^2} \quad (3.12)$$

From Equation 3.12 three important things can be concluded. Firstly, the maximum transition probability occurs, when the frequency of the time-dependent magnetic field is equal to the Larmor frequency and Bohr's frequency condition is satisfied. Secondly, the transition probability is proportional to  $B_1^2$  i.e. the power of the oscillating microwave component. Thirdly, the selection rule for transitions is  $\Delta M_S = \pm 1$ . If the final state is higher in energy than the initial state, a microwave photon will be absorbed, and if the final state is lower in energy a photon will be emitted. In thermal equilibrium at low temperatures, according to Boltzmann statistics, the low energy states are more densely populated, and there will be a net absorption of microwaves. However, sometimes a population inversion can be produced, leading to a net emission of microwaves. An example for such case will be shown in Section 4.3.

Equation 3.12 can also be used to calculate the probability of microwave-induced transitions between nuclear Zeeman levels. Since the probability is proportional to the square of the magnetic moment, that is about 6 orders of magnitude lower for protons than for electrons, the contribution of the nuclear Zeeman effect can be neglected, and the selection rule for transitions between nuclear spin states can be considered as  $\Delta M_I = 0$ .

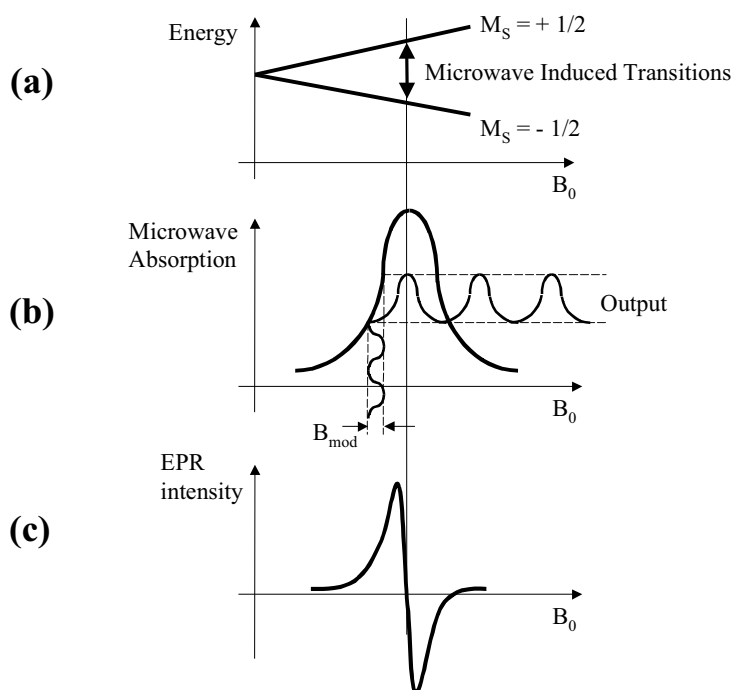


**Figure 3.3** Principle of an EPR experiment.

(a) At resonance a microwave-induced transition occurs.  
 (b) This is detected in field modulation mode, by adding an AC component  $B_{mod}$  to the scanning magnetic field  $B_0$ .  
 (c) A derivative-like EPR signal is detected.

Now we can draw the principle of EPR: the technique is based on the phenomenon that paramagnetic levels are split in static magnetic field and microwave transitions between these levels can be induced. The sample is placed in a microwave cavity, and the microwave frequency is kept fix while the static magnetic field is scanned: one varies the separation between the energy levels to match it to the quantum of radiation. The resonance can be detected as absorption of microwave power (absorption mode) or as a change in the resonance frequency of the cavity (dispersion mode). In the former case, practically, the absorption is not measured directly, but in field modulation mode, where an additional AC magnetic field  $B_{mod}$  is added to the sweeping magnetic field  $B_0$ . The signal is recorded using lock-in technique and is strongest at magnetic field  $B_0$  where the variation over  $B_{mod}$  is largest, i.e. where the slope of absorption has its maximum. Accordingly, the EPR output signal has a derivative-like line shape. Fig. 3.3 shows the schematic of a microwave induced magnetic resonance transition in absorption mode, as applied in the EPR experiments throughout this thesis.

### 3.3 Spin relaxation

The consideration of the problem of matter in thermal equilibrium with radiation lead to the conclusion that three processes occur: absorption, stimulated emission and spontaneous emission. However, it can be shown that spontaneous emission is completely negligible at microwave frequencies and so it may be disregarded in magnetic resonance [3.5]. The double arrow-head in Fig. 3.3a shows the role of both absorption and stimulated emission in

transitions between the Zeeman levels. Time dependent perturbation theory predicts equal transition probability for both processes. Therefore the effect of radiation in an EPR experiment will be to equalize the spin populations. This process leads to complete saturation, when there is no net microwave absorption to be detected. On the other hand, in continuous wave EPR the aim is to detect the continuous absorption of microwaves. In practice this really occurs due to the interaction between spins and the surrounding lattice. The lattice can be considered as a thermal reservoir that can absorb energy from the spin system. Through this interaction the difference in populations approaches its thermal equilibrium value with a so-called characteristic spin-lattice relaxation time,  $T_1$ . In practice  $T_1$  is short compared to the measurement time in continuous-wave EPR experiments, e.g. for different paramagnetic vacancy centers in SiC  $T_1$  has been found to be 4.8  $\mu\text{sec}$  and 13  $\mu\text{sec}$  [3.6].

There is another relaxation process that conserves the total energy of the spin system, but leads to the energy broadening of the resonance absorption of microwaves. In an ensemble of spins, each will at any instant, experience a local magnetic field due to other spins. This local field is different for each member of the ensemble, so there will be a spread in Larmor frequencies, which will be reflected in the linewidth of the absorption. This process is called spin-spin relaxation, and is characterized by its characteristic relaxation time,  $T_2$ . Assume that the static magnetic field  $\vec{B}_0$  is parallel to the z-axis, and the oscillating magnetic field  $\vec{B}_1(t)$  is parallel to the x-axis:

$$\vec{B}_1(t) = \vec{e} B_1 e^{i\omega t} \quad (3.13)$$

Here  $\vec{e}$  is the vector of unity along the x-axis. The motion of the net magnetism  $\vec{M}(t)$  of the system can be described by the well-known Bloch equations:

$$\frac{dM_z(t)}{dt} = \mu_B g_e (\vec{M}(t) \times \vec{B}(t))_z + \frac{M_0 - M_z(t)}{T_1} \quad (3.14)$$

$$\frac{dM_{x,y}(t)}{dt} = \mu_B g_e (\vec{M}(t) \times \vec{B}(t))_{x,y} - \frac{M_{x,y}(t)}{T_2} \quad (3.15)$$

Here  $\vec{B}(t)$  is the sum of the static  $\vec{B}_0$  and the oscillating  $\vec{B}_1(t)$  fields, and  $M_0$  is the net magnetism of the system in thermal equilibrium under the static field  $\vec{B}_0$ , respectively. In the stationary solution of the Bloch equations the dynamic complex susceptibility,  $\chi = \chi' + i\chi''$  can be introduced, where  $\chi'$  and  $\chi''$  are giving the dispersion-like and absorption-like responses of the system for the external driving force,  $\vec{B}(t)$ . Generally,  $\chi$  is a directly measurable quantity, and its real and imaginary parts can be given by the expressions:

$$\chi' = \chi_0 \omega_0 T_2 \frac{(\omega_0 - \omega) T_2}{1 + (\omega_0 - \omega)^2 T_2^2} \quad (3.16)$$

$$\chi'' = \chi_0 \omega_0 T_2 \frac{1}{1 + (\omega_0 - \omega)^2 T_2^2} \quad (3.17)$$

where  $\omega_0$  is the Larmor frequency. Fig. 3.4 shows  $\chi'$  and  $\chi''$  as functions of the frequency of the driving force. In summary, the spin-lattice relaxation, described by  $T_1$ , allows the continuous detection of microwave absorption in continuous-wave mode EPR experiments, whereas the spin-spin relaxation process with relaxation time  $T_2$  has influence on the linewidth of absorption. Nevertheless, in practice anisotropy and inhomogeneity of the sample also affect the linewidths of EPR signals.

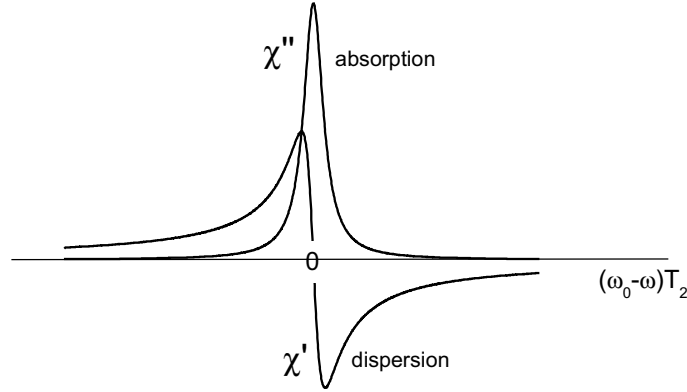


**Figure 3.4** Real and imaginary parts of the magnetic susceptibility representing the dispersion and absorption like response of the system.

### 3.4 The effective spin Hamiltonian

In EPR studies of semiconductors, like SiC, one deals with electrons or holes bound to defects in a crystal of atoms. If this structure is placed in a magnetic field the Hamiltonian will contain a sum of several terms originating from different interactions:

$$\hat{H} = \hat{H}^0 + \hat{H}_Z + \hat{H}_{EX} + \hat{H}_{CF} + \hat{H}_{SO} + \hat{H}_{HF} \quad (3.18)$$

The first term describes the individual Hamiltonian for the electrons or holes together with the defect potential. The second term is the linear Zeeman term, discussed in the previous section. When more than one carrier is bound to the defect  $\hat{H}_{EX}$  accounts for the exchange term, which can be pictured as the interaction between the overlap spin densities of the carriers. Term  $\hat{H}_{CF}$  describes the action of the local crystal field arising from the influence of surrounding atoms through the electric field they produce at the position of the carrier investigated. The magnitude of  $\hat{H}_{CF}$  strongly depends on the actual conditions, e.g. the electrostatic screening effects, and therefore in general the crystal field can be considered as weak, intermediate, or strong. The next term,  $\hat{H}_{SO}$  stands for the spin-orbit interaction between the spins  $S_i$  and the orbital angular momenta  $L_i$ , whereas  $\hat{H}_{HF}$  describes the hyperfine interaction between the spins of carriers bound to the defect and the nuclear spins of the surrounding nuclei of impurities, or crystal host atoms.



### 3.4.1 Spin-orbit coupling

Let us first discuss briefly the spin-orbit interaction. Depending on the relative strength of the terms in Equation 3.13, **LS**-coupling or **JJ**-coupling can occur. When coupling is weak, the spins  $S_i$  of all carriers are coupled to a total spin  $S = \sum_i S_i$ . A similar summation is done for  $L_i$ , and then the total  $S$  and total  $L$  are coupled to a total angular momentum  $J = S + L$ . This procedure is called **LS**-, or Russell-Saunders coupling. In **JJ**-coupling, where the interaction is considerably strong, first the total angular momenta  $J_i = S_i + L_i$  are calculated for all the carriers individually, and then  $J_i$  are summed up to form the total  $J$ . The spin-orbit interaction usually weak for low- $Z$  elements, whereas for high- $Z$  elements gives significant contribution. Since SiC is a compound of two low- $Z$  constituents, here the spin-orbit interaction can be calculated by **LS**-coupling.

### 3.4.2 Fine structure

As Equation 3.5 shows, if  $S = 1/2$  the two energy states due to the linear Zeeman interaction degenerate at zero field. If the system studied has a total electron spin  $S > 1/2$ , Fig. 3.1 suggests the presence of  $2S$  resonance transitions that overlap at any magnetic field i.e. that all the states degenerate at zero field. However, as a fact, in real the degeneracy is lifted and the  $2S$  transitions do not correspond to the same energy at the same magnetic field. To explain this behavior, if keeping the validity of linear Zeeman interaction, than a splitting must be introduced to be present already at zero field as shown in Fig. 3.5 for a system with  $S = 1$ . This splitting is called zero-field splitting. Generally, the zero-field splitting can arise due to the spin-spin interaction,  $\hat{H}_{EX}$ , the local crystal field  $\hat{H}_{CF}$ , as well as the spin-orbit interaction  $\hat{H}_{SO}$  term in Equation 3.18. Here we should not discuss further the physics behind this phenomenon, nevertheless, more details can be found in Ref. [3.5].

When the non-degenerate transitions arise in an  $S > 1/2$  system due to zero-field splitting, the corresponding magnetic resonance line structure in Fig. 3.5 is called fine structure. It can be shown [3.5] that the Hamiltonian, describing such a fine structure pattern can be expressed in mathematical form as:

$$\hat{H}_{FS} = \hat{S}D\hat{S} \quad (3.19)$$

where  $D$  is the fine structure parameter and  $\hat{S}$  is the total spin of the system, respectively (note for systems with  $S > 2$  further terms in Equation 3.19 must also be introduced). Generally, values of the zero field splitting can vary enormously. Sometimes it can be so large is that exceeds the highest Zeeman splitting caused by the magnetic field and then some of the  $\Delta M_S = 1$  transitions may not be observable in EPR (see later, in Section 3.4.4).

To illustrate the strength of different contributions to splitting in zero magnetic field note that calculations in perfect 3C-SiC crystals show a spin-orbit splitting of about 10 meV between p-like electron states at the valence band maximum, whereas in 4H and 6H-SiC it is about 7 meV [3.7, 3.8]. In addition, the uniaxial crystal field present in the hexagonal polytypes, according to calculations, breaks the degeneracy further and leads to zero-field splittings of approximately 70 meV in 4H-SiC and 50 meV in 6H-SiC [3.9], respectively.

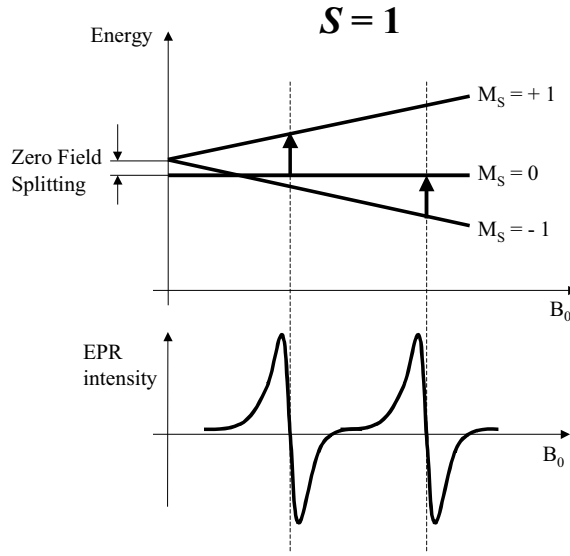


**Figure 3.5** Splitting of a level with a spin  $S = 1$  in a magnetic field. The presence of zero-field splitting leads to the detection of two separated EPR transitions.

### 3.4.3 Hyperfine interaction

The last term in Equation 3.18 is the hyperfine (HF) interaction term. The HF lines have been first observed in paramagnetic resonance by Penrose [3.10] in 1949. The detection of HF structures gives the unique feature of EPR, providing chemical information on the nature of the defect and its surroundings. This interaction couples the spin of the electron or hole bound at the defect to the nuclear spin of the impurity (if present) and the neighboring crystal atoms (the ligands). The Hamiltonian can be written as:

$$\hat{H}_{HF} = \sum_i \hat{S} A_i \hat{I}_i \quad (3.20)$$

where  $\hat{I}_i$  are the nuclear spin operators of the impurity and/or the ligand atoms, and  $A_i$  are the hyperfine interaction parameters. In this thesis we deal only with intrinsic defects containing no impurities, therefore  $\hat{I}_i$  corresponds to ligand host atoms.

If the energetic contribution due to  $\hat{H}_{HF}$  is weaker than the electronic Zeeman term, the HF interaction leads to the additional splitting of every Zeeman component into  $2I+1$  components. In typical EPR experiments, performed in this thesis, the selection rule  $\Delta M_I = 0$  is valid and therefore the observed  $2I+1$  transitions are equally spaced in energy, see in Fig. 3.6 for an  $S = 1/2$ ,  $I = 1/2$  system.

The chemical information can be extracted the following way. The sample consists of atomic species that can exist in several different isotopes. These isotopes differ in the number of neutrons in the nucleus, whereas the number of protons is identical. Therefore the nuclear spin  $I$  depends on the specific isotope. The stable isotopes and their natural abundances are known with a good accuracy, and these abundances are unique for all elements. For example, in SiC, silicon has three different stable isotopes:  $^{28}\text{Si}$  with  $I = 0$  and 92.2 % relative abundance,  $^{29}\text{Si}$  with  $I = 1/2$  and 4.7 % relative abundance, and  $^{30}\text{Si}$  with  $I = 0$  and 3.1 % relative abundance. Consequently, a Zeeman transition is not affected by the presence of  $^{28}\text{Si}$  and  $^{30}\text{Si}$  atoms, whereas the HF interaction with one  $^{29}\text{Si}$  atom gives rise to two HF transitions with equal intensity (see Fig. 3.6). The resulting EPR signal is the sum of these contributions, i.e. the central line and two satellite lines whose intensity is about 2.5 % of the central line.

Concerning the carbon component in SiC, it has two stable isotopes:  $^{12}\text{C}$  with  $I = 0$  and 98.9 % relative abundance, and  $^{13}\text{C}$  with  $I = 1/2$  and 1.1 % relative abundance, respectively. So, the presence of one  $^{13}\text{C}$  in EPR gives rise to two equally spaced satellite lines with a relative intensity of about 0.5 % of the central line. From the different relative intensities of satellite lines the Si and C atoms surrounding a defect can be distinguished.

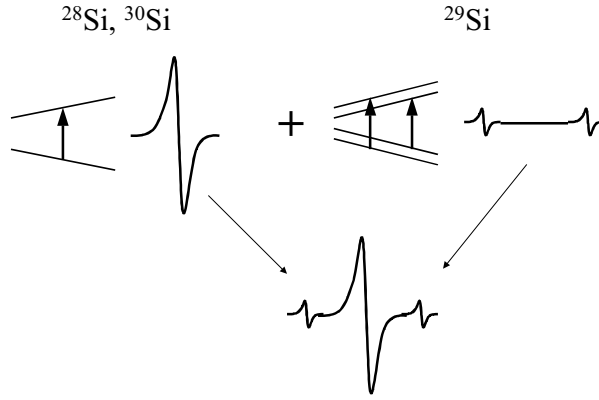


**Figure 3.6** Chemical analysis in EPR. The isotopes  $^{28}\text{Si}$  and  $^{30}\text{Si}$  with  $I = 0$  give rise to one EPR line, whereas for  $^{29}\text{Si}$  with  $I = 1/2$  the signal is split into two components due to the hyperfine interaction. The relative signal intensities are governed by the relative natural abundances of the different isotopes.

#### 3.4.4 The effective spin Hamiltonian formalism

In practice it is difficult to determine the magnetic properties of a particular solid, containing a number of different defects, by starting with *ab initio* models and calculations. Instead, a practical approach is used to describe and classify observations provided by EPR, that is, the introduction of an effective spin Hamiltonian. The main idea is to reverse the above approach and *assign* an effective spin  $S_{\text{eff}}$  to a state such that  $2S_{\text{eff}} + 1$  corresponds to the number of components observed in a magnetic field. An example of the method is shown in Fig. 3.7. Here the splitting of a state with “true” spin  $S = 3/2$  is shown in function of the magnetic field. However, in Fig. 3.7a, the zero field splitting due to the reduced symmetry of the crystal is larger than the highest Zeeman splitting, so that just two microwave transitions can be observed. Here both sets of levels  $M_S = \pm 1/2$  and  $M_S = \pm 3/2$  are assigned to an effective spin of  $S_{\text{eff}} = 1/2$ . In Fig. 3.7b the zero field splitting is much smaller and Zeeman splitting dominates, therefore all four levels have to be considered at the same time. Here the assigned effective spin is  $S_{\text{eff}} = 3/2$ , that is equal to the true spin. If the magnetic field is further increased in case (a), then the Zeeman splitting will become similar to and finally larger than the zero field splitting and we will get to the same situation as for case (b). This shows that the assignment of the appropriate effective spin depends not only on the studied system, but also on the measurement conditions. A typical effective spin Hamiltonian is written as:

$$H_{\text{eff}} = \mu_B B g_{\text{eff}} S_{\text{eff}} + S_{\text{eff}} D S_{\text{eff}} \quad (3.21)$$

where the second term appears only in systems with  $S_{\text{eff}} > 1/2$ . In Equation 3.21  $g_{\text{eff}}$  and  $D_{\text{eff}}$  are empirical and are treated as fitting parameters in order to describe the observed splitting pattern. Hereinafter, when notations  $H$ ,  $g$ ,  $S$  are used, they all will be considered in the effective spin formalism, i.e. as  $H_{\text{eff}}$ ,  $g_{\text{eff}}$ , and  $S_{\text{eff}}$ . For simplicity we also omit operator signs.

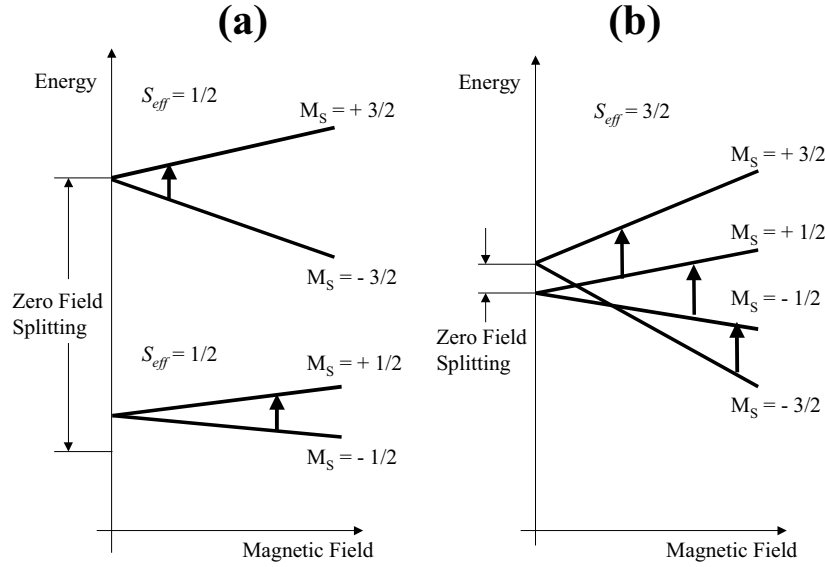


**Figure 3.7** Splitting of a level with a true spin  $S = 3/2$  in a magnetic field. (a) The Zeeman splitting is much smaller than the zero field splitting and only two EPR transitions are detected. (b) The zero field splitting is smaller and all three EPR transitions are detected. The corresponding effective spins are (a)  $S_{eff} = 1/2$  and (b)  $S_{eff} = S_{true} = 3/2$ , respectively.

### 3.4.5 Symmetry properties

Since magnetic interactions are affected by the symmetry properties of the crystal lattice, the Zeeman interaction and the crystal field splitting need no longer to be isotropic in the spin Hamiltonian. Consequently, both  $g_{eff}$  and  $D$  in Equation 3.21 are tensors. However, usually  $g_{xy} = g_{yx}$  and so on, and it is then possible to transform the system to a axis system, called the principle axes, where  $g$  is diagonal and has only three nonzero components,  $g_x$ ,  $g_y$  and  $g_z$ . The same diagonalization can be performed for  $D$  and  $D_x$ ,  $D_y$  and  $D_z$  can be determined. For cubic symmetry,  $D_x = D_y = D_z$  resulting in a corresponding spin Hamiltonian term:

$$H = D_z (S_x^2 + S_y^2 + S_z^2) = D_z S(S+1) \quad (3.22)$$

This interaction shifts all energy levels the same way and will thus have no effect on the EPR spectrum. It is therefore possible to put  $D_x + D_y + D_z = 0$  and the spin Hamiltonian can be reduced to:

$$H = D \left( S_z^2 - \frac{1}{3} S(S+1) \right) + E (S_x^2 - S_y^2) \quad (3.23)$$

where  $D = 3D_z/2$  and  $E = (D_x - D_y)/2$ , giving the axially symmetric and anisotropic parts of the fine structure parameter, respectively.

Generally, all terms in the spin Hamiltonian must be invariant under the point group symmetry operations of the paramagnetic defect that bounds the carrier. For example, if the symmetry is trigonal (that may be  $C_{3V}$  in SiC), the Zeeman term will have axial symmetry around the trigonal axis, i.e. the c-axis of SiC. In this case  $g$  can be described by two different components parallel and perpendicular to the c-axis,  $g_{//}$  and  $g_{\perp}$ , and the Zeeman splitting will

depend on the orientation of the magnetic field with respect to the c-axis. Fig. 3.8 shows the change of the resonant magnetic field in function of the angle  $\Theta$  between  $\vec{B}$  and the c-axis (often called as the angular dependence) for a spin  $S = 1/2$  center in 4H-SiC [3.11]. If the symmetry is lowered further, for example to monoclinic (that should be  $C_{1h}$  in SiC), the number of inequivalent axes is increased, therefore more than one line will arise from the same defect in the EPR spectrum. For some directions of the magnetic field, however, some of these lines might be equivalent and completely overlap. As an example, Fig. 3.9 shows the EPR pattern for a spin  $S = 1/2$  defect center with  $C_{1h}$  symmetry in 4H-SiC [3.12].

In principle, the number of lines and the magnetic field directions for which the lines fall together is different for different symmetries. In this way the symmetry of a defect can be determined by EPR. In addition the number of EPR lines can be doubled, tripled, etc., if the same defect can occupy different inequivalent lattice sites giving rise to slightly different magnetic properties. However, sometimes even the same kind of defect may possess significantly different magnetic features just because it locates at different lattice sites in the crystal.

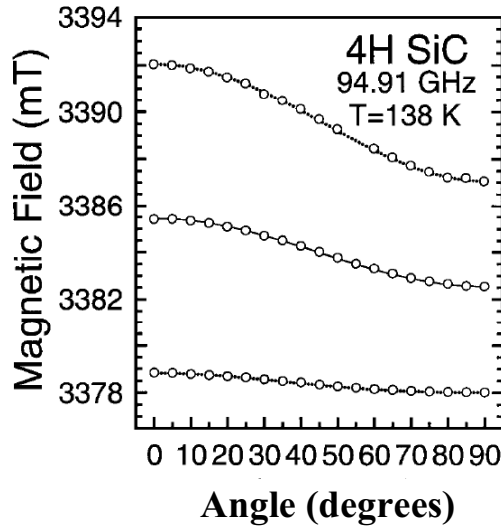


**Figure 3.8** Angular dependence of the resonant magnetic field for a spin  $S = 1/2$  defect center with  $C_{3v}$  symmetry in 4H-SiC [3.10] measured rotating the sample in the (11-20) plane. The central line corresponds to the Zeeman transition between the  $M_S = \pm 1/2$  states, while the two satellites are due to hyperfine interaction with one  $^{29}\text{Si}$  atom. The EPR spectra were recorded at high microwave frequency of 94.91 GHz (W-band) at 138 K.

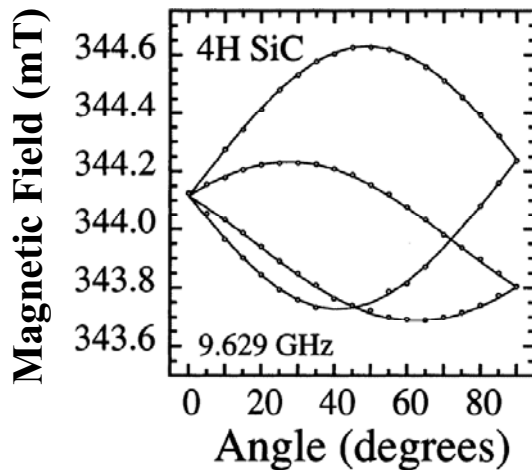


**Figure 3.9** Angular dependence of the resonant magnetic field for a spin  $S = 1/2$  defect center with  $C_{1h}$  symmetry in 4H-SiC [3.12] measured rotating the sample in the [11-20] plane. EPR spectra were recorded at X-band microwave frequency of 9.629 GHz.

In typical EPR experiments performed in this thesis the sample is rotated in the  $[11\bar{2}0]$  plane of the hexagonal SiC system, and the angle  $\theta$  between the magnetic field  $\vec{B}$  and the c-axis is varied from  $0^\circ$  to  $90^\circ$ . This arrangement can be seen in Fig. 3.10. A careful orientation is required since misorientations can make the fitting procedure and analysis of the results very difficult. However, small inaccuracies in the orientation can be taken into account in data evaluation using appropriate computer programs.

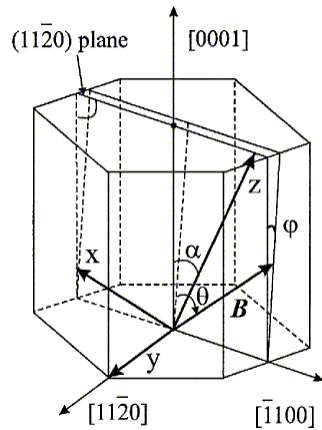


**Figure 3.10** Arrangement in a typical EPR experiment performed on hexagonal SiC structures. The sample is rotated in the  $(11\bar{2}0)$  plane from  $\theta = 0^\circ$  to  $90^\circ$ . The angle  $\alpha$  is measured between the crystallographic  $\langle 0001 \rangle$  axis (the c-axis) and the principal z-axis of the g-tensor, and  $\phi$  is a slight misorientation measured between the sample normal and the exact  $(11\bar{2}0)$  plane.

### 3.4.6 Experimental details

The elements of a simple EPR spectrometer used in this Ph.D. thesis are shown in Fig. 3.11. The microwave radiation is generated by a klystron and via a device, called circulator, fed to the sample along a waveguide. The microwave input power is controlled by an attenuator. The sample is placed in a resonant cavity whose dimensions match the wavelength of the radiation in order to set up a standing wave pattern in it. This efficiently increases the pathlength of the radiation in the sample. The exact resonant frequency of the cavity depends on the electrical properties of the sample and so provision is made for tuning the length of the cavity to some extent. The radiation passes from the waveguide into the cavity through a small hole, the iris. With an appropriate iris setting it can be achieved that all the microwave power entering the cavity is stored therein, i.e. there is no power reflected from the cavity. If the applied scanning magnetic field is now reaches the value required for paramagnetic resonance, microwave power is absorbed by the sample. This changes the matching of the cavity to the waveguide so there is some power now reflected and, via the circulator, reaches the detector. This reflected radiation is the proper EPR signal.

The detector converts the radiation to a D.C. signal which is not readily processed. Therefore the scanning magnetic field is modulated with the help of a pair of small coils mounted outside the cavity. In these coils an alternating current is fed through giving a small oscillating magnetic component that is superimposed on the sweeping static magnetic field (see Fig. 3.3). In our experiments a commonly used modulation frequency of 100 kHz was applied, that is usually optimal in standard EPR measurements. As Fig. 3.3 shows, the output of the detector contains an oscillating component, whose amplitude is proportional to the slope of the absorption line. This component, which can readily be amplified, is taken as the EPR signal. Its phase, relative to that of the signal fed to the modulation coils, depends on

whether the EPR absorption has a positive or negative slope, and by comparing the two in a frequency selective and phase-sensitive detector one can draw out the first derivative of the absorption. This is the so-called lock-in detection technique. Increasing the modulation amplitude will increase the EPR signal intensity until the width of the modulation reaches the natural line width. Further increase of the modulation amplitude leads to distortion of the original line shapes and loss of resolution in multi-line spectra. Thus the detected line width will always be equal or larger than the modulation amplitude.

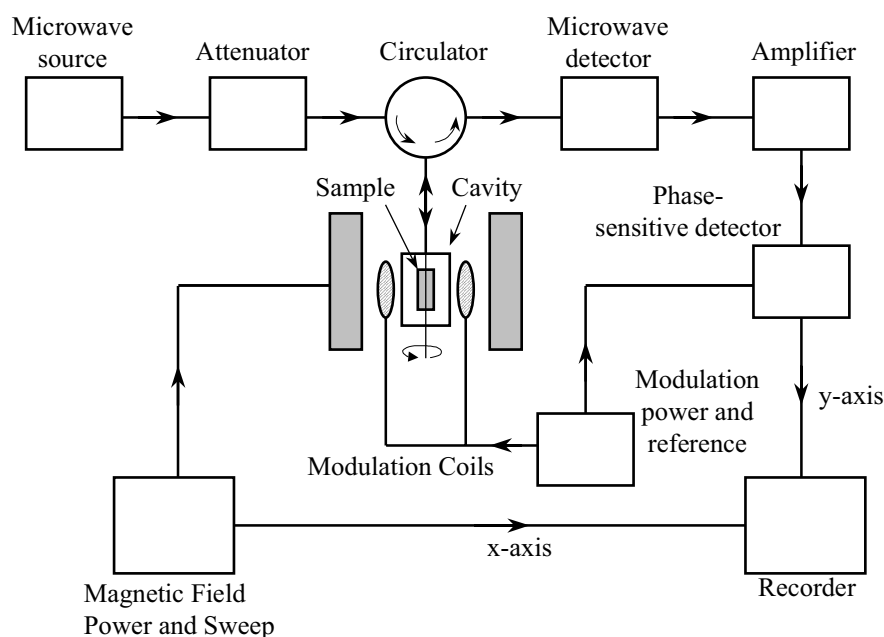


**Figure 3.11** *Schematic of the experimental setup for a conventional continuous wave EPR experiment.*

In this Ph.D. thesis the applied modulation field amplitudes were always kept between 0.01 – 0.1 mT, i.e. 0.1 – 1 Gauss. The EPR experiments have been performed on a Bruker ER-200D X-band (~9.5 GHz) spectrometer equipped with a cylindrical TE<sub>011</sub> microwave cavity with optical access, operating in continuous wave conditions. Measurements have been done at temperature of 77 K by filling the sample holder with liquid nitrogen.

### 3.5 Photo-EPR

Generally, simple EPR technique gives a lot of information about symmetry, localization, and electronic structure of defects, and also offers chemical identification of the atoms surrounding the defects. However, for some charge states of defects, the ground state can be a spin singlet and therefore is not accessible for EPR. One way to overcome this problem is to change the charge state by adding or removing an electron from the defect, in order to make it EPR active. It can be achieved if the sample is illuminated by light with appropriate wavelengths during the EPR measurement. This technique is called photo-EPR. Photo-EPR is appropriate to determine the positions of energy levels introduced by defects in the bandgap. In such experiments, conditions of EPR detection are kept the same and the wavelength of light is scanned in small steps. The light beam can be dispersed by a grating monochromator, filtered by appropriate optical filters and then focused by lenses onto the sample. The principle of a photo-EPR experiment is shown in Fig. 3.12. Assume that the

relaxation energy of the defect structure upon changing its charge state is negligible, i.e. the Franck-Condon effect [3.13, 3.14] does not play role. Now, when the photon energy of the excitation light is equal to  $\Delta E_1$  in Fig. 3.12a, the absorption of electrons from the valence band maximum  $E_V$  to the level  $E_T$  occurs, which induces a change in the EPR intensity, depending on the charge state of the defect. If the spin state of the defect is changing from EPR active to EPR inactive than the EPR intensity decreases (Fig. 3.12b), and vice versa for transitions from EPR inactive to EPR active spin states. When the photon energy is enough to excite electrons from the defect level to the conduction band minimum  $E_C$  (indicated as  $\Delta E_2$  in Fig. 3.12a), a change of EPR intensity opposite to the process of absorption of electrons will be induced. The emission of electrons may change the defect back to its initial charge state to recover the EPR signal (Fig. 3.12b), or oppositely, may decrease the EPR signal. Generally, besides these two main transitions at photon energies  $\Delta E_1$  and  $\Delta E_2$ , one may observe also transitions between the defect level and the levels of shallow donors and acceptors. These additional transitions make defect level studies complicated and therefore a satisfactory photo-EPR analysis requires low impurity concentrations in the sample.

Even though it is possible to use light excitation with above bandgap energy to make the ground states of defects EPR active this is usually not the method of choice. Above bandgap excitation generates a lot of free carriers in the sample, thus changing its conductivity and therefore the microwave field distribution in the cavity. It may then not be possible to tune the cavity to resonance leading to the drop of microwave intensity and making the EPR experiment impossible. On the other hand, if tuning is possible, cyclotron resonance will often dominate in high-purity samples. This process gives an unintentional background to EPR spectra. Still, sometimes above bandgap light is used, e.g. in annealing studies when defect signals are strongly reduced at elevated temperatures. Here the full power of the source, i.e. a wide spectrum of the excitation light is directed on the sample to increase signal intensities (for example white light of a xenon lamp). Note, in photo-EPR experiments discussed in this thesis, the excitation source was a xenon lamp with a power of 150 W.

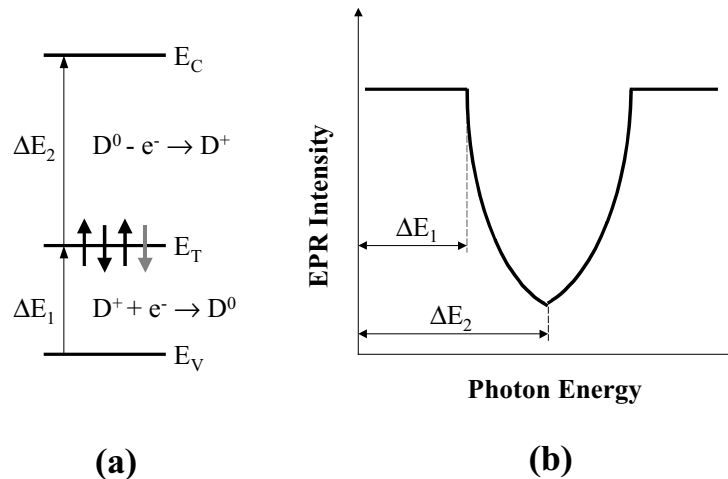


**Figure 3.12** Principle of a photo-EPR experiment involving a deep level  $E_T$  introduced by an EPR active (paramagnetic) defect in the positive charge state,  $D^+$ . (a) Transitions between the deep level and the band edges and (b) the spectral dependency of the photo-EPR intensity of  $D^+$ . Note, four electrons bound to the defect represent the neutral charge state with spin  $S = 0$ , whereas three electrons (marked by black arrows in panel (a)) generate the positive charge state with spin  $S = 1$ , respectively.



### 3.6 Photoluminescence

Results of EPR and photo-EPR experiments can be supplemented with information provided by other optical and magnetic resonance techniques. One of these methods is photoluminescence (PL). In a PL experiment, the semiconductor is illuminated with above bandgap light, generating electrons in the conduction band and holes in the valence band. The crystal in this case no longer in thermal equilibrium, and the excited electrons and holes can relax in several different ways. In the relaxation process the excess energy will be released in the form of phonons, photons, or both. Energy release by phonons is nonradiative relaxation (heat transfer) whereas relaxation by photons is a radiative process. The relative importance of these relaxation channels depends on factors, such as the temperature, and the amount of excess energy that has to be released.

If the energy of the exciting photon is larger than the bandgap energy electrons and holes are created deep in the conduction and valence bands and within a very short time period they relax down to the band minima via phonon emission. The electrons then can radiatively recombine with holes. Different radiative recombination processes are illustrated in Fig. 3.13. Since the electron and hole are oppositely charged they can attract each other and form a bound complex as a quasi-particle, called an exciton. The exciton can be free to move in the lattice, then called a free exciton (Fig. 3.13a), or can be localized to a defect, forming a bound exciton (Fig. 3.13b). Radiative recombination of these electron-hole pairs can take place in both cases. Fig. 3.13c shows a free-to-bound transition, in which the electron or hole relaxes directly from a band edge to a shallow or deep level under emission of a photon. Another process is the so-called donor-acceptor pair luminescence, when capture of an electron to a donor and a hole to an acceptor is followed by their recombination (Fig. 3.13d). The capture of the carrier into an excited state of a deep level defect should also occur and the excess energy of the defect will be released in an internal transition (Fig. 3.13e). Fig. 3.13 obviously shows the importance of defect levels in radiative recombination processes.

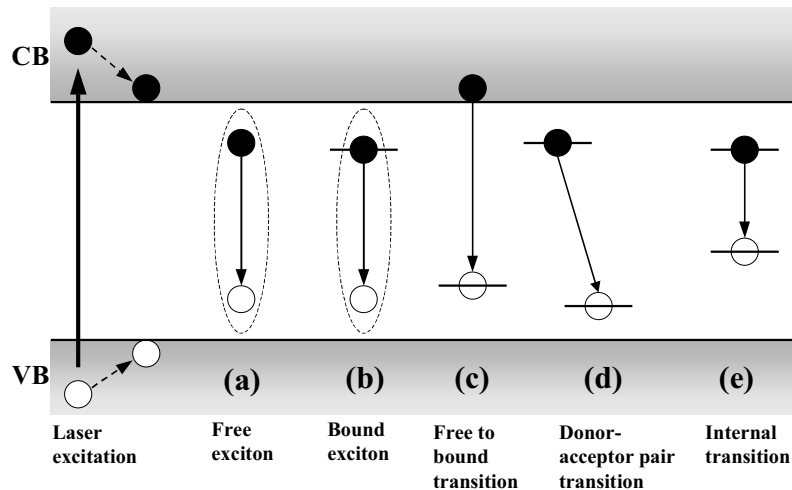


**Figure 3.13** *Schematics of recombination mechanisms observable in photoluminescence (PL).*

Each of these processes has its unique features; in particular the energy of the emitted photons differs. Detecting photons in the function of their energy with the help of a monochromator, a PL spectrum can be obtained. Since defect levels are involved in relaxation

processes, a PL spectrum recorded on a semiconductor provides valuable information about the electronic structure of defects in the material. Moreover, since defect levels can split under external magnetic field, it will be detected as the splitting and shift of the corresponding PL lines (the method is referred to as a Zeeman experiment). In combination with other techniques, (EPR, photo-EPR, etc.) such information can be useful when the spin multiplicity of defect ground or excited states is studied.

Due to the indirect band structure of SiC both energy and crystal momentum ( $\hbar \mathbf{k}$ ) need to be released during a recombination event. However, a photon with bandgap energy in SiC has a very small momentum. Thus e.g. a free exciton transition is usually a phonon-assisted process where the excess momentum is taken away by a crystal phonon with appropriate  $\mathbf{k}$ . When the carriers recombine from more localized states in space such as a bound exciton, the electron-hole wavefunction is more spread out in  $\mathbf{k}$ -space, and therefore has a finite amplitude in  $\mathbf{k} = 0$ . This allows for a no-phonon transition to occur. The corresponding PL line is called no-phonon line, or zero-phonon line (ZPL).

In practice, usually a laser is used as the source for above bandgap excitation in order to achieve enough intensity of the emitted PL radiation. Usually the measurement temperature can be varied from about 1.5 K up to 300 K. Low temperatures are often necessary, because at higher temperatures non-radiative recombination channels become more efficient. In addition, line widths are also increased due to electron-phonon interactions.

There are a lot of other related techniques used in defect characterization. Here we refer only to some of them since the detailed description is beyond the scope of this thesis. An alternative approach of EPR is to monitor the PL intensity due to the recombination at a defect while the magnetic field is scanned in the presence of the microwave field. At magnetic resonance, the PL intensity can be affected, giving rise to a measurable signal. This technique is called Optically Detected Magnetic Resonance (ODMR). Related methods are the spin-sensitive Magnetic Circular Dichroism of Absorption (MCDA) and MCDA-detected EPR. Furthermore, EPR is operating not only in the simple continuous wave mode but can be applied as pulsed-EPR. With the pulsed technique relaxation and dynamic properties of the spin system can be obtained.

Usually in irradiated samples a large number of point defects is created. Some of them exhibit donor or acceptor like behavior and is able to capture electrons or holes. Usually, as-irradiated samples are compensated and the Fermi level is close to midgap. Accordingly, defect charge states whose formation energy is the lowest at midgap are dominant. The paramagnetic defect charge states are EPR active, while diamagnetic states are invisible for EPR. The role of a specific defect in device operation depends on its concentration and the capture or emission cross-section for electrons (holes). In the EPR technique the measure of the absolute defect concentration requires very well calibrated standards and accurate reproducibility of the measurement conditions. Such efforts are seldom made in EPR, however, some example can be found in literature [3.15]. The concentration and the capture cross-section of defects with deep levels can be studied more efficiently by other techniques, like DLTS. Therefore the comprehensive characterization of a defect concerning its charge states, ionization energy levels, atomic structure, concentration, emission and capture cross-sections, and its role in device operation calls for the combination of different experimental techniques, like EPR, DLTS, PL, the measurement of capacitance-voltage (C-V) characteristics and resistivity, positron annihilation spectroscopy (PAS), etc.

## Chapter 4

### EPR of irradiation-induced point defect centers in 4H-SiC

In this chapter my EPR and photo-EPR experiments, performed on electron-irradiated and as-grown 4H-SiC samples are summarized. The 4H-SiC polytype is not only of technological interest, but is also important from the research side. Due to its two different lattice sites, cubic and hexagonal, 4H-SiC allows a particular point defect to have different atomic configurations with different corresponding EPR spectra. This fact can make the discussion of results complicated. However, valuable information can also be obtained in the understanding and modeling of defects. EPR spectra of irradiated 4H-SiC samples usually consist of several lines, originating from different defects, but their analysis is still not so complicated as e.g. for 6H-SiC with three inequivalent lattice sites.

Usually, in irradiated samples an increased number of strong EPR spectra are present as compared to that in as-grown material. However, if a defect is created by irradiation, and is formed also in as-grown samples, it may be dominant in some kind of as-grown wafers and in such case its detailed analysis can be processed.

In section 4.1 the annealing of two EPR centers, labeled as EI5 and EI6, are performed in a wide temperature range from RT to 1600 °C in p-type electron-irradiated 4H-SiC. The EI5 center with its HF structure and deep (+/0) ionization level in the bandgap has been previously attributed to the positively charged carbon vacancy at the cubic lattice site in 4H and 6H-SiC. The low annealing temperature of EI5 was observed by simple EPR technique, whereas from theory a high thermal stability of the defect is expected. Moreover, the EI6 center was attributed to the silicon antisite defect, but its measured HF structure is in contrast with theoretical predictions. Based on my experiments in section 4.1, previous conclusions concerning both the thermal stability of the carbon vacancy and the identification of the EI6 center are revised.

In Section 4.2, a detailed analysis of the P6/P7 EPR centers in electron-irradiated p-type 4H-SiC is given. The P6/P7 centers have been previously identified in 6H-SiC as the carbon vacancy-carbon antisite pairs ( $V_C-C_{Si}$ ). I give the angular dependence analysis for the g-tensor and the fine structure  $D$  tensor of the centers. An attempt has also been made to analyze the hyperfine structure of the centers, however the full description is still lacking due to experimental limitations. I have followed the annealing behavior of the P6/P7 centers that supports the result of theoretical calculations showing the transformation of the Si vacancy into the  $V_C-C_{Si}$  pairs at elevated temperatures.

Section 4.3 deals with a silicon vacancy-related EPR center, labeled as  $T_{V2a}$ . This spectrum can be observed with considerable high intensity in irradiated material, however, usually overlaps with several other spectra, and so far even the number of EPR lines corresponding to the center has not become clear. I observed  $T_{V2a}$  in as-grown, unirradiated, semi-insulating 4H-SiC by photo-EPR. In this case  $T_{V2a}$  was dominating over other signals thus allowing the determination of the number of its EPR lines under light illumination. My EPR experiments, together with previous results of Zeeman experiments on  $T_{V2a}$  taken from the literature, can be explained by a spin  $S = 1$  triplet ground state and an  $S = 0$  singlet excited state of the center.

## 4.1 Annealing behavior of the carbon vacancy in electron-irradiated 4H-SiC

### 4.1.1 Introduction

In this section I briefly summarize the previous results of other research groups that has given the motivation for my EPR experiments on the EI5 and EI6 centers.

Recent EPR studies from several experimental groups have shown the presence of a spin  $S = 1/2$  center with considerably large intensity in electron-irradiated 4H and 6H-SiC. However, the same center often can be observed also in as-grown SiC samples. It has been shown that this so-called EI5 center in irradiated p-type 4H and 6H-SiC [4.1] or the Ky1 center in 6H-SiC [4.2], are similar and related to the positively charged carbon vacancy ( $V_C^+$ ). Photo-EPR experiments by Son [4.3] revealed the ground state of the EI5 center in 4H-SiC to be a deep donor level with the (+/0) level located at  $\sim 1.47$  eV above the valence band ( $E_V$ ). This value agrees well with the calculated (+/0) level of  $V_C^+$  in 4H-SiC [4.4-4.6]. Theoretical calculations of the silicon ligand hyperfine (HF) structure of the center [4.6-4.8] are also in good agreement with the observed experimental values [4.1, 4.2], showing convincingly that the EI5 center is related to  $V_C^+$  at the cubic lattice site in 4H- and 6H-SiC. The calculated geometry of  $V_C$  at the cubic site can be seen in Section 2 in Fig. 2.1a. Table 4.1 summarizes the measured and calculated principal values of the hyperfine tensors  $A$  for the EI5 center and for the carbon vacancy at the cubic site. The measured and calculated (+/0) ionization levels with respect to the valence band maximum are also given. There is no major difference between the HF tensor parameters for the surrounding  $Si_{1-4}$  atoms (for labels 1, 2, 3, 4 see Fig 2.1a) in Table 4.1, i.e. the electron spin giving rise to EPR is nearly equally localized on all four ligand Si atoms.

Another EPR signal usually appears together with EI5. This center, labeled EI6, in irradiated 4H and 6H-SiC has been suggested by Son and his co-workers to be related to the isolated silicon antisite in the positive charge state,  $Si_C^+$  [4.9]. This proposal is based on the fact that a strong HF interaction of the paramagnetic electron with one Si atom has been detected (corresponding to large HF splitting) and this was attributed to the presence of a Si

Principal values of hyperfine tensors in MHz											
Experiment (EI5)				Theory for $V_C^+$ at the cubic lattice site							
Ref. [4.1]				Ref. [4.8]				Ref. [4.6]			
Si <sub>1</sub> :	181.1	125	125	Si <sub>1</sub> :	197	122	114	Si <sub>1</sub> :	182.1	126	126
Si <sub>2-4</sub> :	140.6	103.4	106.7	Si <sub>2</sub> :	155	93	84	Si <sub>2</sub> :	113.8	78.3	77.8
				Si <sub>3,4</sub> :	161	109	103	Si <sub>3,4</sub> :	113.8	78.3	77.8
(+/0) Ionization levels above $E_V$ in eV											
Experiment (EI5)				Theory for $V_C$							
Ref. [4.3]				Ref. [4.5]				Ref. [4.4]			
$E_V + 1.47$				Cub.	$E_V + 1.37$			$E_V + 1.41$			Ref. [4.6]
				Hex.	$E_V + 1.44$			$E_V + 1.53$			$E_V + 1.57$

**Table 4.1** Experimental results for the principal values of the hyperfine tensor and for the position of the (+/0) ionization level of the EI5 center in 4H-SiC, in comparison with calculations for the same properties of the positively charged carbon vacancy  $V_C^+$  in 4H-SiC.

atom in the core of the defect [4.9]. In addition, weaker ligand HF interaction with the surrounding next nearest (NN) Si atoms has also been observed. However, theoretical calculations do not support the  $\text{Si}_\text{C}^+$  model, rather showing  $\text{V}_\text{C}^+$  at the hexagonal lattice site as a promising candidate for EI6 considering its HF tensor parameters [4.6,4.7]. Table 4.2 shows measured HF tensor data for EI6 together with calculations of several groups for  $\text{V}_\text{C}^+$  at the hexagonal site and for  $\text{Si}_\text{C}^+$  at both sites in 4H-SiC. For EI6, only the projections of the HF tensor perpendicular to the c-axis ( $A_{\perp\text{c}}$ ) are available. It can be seen that according to theory of  $\text{Si}_\text{C}^+$ , the electron spin is slightly localized to the central  $\text{Si}_\text{C}$  atom, as well as to all the four ligand  $\text{Si}_{1-4}$  atoms, whereas for  $\text{V}_\text{C}^+$  at the hexagonal site there is a strong localization on one of the ligands,  $\text{Si}_1$ . Also, a significant difference in the ionization (+/0) levels can be seen between  $\text{V}_\text{C}^+$  and  $\text{Si}_\text{C}^+$  from Table 2.1 and 2.2. The calculated geometry of  $\text{V}_\text{C}$  at the hexagonal site and of  $\text{Si}_\text{C}$  is shown in Fig. 2.1b and c, respectively.

It has also not been clear about the annealing properties of  $\text{V}_\text{C}$  in SiC. A preliminary annealing EPR study by Son [4.1] observed the disappearance of the HF lines of the EI5 spectrum at  $\sim 500^\circ\text{C}$ , but detailed annealing data have not been available. Positron annihilation spectroscopy studies of irradiated 6H-SiC by Ling [4.10] showed the presence of a positron trapping center, which disappeared in the  $400\text{--}650^\circ\text{C}$  range and was attributed to  $\text{V}_\text{C}^-$ . Contrary, recent calculations by Bockstedte [4.7] and Rauls [4.11] have shown that  $\text{V}_\text{C}$  with its high migration barriers (4.1-4.7 eV for  $\text{V}_\text{C}^+$  and 5.0-5.8 eV for  $\text{V}_\text{C}^{2+}$ ) is expected to be rather immobile. This condition predicts high annealing temperature of the vacancy.

Since the carbon vacancy is a deep level defect in SiC it should have significant role in carrier trapping processes. The identification as well as the thermal stability of the defect is thus of considerable interest. Accordingly, in the next section I report the annealing behavior

Principal values of hyperfine tensors in MHz											
Experiment (EI6)				Theory for $V_C^+$ at the hexagonal site of 4H-SiC							
Ref. [4.9]				Ref. [4.8]			Ref. [4.6]				
Si <sub>C</sub> :	423	288	288	Si <sub>1</sub> :	400	275	275	Si <sub>1</sub> :	360.5	222.7	222.7
Si <sub>1</sub> :	A <sub>⊥c</sub> : 45			Si <sub>2,4</sub> :	43	22	20	Si <sub>2,4</sub> :	12.9	28	13.3
Si <sub>2,3</sub> :	A <sub>⊥c</sub> : 19			Theory for Si <sub>C</sub> <sup>+</sup> in 4H-SiC (Ref. [4.8])							
Si <sub>4</sub> :	A <sub>⊥c</sub> : 62										
				Cubic site			Hexagonal site				
				Si <sub>C</sub> :	-93	24	22	Si <sub>C</sub> :	-91	25	24
				Si <sub>1</sub> :	10	7	2	Si <sub>1</sub> :	10	5	4
				Si <sub>2</sub> :	-60	17	14	Si <sub>2</sub> :	-56	17	13
				Si <sub>3,4</sub> :	14	5	-11	Si <sub>3,4</sub> :	13	5	-11
Calculated (+/0) ionization levels for Si <sub>C</sub> <sup>+</sup> above E <sub>V</sub> in eV (Ref. [4.4])											
				Cubic site			E <sub>V</sub> + 0.4				
				Hexagonal site			E <sub>V</sub> + 0.43				

**Table 4.2** Experimental results for the principal values of the hyperfine tensor of the EI6 center, in comparison with calculations of the same properties for  $\text{V}_\text{C}^+$  at the hexagonal site and for  $\text{Si}_\text{C}^+$  at both lattice sites of 4H-SiC. Calculated (+/0) ionization levels for  $\text{Si}_\text{C}^+$  are also shown.

of the EI5 and EI6 centers in electron-irradiated 4H-SiC obtained in EPR measurements performed both in dark and under light excitation (photo-EPR).

#### 4.1.2 Experimental details

Samples used in this work were commercial p-type 4H-SiC substrates doped with Al to a concentration of  $\sim 5 \times 10^{17} \text{ cm}^{-3}$  and irradiated by 2.5 MeV electrons at room temperature with a fluence of  $2 \times 10^{18} \text{ cm}^{-2}$ . The samples were annealed isochronally for 5 minutes at each step from 160 °C up to 1200 °C in pure Ar atmosphere. In the range 1200-1600 °C, the annealing was done in a chemical vapor deposition (CVD) setup with 20 minutes annealing time. EPR measurements were performed on a Bruker X-band ( $\sim 9.48 \text{ GHz}$ ) EPR spectrometer at 77 K. In the photo-EPR measurements, a xenon lamp with a power of 150 W was used as the excitation source. Different optical filters were used for below bandgap excitation.

After each annealing step, except 1600 °C, the EPR measurements were performed with similar experimental settings, i.e. sweep width and time, resolution, modulation width, attenuation, and the orientation of the magnetic field with respect to the c-axis. This was done for an adequate comparison of the measured EPR signal intensities.

These experimental details are valid also for the experiments in Section 4.2, and therefore will not be repeated there.

#### 4.1.3 Results and discussion

Fig. 4.1 shows the EPR spectra of the EI5 and EI6 centers after annealing at 350 °C and measured at 77 K in dark with  $\mathbf{B} \parallel \mathbf{c}$ . Even though the central lines of EI5 and EI6 completely overlap at X-band frequency ( $\sim 9.48 \text{ GHz}$ ), some of their HF lines at low-field side are very well separated and therefore the intensity of both centers can be measured without interference (it is true also for  $\mathbf{B} \perp \mathbf{c}$ ). The HF lines of EI5 due to interaction with one  $^{29}\text{Si}$  nuclei at four NN sites are marked by solid arrows. At this orientation of  $\mathbf{B}$  the HF coupling for Si atoms at three from the four NN sites (labeled as  $\text{Si}_2$ ,  $\text{Si}_3$  and  $\text{Si}_4$  Fig. 4.1 and also in Chapter 1 in Fig. 2.1a) are similar and therefore their HF lines overlap.

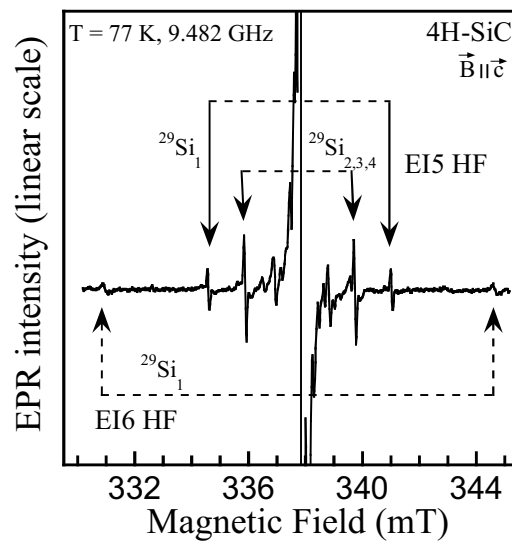


**Figure 4.1** EPR spectra of the EI5 and EI6 centers in electron-irradiated p-type 4H-SiC measured in dark with the magnetic field  $\mathbf{B} \parallel \mathbf{c}$  after annealing at 350 °C.

The HF splitting for  $\text{Si}_1$  at the fourth NN site is the largest, and its HF line is separated from that of  $\text{Si}_2$ ,  $\text{Si}_3$ , and  $\text{Si}_4$ . A slight misorientation from  $\mathbf{B} \parallel c$  leads to the splitting of the overlapping HF lines, and the splitting is very sensitive for the degree of misalignment. Accordingly, to find identical measurement conditions when placing the sample into the resonance cavity after each annealing step is a complicated task. Therefore in my study the intensity of the HF lines of EI5 and EI6 in function of the annealing temperature was measured with  $\mathbf{B} \perp c$ . In this case two of the four HF lines are well separated and just the remaining two overlap (see Fig. 4.2). In addition, the splitting is not as sensitive for slight misalignments than for  $\mathbf{B} \parallel c$ .

Fig. 4.2 shows EPR spectra in electron-irradiated 4H-SiC before and after annealing at different temperatures measured at 77 K for the magnetic field  $\mathbf{B}$  perpendicular to the  $c$ -axis of the hexagonal crystal. The EPR spectrum in as-irradiated sample is shown in Fig. 4.2a. The strongest line consists of two overlapping signals of EI5 and EI6.

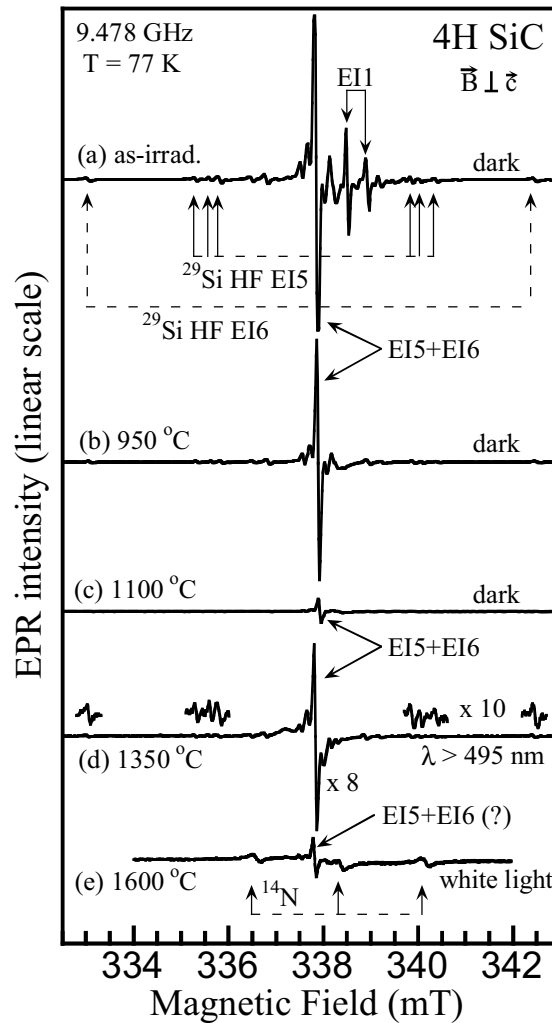


**Figure 4.2** EPR spectra in electron-irradiated *p*-type 4H-SiC measured before and after annealing at different temperatures: (a)-(c) in dark and d) under illumination of light ( $\lambda \geq 495$  nm) in  $\times 8$  scale. The insets (in  $\times 10$  scale) show the HF lines of EI5 and EI6. (e) The central line of EI5 and EI6 and the signal of the N donor measured under white light excitation in the sample annealed at 1600 °C.

The HF lines of the EI5 center due to the interaction with a  $^{29}\text{Si}$  atom ( $I = 1/2$ , 4.7% natural abundance) occupying four nearest neighbor sites are marked by solid arrows. Dashed arrows indicate the large-splitting HF lines corresponding to the interaction with one  $^{29}\text{Si}$  atom of the EI6 center.

In addition to the EI5 and EI6 signals, the spectrum of the EI1 center [4.12] (Fig. 4.2a) and a weak line of unknown origin at  $\sim 338.2$  mT are also observed. EI1 is annealed out at relatively low temperature ( $\sim 250$  °C) [4.12] and has recently been suggested to be related to the carbon split-interstitial [4.6, 4.7]. After annealing at 950 °C (Fig. 4.2b), EI5 and EI6 signals are still clearly detected, whereas other spectra almost disappear. The intensity of the central line decreases significantly and no HF lines could be detected in dark after a 1100 °C anneal (Fig. 4.2c). After annealing at 1350 °C, the central line of the EI5 and EI6 spectra become almost undetectable in dark, but can be observed even with their clear HF structures under light illumination, as can be seen in the inset of Fig. 4.2d. At higher annealing temperatures, only the central line can still be detected under above-bandgap light illumination, see e.g. the spectrum in Fig. 4.2e measured under white light excitation after a 1600 °C anneal. Without observing the HF lines, the identification of the central line become complicated, however, the angular dependence measured at X-band frequency confirms that it is still from EI5 and EI6 or either one of them. The spectrum of the N donor consisting of three equidistant lines with characteristic splitting of 1.8 mT is also detected and marked by solid arrows in Fig. 4.2e.

Figures 4.3a and 4.3b show the EPR intensity of the HF lines of the EI5 and EI6 spectra measured in dark (solid symbols) and under illumination with light of wavelengths  $\lambda \geq 530$  nm (open symbols) as a function of annealing temperature. These intensity values are normalized to the EPR intensities measured in dark in the unannealed sample. The decrease of EPR intensities was observed already at annealing temperatures between 160-400 °C in measurements performed in dark as well as under light illumination. Here the EI5 signal drops by  $\sim 43$  % (or  $\sim 48$  % if measured under illumination), whereas the corresponding decrease of the EI6 signal is  $\sim 44$  % ( $\sim 46$  %). This annealing stage of EI5 may be explained as due to (i) the recapture of interstitials to  $V_C$  and (ii) a slight shift of the Fermi level ( $E_F$ ) (caused by the reduction of the  $V_C$  concentration as well as the annealing of other centers, e.g. EI1 [4.12]) makes it less favorable to observe the EPR signal.

Annealing temperatures in the range 400-950 °C has almost no effect on both the centers. Above 1000 °C a rapid reduce of the EI5 and EI6 signals can be observed (solid symbols in Fig. 4.3). However, under light illumination even after annealing at 1100°C the HF lines can be detected with nearly the same intensities as before (open symbols in Fig. 4.3). This suggests that the decrease of signal intensities between 950-1100 °C as measured in dark is not really due to the annealing of the corresponding defects but caused by the change of the Fermi level. This is expected to occur when the silicon vacancy ( $V_{Si}$ ) is annealed out in the temperature range 700-900 °C [4.13] to form  $V_C$ - $C_{Si}$  pairs [4.14]. In our samples, the concentration of  $V_C$ - $C_{Si}$  pairs is found to reach the maximum at  $\sim 850$  °C and drops to zero at  $\sim 1100$  °C (see in Section 4.2). Due to the annealing of these defects,  $E_F$  may shift to a position, which is not suitable for the detection of EI5 and EI6 signals, and therefore light illumination is required for observation of the defects in their paramagnetic state.



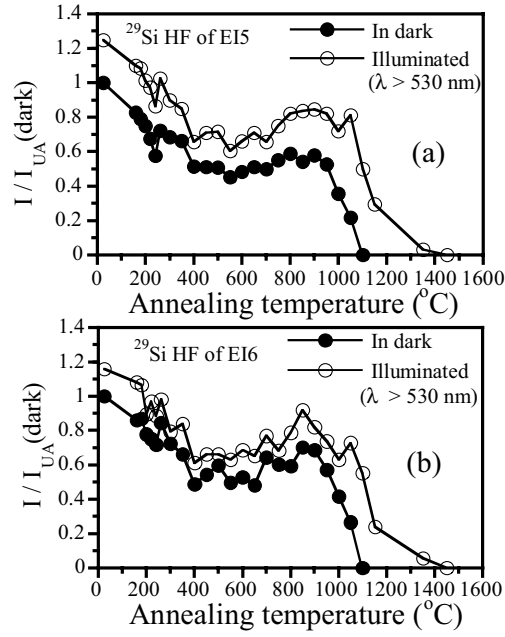


**Figure 4.3** EPR intensity of the low-field  $^{29}\text{Si}$  HF lines of the (a) EI5 and (b) EI6 centers in electron-irradiated 4H-SiC measured in dark (solid symbols) and under illumination with light (open symbols) as a function of annealing temperature. The intensity values are normalized to the EPR intensities measured in dark in the unannealed sample ( $I_{UA}(\text{dark})$ ). Data for the 1600 °C anneal are measured in different conditions and therefore not included.

Increasing the annealing temperature, between 1100-1600 °C leads to the decrease of both the EI5 and EI6 signals, however, the tendency is quite moderate. The reduction of the EPR signals at this annealing temperature range could also be partly due to lower efficiency of the photo-excitation when  $E_F$  moves far away from the defect levels. (It will be more and more difficult to pump (or remove) electrons to (or from) the defect level and to keep the defect in its paramagnetic state long enough to be detected by EPR.) Indeed, the spectrum in Fig. 4.2e can only be detected when using white light with the full power of the lamp. It seems that in the range 1100-1600 °C,  $V_C$  becomes mobile and its second annealing step starts. It should happen either by sublattice migration, or by subsequent hop between the Si and C sublattices, leaving behind clusters of antisite pairs. However, as shown by theoretical calculations, the latter process requires a higher energy compared to that of the former one and is therefore unlikely to happen [4.11]. The migration of  $V_{Si}$  via nearest jump to form  $V_C-C_{Si}$  pair requires lower energy and the process can continue, leading to the formation of larger  $V_C$ -antisite clusters [4.11]. At high temperatures,  $V_C$  can be dissociated from the cluster and moves away. Finally, the  $V_C$  migration may end up in vacancy clusters or at surfaces. The above processes may involve many steps and therefore require more time. This may explain a gradual decrease of the EI5 signal between 1100-1600 °C. Since we cannot estimate the influence of the Fermi level change on the intensity of EI5 and EI6, a detailed annealing behavior of the centers in this temperature range could not be obtained. However, the shift of  $E_F$  could be the reason for the previously reported low annealing temperature of  $V_C$  (450-500 °C) in Ref. 1 and such influence cannot be eliminated even using light illumination as in my study.

Fig. 4.3 shows the similar annealing behavior of EI5 and EI6 signals in dark as well as under light illumination. Such a similarity is not expected if EI6 is related to  $\text{Si}_C^+$  as it is suggested in Ref. [4.13]. This annealing behavior supports the theoretical calculations [4.8, 4.15], which suggest that the EI6 center is the  $V_C^+$  at the hexagonal lattice site. As shown in Fig. 4.3, the light illumination causes a rise of 30-45 % in the EI5 signal whereas it induces an increase of the EI6 signal by 10-30 % (in the temperature range below 950 °C), indicating that the ionization energy levels of the centers are different. This is consistent with theoretical

calculations [4.4, 4.5], showing the (+/0) level to be located ~0.1 eV higher in the bandgap for the C vacancy at the hexagonal site than for the cubic site (see Table 4.1).

#### **4.1.4 Conclusions**

In summary, I have performed annealing studies of the EI5 and EI6 centers in electron-irradiated 4H-SiC using EPR and photo-EPR. I have found the carbon vacancy is stable at temperatures much higher than that previously reported. The defect seems to become mobile at temperatures above 1100 °C but still survives annealing temperature of 1600 °C. Neglecting the influence of the Fermi level change on the EPR detection of these defects, it can be concluded that both centers have similar annealing behaviors and therefore the EI6 center may be the positively charged carbon vacancy at the hexagonal lattice site of 4H-SiC.

Note that in a recent parallel work, reported by Umeda et al. [4.16], a detailed analysis of the spin Hamiltonian parameters of EI5 and EI6 has also lead to the conclusion that EI6 is related to  $V_C^+$ . These works together with theoretical calculations reveal that the atomic structures of the two types of  $V_C^+$  in 4H-SiC are greatly different as it is shown in Fig. 2.1.

Note, in a work of the SiC research group at IFM, Linköping University we have shown that under growth conditions leading to a somewhat favored incorporation of acceptors, the EPR spectra are dominated by the deep donors EI5 and EI6 [4.17]. The resistivity of such crystals have an activation energy of  $1.4 \pm 0.1$  eV, which correlates well with the position of the  $V_C^+/V_C^0$  deep level [4.3]. Since high resistivities of  $10^{10}$ - $10^{11}$   $\Omega\text{cm}$  can be kept even after 1600 °C annealing [4.17], the carbon vacancy, with its high thermal stability, is probably one of the dominant defects giving rise to semi-insulating properties of SiC substrates. Therefore the growth of  $V_C$ -rich SI-SiC wafers seems to be a possible way to increase performance of devices processed on semi-insulating SiC substrates.

## **4.2 The carbon vacancy-carbon antisite pairs in electron-irradiated 4H-SiC**

### **4.2.1 Introduction**

It has been known since many years that high-energy particle irradiation induces many intrinsic defects with spin  $S=1$  in hexagonal SiC polytypes [4.18]. Some of these and other new defects were also detected by electron paramagnetic resonance (EPR) in as-grown 6H-SiC after heat treatment at high temperatures and attributed to different configurations of vacancy pairs [4.19]. Among these defects, the P6/P7 centers in 6H-SiC [4.14] were later identified to be different configurations of the carbon vacancy-carbon antisite pair in the +2 charge state  $(V_C-C_{Si})^{2+}$  (Ref. 4.14). The paired defect is formed after irradiation and a subsequent annealing [4.20] and was also detected by optically detected magnetic resonance (ODMR) in as-grown 6H-SiC without any thermal treatment [4.20]. This is expected since SiC crystals are usually grown at high temperatures ( $\sim 1600$  °C in epitaxial growth by chemical vapor deposition (CVD) or above 2000 °C in sublimation techniques) and during the cooling down process after growth, vacancies can interact with other intrinsic defects to form associated complexes. Theoretical calculations suggested that the  $V_C-C_{Si}$  pairs have lower formation energies than that of the isolated silicon vacancy ( $V_{Si}$ ) and can be formed via the process of trapping a C atom neighbor by a  $V_{Si}$  [4.14, 4.21]. However, the defect formation and its annealing behavior have not been experimentally studied.

It is surprising that the defect has so far not been detected in irradiated 4H-SiC although most of the recent magnetic resonance studies were performed in this polytype. Recently, several EPR spectra, with spin  $S=1$  have been observed in high-purity semi-insulating (HPSI) 4H-SiC under illumination with light of photon energies  $h\nu \geq 1.15$  eV [4.22]. The similarity between these spectra and the P6/P7 spectra in 6H-SiC at main directions leads to the suggestion that they belong to the same defect [4.22]. (The labels P6/P7 are therefore adapted for these centers in 4H-SiC [4.22].) However, their parameters and the ligand hyperfine (HF) interaction have not been analyzed and no HF interaction with the antisite  $^{13}\text{C}$  atom was observed. The P6/P7 centers were found to have a concentration comparable with that of shallow dopants in HPSI 4H-SiC substrates and were suggested to be responsible for the high resistivity of the material [4.22].

In this section, I present the angular dependence analysis of the g-tensor and of the fine structure tensor  $D$  in 4H-SiC, irradiated with 2.5 MeV electrons to a fluence of  $2 \times 10^{18} \text{ cm}^{-2}$ . The HF structure detected with  $\mathbf{B} \perp c$  shows the HF of the  $^{13}\text{C}$  antisite of the P6/P7 spectra in 4H-SiC that is in agreement with the model of  $V_C-C_{Si}$  pairs. My annealing study in electron-irradiated material showed that the P6/P7 centers increase their intensity in the temperature range 600-850 °C and are not detectable after an 1100 °C anneal. This behavior supports theoretical models predicting the transformation of  $V_{Si}$  into  $V_C-C_{Si}$  pairs at elevated temperature.

Now I skip the experimental details, since it is already given in Section 4.1.2. A brief summary of data evaluation is given in Appendix 1.

### **4.2.2 Results and discussion**

The EPR spectra in p-type e-irradiated 4H-SiC and subsequently annealed at 850 °C for 5 minutes measured at 77 K under illumination with light of photon energies  $h\nu \geq 1.2$  eV for the magnetic field  $\mathbf{B}$  along the c-axis are shown in Fig. 4.4.

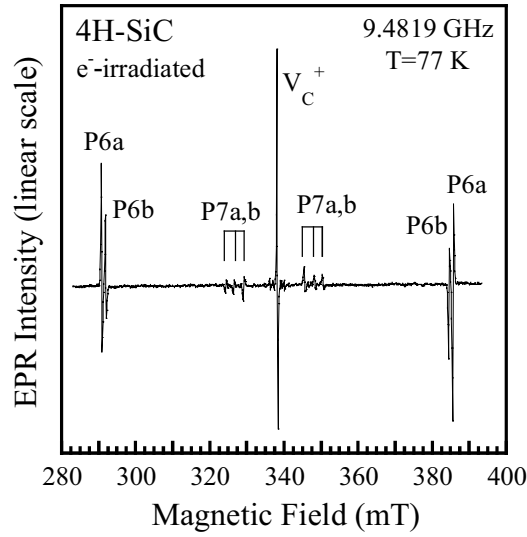


**Figure 4.4** EPR spectra in *p*-type 4H-SiC irradiated by 2.5 MeV electrons and annealed at 850 °C. The measurement has been performed at 77 K under illumination of light with wavelength  $\lambda \geq 840$  nm for  $\mathbf{B}$  parallel to the *c*-axis.

In addition to the strong signal of the positively charged carbon vacancy ( $V_C^+$ ) [4.1], several pairs of lines labeled P6a,b and P7a,b were detected. The angular variations of these spectra as measured with rotating  $\mathbf{B}$  in the  $(11\bar{2}0)$  plane are plotted in Fig. 4.5. As can be seen in this figure, the P6/P7 lines belong to different spectra with an effective electron spin  $S=1$ . The angular dependencies of the P6a and P6b are typical for a spin  $S=1$  center with  $C_{3v}$  symmetry characterized by the largest zero-field splitting at the magnetic field direction along the *c*-axis. The P7a,b centers have  $C_{1h}$  symmetry with the zero-field splitting comparable to that of the P6a,b but being largest at the angle of  $\sim 70$  degrees off the *c*-axis (Fig. 4.5). The angular dependencies of the P6/P7 centers can be described by the following spin-Hamiltonian:

$$H = \mu_B \mathbf{B} \cdot \mathbf{g} \cdot \mathbf{S} + D \left( S_z^2 - \frac{1}{3} S(S+1) \right) + E(S_x^2 - S_y^2) \quad (4.1)$$

with an effective electron spin  $S=1$ . Here  $\mu_B$  is the Bohr magneton. In the principal axes coordinate, the *x* and *z* axes lie in the  $(11\bar{2}0)$  plane and the *y*-axis is along the  $\langle 11\bar{2}0 \rangle$  direction. The angle between the principal *z*-axis and the *c*-axis of the hexagonal crystal denotes as  $\alpha$ , for illustration see Fig. 3.10 in the previous chapter.  $D$  and  $E$  are the fine structure parameters of the axial and orthorhombic fields, respectively, and defined as  $D = 3D_z/2$  and  $E = (D_x - D_y)/2$ . The symmetry is  $C_{3v}$  for the P6a,b centers and  $C_{1h}$  for the P7a,b centers. The best fits give the same *g*-value  $g = 2.003$  for all the centers. The principal *z*-axis of the fine structure tensor  $\mathbf{D}$  is along the *c*-axis for the P6a and P6b centers whereas it is about 70 degrees off the *c* direction for the P7a and P7b centers. That is, in principle, close to the tetrahedral bonding direction with an ideal value of  $70.529^\circ$ , see Fig. 1.1 in Chapter 1. The spin Hamiltonian parameters, deduced from the fits are given in Table 4.3. The simulated angular dependencies using these parameters and Equation 4.1 are plotted in Fig. 4.5 as dotted lines. In the simulations, a sample misalignment of 1.5 degrees off the *c*-axis toward the  $\langle 11\bar{2}0 \rangle$  direction was included to account for the small splitting of the P7a,b lines at the angles close to the direction of the *c*-axis. As can be seen in Table 4.3, the parameters of these

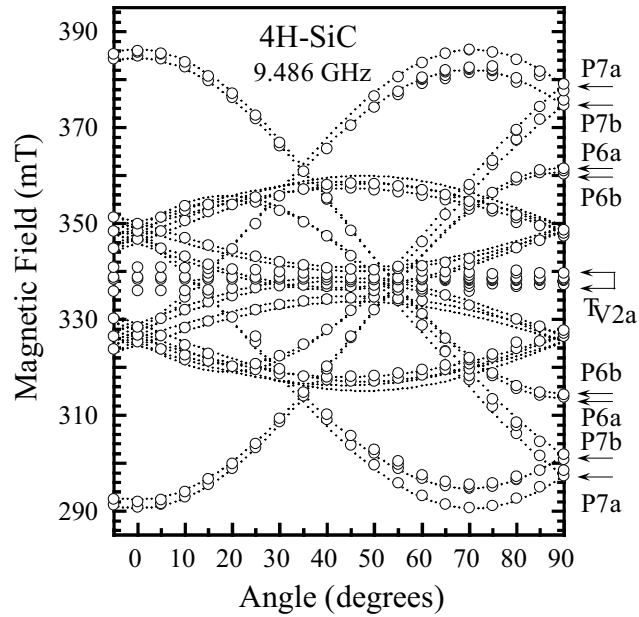


**Figure 4.5** Angular dependencies of the P6/P7 spectra in 4H-SiC. The curves represent the simulations using the parameters in Table 4.3 and the spin Hamiltonian Equation 4.1. A sample misalignment of  $1.5^\circ$  off the  $c$ -axis toward the  $\langle 11\bar{2}0 \rangle$  direction is included in the simulation.

	Center	$g$	$D$ [ $10^{-4} \text{ cm}^{-1}$ ]	$E$ [ $10^{-4} \text{ cm}^{-1}$ ]	$\alpha$ [degrees]	Symmetry
4H	P6a	2.003	447	0	0.0	$C_{3v}$
	P6b	2.003	430	0	0.0	$C_{3v}$
	P7a	2.003	447	105	71	$C_{1h}$
	P7b	2.003	408	90	70	$C_{1h}$
6H	P6a	2.003	456	0	0.0	$C_{3v}$
	P6b	2.003	447	0	0.0	$C_{3v}$
	P6c	2.003	430	0	0.0	$C_{3v}$
	P7a	2.003	449	-4	71.2	$C_{1h}$
	P7b	2.003	441	46	70.0	$C_{1h}$
	P7c	2.003	416	-1	70.5	$C_{1h}$

**Table 4.3** Spin Hamiltonian parameters of the P6/P7 centers in 4H-SiC.  $\alpha$  is the angle between the principal  $z$ -axis and the  $c$ -axis. The parameters for P6/P7 centers determined in Ref. [4.14] for 6H-SiC are also given for comparison.

centers are very close to that of the P6/P7 centers in 6H-SiC [4.14]. I used light illumination with different photon energies but only observed two  $C_{3v}$  centers (P6a and P6b) and two  $C_{1h}$  centers (P7a and P7b) in 4H-SiC. In 6H-SiC, three different centers were observed for each symmetry type [4.14].

Figure 4.6a shows the low field lines of the P6a and P6b spectra in irradiated 4H-SiC after annealing at  $850^\circ \text{C}$  measured under illumination with light of wavelengths  $\lambda \geq 840 \text{ nm}$  for  $\mathbf{B}$  parallel to the  $c$ -axis. Both the P6a and P6b lines have two inner broad HF lines with the splitting of about  $0.4 \text{ mT}$  (indicated by arrows in Fig. 4.6).

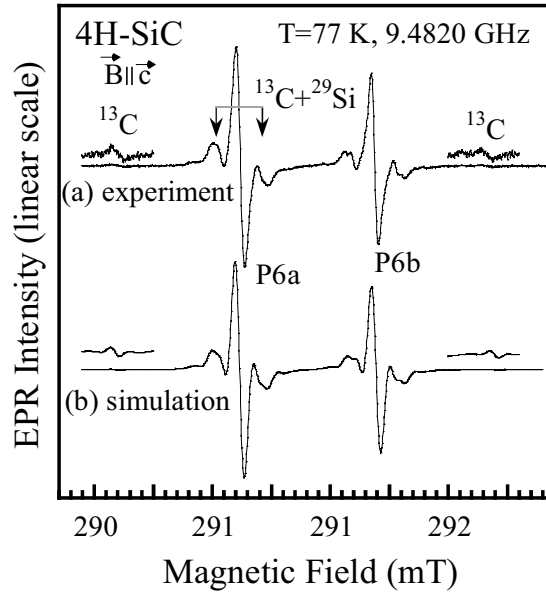


**Figure 4.6:** (a) A part of the P6a and P6b spectra measured for  $\mathbf{B} \parallel \mathbf{c}$  axis showing the HF structure due to the interaction with the nearest neighbor C and Si atoms and with the C antisite (shown in extended scale in the inset). (b) The simulation using HF parameters (with values see in the text) with the line width of 0.8 G and the line shape determined by the ratio Lorentzian/Gaussian of 0.6.

At this angle of the magnetic field, the HF lines of the P6b are a bit broader and a very small splitting could be seen, indicating an overlapping of different HF signals. Very weak outer HF lines were also detected at each side of the P6a and P6b lines. The distance between the HF and the central line is about 1.05 mT for P6a and  $\sim 0.95$  mT for the P6b line, which corresponds to the HF splitting of  $\sim 2.10$  mT and 1.90 mT, respectively. Their intensity is about 0.6-0.7 % of that of the central line. This intensity ratio is approximately a half of the natural abundance of one  $^{13}\text{C}$  atom ( $I=1/2$  and a natural abundance of 1.11 %). These outer HF lines are therefore attributed to the HF structure due to the interaction with a single  $^{13}\text{C}$  nucleus. The HF structure is similar to that observed in 6H-SiC, but with a slightly larger splitting ( $\sim 59$  MHz and  $\sim 53$  MHz for the P6a and P6b centers, respectively, in 4H-SiC as compared to a value of 48 MHz in 6H-SiC (Ref. 4.14)). Note that the HF structures of the P7a,b signals are very similar but much weaker and the HF interaction with the  $^{13}\text{C}_{\text{Si}}$  was not observed.

In general, the P6/P7 centers can be detected with considerably high intensity only under light illumination with  $h\nu \geq 1.15$  eV both in 4H and 6H-SiC. The EPR line intensity also depends on the orientation of the magnetic field, and is strongest for  $\mathbf{B} \parallel \mathbf{c}$ . Rotating the sample in the  $[11\bar{2}0]$  plane toward  $\mathbf{B} \perp \mathbf{c}$  the intensity significantly decreases and already for an off-axis  $10^\circ$  the HF structure no longer can be detected. These conditions do not allow the measurement of the angular dependence of the HF lines and the overlapping inner HF structures cannot be resolved.

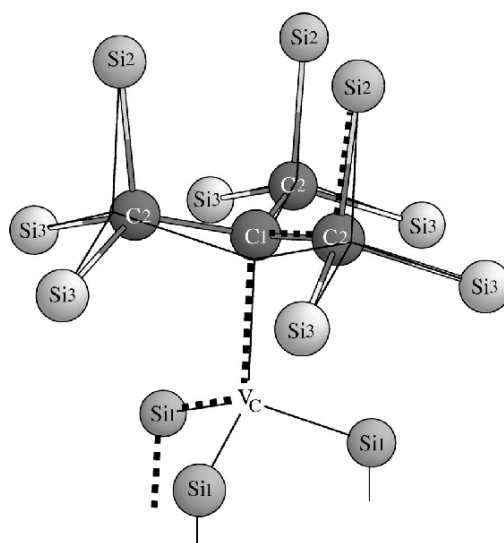


**Figure 4.7** Calculated relaxed structure of the  $V_C$ - $C_{Si}$  pair oriented along the  $c$ -axis of SiC (i.e. the P6 center) taken from Ref. 4.14. The thin lines mark the position of the bonds in the ideal lattice. The dashed line represents the  $(11-20)$  plane.

In 6H-SiC, the inner HF lines were attributed to the HF interaction with 4 to 8 Si atoms [4.14]. The number of Si atoms was estimated in order to account for the intensity ratio of about 15% for each HF line [4.14] without considering the interaction with C atoms in the nearest neighbor (NN) and next nearest neighbor (NNN) shell. However, an alternative interpretation can also be given. Fig. 4.7 illustrates the calculated atomic structure of the  $V_C$ - $C_{Si}$  pair, taken from Ref. 4.14. As can be seen, there should be HF interactions with: (i) 3 Si NN atoms of the  $V_C$ , (ii) 3 C NN atoms of the  $C_{Si}$ , (iii) 9 Si NNN atoms of the  $C_{Si}$ , and (iv) 9 C NNN atoms of the  $V_C$ . Fig. 4.6b shows the simulated P6a and P6b signals including the HF interaction with the above mentioned neighbor atoms. In the simulation performed by the WinEPR program [<http://www.bruker-biospin.com/brukerepr/winsimulation.html>], HF parameters of 4.2 G, 4.25 G, 2.7 G, and 3.9 G were used for (i), (ii), (iii), and (iv) in case of the P6a center. The corresponding HF parameters were assumed as 4.35 G, 4.4 G, 2.7 G, and 3.9 G for the P6b center. The line width was set to 0.8 G, and the line shape was determined by the ratio Lorentzian/Gaussian of 0.6. As can be seen, the simulation well reproduces the measured intensity ratios of the P6a and P6b signals.

Since the unresolved HF structure gives rise to different possible interpretations, for the unambiguous assignment of the HF lines the measurement of the full angular dependence is required. However, currently such measurements and the comparison with the results of theoretical calculations are not accessible.

Based on their  $g$  and  $D$  tensor parameters, which are similar to that have been reported for the P6/P7 centers in 6H-SiC, following Lingner's [4.14] identification I conclude that the observed P6a and P6b spectra are related to the  $V_C$ - $C_{Si}$  pairs in 4H-SiC. The detected number of EPR spectra is in agreement with the number of inequivalent lattice sites in the 4H polytype. The measured relative intensities of the HF lines with respect to the central lines for  $B \parallel c$  can be interpreted within the  $V_C$ - $C_{Si}$  model, however in this case further investigations are required.

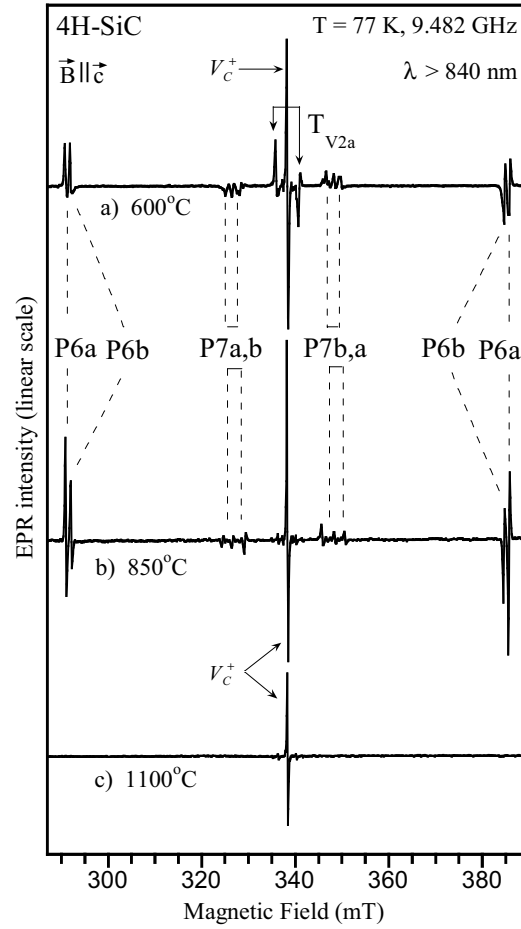


**Figure 4.8** EPR spectra in p-type electron-irradiated 4H-SiC measured after annealing at a) 600 °C, b) 850 °C, and c) 1100 °C under light illumination with wavelengths  $\lambda \geq 840$  nm

Fig. 4.8a-c show EPR spectra in irradiated 4H-SiC measured at 77 K with  $\mathbf{B} \parallel \mathbf{c}$  under light illumination with wavelengths  $\lambda \geq 840$  nm at different annealing temperatures. Fig. 4.8a shows EPR spectra observed after annealing the sample at 600 °C. In addition to the P6/P7 centers, the  $V_C^+$  signals, and the silicon vacancy related  $T_{V2a}$  center [4.23] were also detected. Increasing the annealing temperature, the P6/P7 signals increase and reach their maximum intensities after annealing at  $\sim 850$  °C (Fig. 4.8b), then decrease and completely vanish after annealing at 1100 °C (Fig. 4.8c). The  $T_{V2a}$  center cannot be observed after an 850 °C annealing (Fig. 4.8b). The dependence of the intensity of P6/P7 and of  $T_{V2a}$  on the annealing temperature is plotted in Fig. 4.9. The  $T_{V2a}$  signal anneals out between 600 and 700 °C, whereas the P6/P7 signals increase by a comparable amount between 600 and 850 °C.

This annealing behavior in irradiated material is in agreement with the theoretical calculations [4.11,4.14,4.21] on the migration of vacancies and the formation of vacancy-antisite complexes. The annealing of  $V_{Si}$  takes place at temperature range 600-700 °C [4.13] when a nearest C neighbor (marked as the C1 atom in Fig. 4.6) can jump into the  $V_{Si}$  to form a  $V_C-C_{Si}$  pair and thus to increase the P6/P7 signal intensities. At higher annealing temperatures (above 850 °C), the  $V_C-C_{Si}$  pairs dissociate and can be transformed to either  $V_{Si}$  or complexes of  $V_C$  and antisite clusters [4.11].



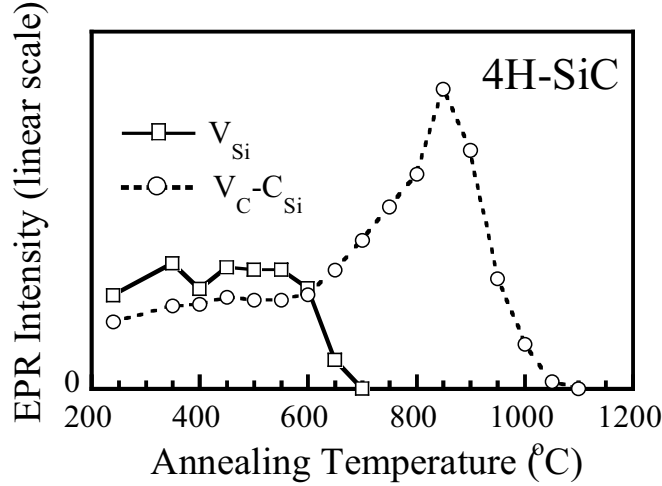


**Figure 4.9** EPR intensity of the  $V_C-C_{Si}$  pairs (the P6 centers) and of the  $V_{Si}$ -related  $T_{V2a}$  center as a function of annealing temperature in electron-irradiated p-type 4H-SiC.

Note that our annealing studies in as-grown SI 4H-SiC samples (performed by the SiC group at IFM, Linköping; not presented here) showed that SI samples with strong signals of the  $V_C-C_{Si}$  pair still have very high resistivities after being annealed at 1600 °C, when the  $V_C-C_{Si}$  defects (P6/P7) have already been annealed out. This indicates that the  $V_C-C_{Si}$  pairs do not play an important role in carrier compensation and are not responsible for the SI properties in HPSI 4H-SiC as it was suggested by Carlos et al in Ref. 4.22.

#### 4.2.3 Conclusions

In summary, I have observed the EPR spectra of the P6/P7 defects in irradiated 4H-SiC and determined the spin Hamiltonian parameters for the centers. The analyzed  $g$  and  $D$  tensor parameters and the number of EPR spectra corresponding to different inequivalent lattice sites in 4H-SiC support the identification of the P6/P7 centers as the  $V_C-C_{Si}$  pairs. The increase of the intensity of the P6/P7 centers in the temperature range 600-850 °C can be explained by the transformation of  $V_{Si}$  into the  $V_C-C_{Si}$  pairs. In irradiated material the P6/P7 centers are annealed out at ~1100 °C.

### 4.3 Silicon vacancy related $T_{V2a}$ center in 4H-SiC

#### 4.3.1 Introduction

In irradiated n-type 4H and 6H-SiC, several optically detected magnetic resonance (ODMR) spectra, labeled  $T_{V1x}$ ,  $T_{V2x}$ , and  $T_{V3x}$  (with  $x=a, b$ ), are often detected by monitoring a near-infrared photoluminescence (PL) band, which consists of zero-phonon lines (ZPL's) at 1.438 eV (labeled V1) and 1.352 eV (V2) in 4H-SiC and 1.433 eV (V1), 1.398 eV (V2), and 1.368 eV (V3) in 6H-SiC [4.23]. These ODMR centers have  $C_{3v}$  symmetry and an isotropic  $g$ -value close to 2.003. These spectra were also observed by electron paramagnetic resonance by several groups in 4H and 6H-SiC [4.19, 4.24-4.26]. One of these ODMR spectra,  $T_{V2a}$ , is related to the ZPL V2 at 1.352 eV in 4H-SiC [4.23]. In these works [4.19, 4.23-4.26], these spectra were suggested to originate from spin triplet states ( $S=1$ ). The spectra were first observed by Vainer and Il'in in slightly n-type 6H-SiC [4.19] (labeled P3 and P5) and were attributed to the far-distance vacancy pairs ( $V_{Si}-V_C$ ) with different zero-field splitting (ZFS) parameter  $D$  depending on the distance between the two vacancies. Based on the hyperfine structure due to the interaction with 12 Si atoms in the NNN shell, the spin state, the correspondence between the number of the ZPL's (two in 4H and three in 6H-SiC) and the number of inequivalent lattice sites in each polytype, and the possible level position in the bandgap of 6H and 4H-SiC, Sörman et al. [4.23] attributed the centers to the neutral isolated silicon vacancy ( $V_{Si}^0$ ) at the quasi-cubic and hexagonal lattice sites.

In a Zeeman study by Wagner et al. [4.27], no splitting of any ZPL's in the magnetic field up to 5 T has been detected, indicating that the corresponding PL transitions are between the singlet states. The triplet spectra seen in ODMR were therefore tentatively explained as being detected indirectly via an excited triplet state located between the ground and excited singlet states [4.27]. However, recent EPR observations of the same spectra in 4H and 6H-SiC under equilibrium conditions at low temperatures (1.2 to 4 K) [4.25, 4.26] suggesting that the spectrum must arise from the ground state.

Recently, complete ligand hyperfine tensors of the interaction with four C atoms in the NN shell have been determined [4.24, 4.28-4.30], supporting the isolated silicon vacancy model. There is an ambiguity about the spin  $S=1$  of the  $T_{V2a}$  center since its EPR spectrum always appears together with the strong signal at  $g \sim 2.003$  of the undistorted negatively charged silicon vacancy ( $V_{Si}^-$ ) [4.13, 4.31, 4.32], which may hide the central line of a possible  $S=3/2$  spin. Recently, the spin state  $S=3/2$  was indirectly determined for the  $T_{V2a}$  center in 4H-SiC by pulsed-EPR [4.28], whereas the high-field pulsed-EPR study by Orlinski et al. [4.25] suggested a spin  $S=1$  in agreement with Sörman et al. [4.23]. In a magnetic circular dichroism of the absorption (MCDA) and MCDA-detected EPR (MCDA-EPR) study of 6H- and 15R-SiC, Lingner et al. [4.33] observed the same PL band, but the MCDA-EPR spectrum measured on the V3 ZPL at 1.369 eV in 6H-SiC consists of only one line with  $g=2.005$ . This leads to a suggestion that the ground state of the silicon vacancy in SiC is triple negative ( $-3$ ) with  $S=1/2$  [4.33].

Clarifying the spin state of the  $T_{V2a}$  center is important for understanding the electronic structure of this fundamental defect.

#### 4.3.2. Experimental details

In irradiated SiC, the  $T_{V_{2a}}$  spectrum always appears together with the dominating signal of  $V_{Si}^-$ , which has almost the same  $g$ -value and similar HF structures. This makes the direct determination of the spin of the  $T_{V_{2a}}$  center difficult. In order to avoid the interference of the  $V_{Si}^-$  signal, in this study I used as-grown semi-insulating (SI) 4H-SiC substrates grown by HTCVD [4.34]. The typical concentration of some common residual impurities in HTCVD wafers measured by secondary ion mass spectrometry (SIMS) is: N(nitrogen)  $\sim 7.6 \times 10^{15} \text{ cm}^{-3}$ , N(boron)  $\sim 1.2 \times 10^{15} \text{ cm}^{-3}$ , N(aluminum)  $\sim 6.6 \times 10^{13} \text{ cm}^{-3}$ , and N(vanadium)  $\sim 8.0 \times 10^{12} \text{ cm}^{-3}$  [4.34]. In this material, intrinsic defects are used to compensate nitrogen donors to obtain SI properties. The resistivity of the SI material at room temperature is in the range  $\rho > 10^9 \Omega \text{ cm}$ . EPR measurements were performed on a Bruker X-band ( $\sim 9.47 \text{ GHz}$ ) EPR spectrometer. In photo-EPR measurements, a xenon lamp with a power of 150 W was used as the excitation source. Appropriate long-wavelength-passed and short-wavelength-passed optical filters were used to form band-passed filters at different wavelengths.

#### 4.3.3 Results and discussion

The sample was mounted and cooled down to 77 K in dark to obtain equilibrium conditions. Fig. 4.10a shows the EPR spectrum measured in dark at 77 K for the magnetic field  $\mathbf{B}$  along the  $c$ -axis. As indicated in Fig. 4.10a, the EPR signals of the positively charged carbon vacancy ( $V_C^+$ ) [4.1] and a new center, labeled SI-9, are predominant. Another lines, labeled SI-4 [4.35], also appear in this region of  $g=2$  (Fig. 4.10). We will not discuss here further on the SI-4 and SI-9 centers. In addition to these signals, two weak lines at  $\sim 335.42 \text{ mT}$  and  $\sim 340.40 \text{ mT}$  were detected (Fig. 4.10a). Under illumination by light with photon energies  $h\nu \geq 1.4 \text{ eV}$  ( $\lambda \leq 890 \text{ nm}$ ), the intensity of these two lines increase by two orders of magnitude. Figs. 4.10b and 4.10c show the spectra measured for  $\mathbf{B}$  parallel and perpendicular to the  $c$ -axis, respectively, with a dramatic enhancement in intensity of these two lines under light illumination with  $\lambda \geq 630 \text{ nm}$  ( $h\nu \leq 1.97 \text{ eV}$ ). (Light with this wavelength was used to suppress the ( $V_C^+$ ) [4.3] and SI-4 signals.) The angular dependence study show that these two lines belong to a spin  $S=1$  center with an isotropic  $g$ -value  $g=2.0028 \pm 0.0001$  and a ZFS parameter  $D = 46.75 \times 10^{-4} \text{ cm}^{-1}$  (or  $70.1 \pm 0.2 \text{ MHz}$ ). Within the experimental error, both  $g$  and  $D$  values of this center are identical to that of the  $T_{V_{2a}}$  center measured by Mizuochi et al. [4.28].

In this as-grown high-purity material, the line width (the distance between the maximum and minimum of the first derivative EPR line) is only  $\sim 0.039 \text{ mT}$  and a well-resolved isotropic HF structure is observed (Fig. 4.10b). The splitting between the lines b is  $0.305 \text{ mT}$ , which is a half of the splitting between the lines c ( $0.61 \text{ mT}$ ). The intensity ratios between the HF lines and the main line are  $b/a=0.25$  and  $c/a=0.03$  if comparing the amplitude ( $b/a=0.26$  and  $c/a=0.034$  if comparing the integrated intensity). This HF structure is clearly the same structure due to the HF interaction with one and two  $^{29}\text{Si}$  atoms (nuclear spin  $I=1/2$  and a natural abundance of 4.67 %) among 12 NNN Si atoms as observed for the  $T_{V_{2a}}$  center in Ref. 4.23 and 4.28. The observed intensity ratios are in good agreement with the calculated ones:

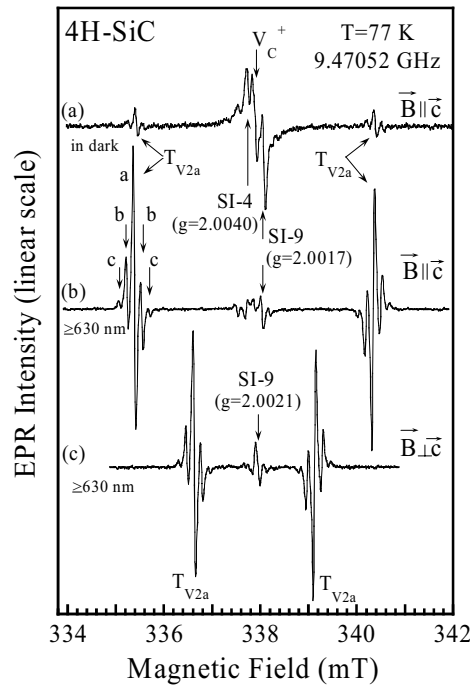


**Figure 4.10** EPR spectra in SI 4H-SiC grown by HTCVD measured for the magnetic field  $\vec{B}$  along the  $c$ -axis and at 77 K (a) in dark and (b) and (c) under illumination with light of wavelength  $\lambda \geq 630$  nm.

$b/a=0.273$  and  $c/a=0.037$ . From the same  $g$  and  $D$  values and the NNN  $^{29}\text{Si}$  HF structure (within experimental errors), it is evident that I have observed the  $T_{V2a}$  center. As can be seen in Figs. 4.10b and 4.10c, it is clear that the  $T_{V2a}$  spectrum consists of only two strong lines under light illumination.

The  $T_{V2a}$  and  $T_{V3a}$  spectra in 6H-SiC with clearly only two lines each have previously been observed in ODMR using resonant excitation at the corresponding ZPL's V2 and V3 [4.23]. From the observations by ODMR [4.23] and EPR in this work, it seems that the  $T_{V2a}$  spectrum with two lines arises from a spin triplet state ( $S=1$ ).

Both the low- and high-field lines of the  $T_{V2a}$  spectrum have the same phase corresponding to the absorption of microwave (MW) when measuring in dark (Fig. 4.10a), but have opposite phases under light illumination (Figs. 4.10b and 4.10c). This can be explained by the energy-level scheme illustrated in Fig. 4.11. Since the spectrum can be observed in dark and at low temperatures (even at 1.2 – 4 K [4.25, 4.26]) the triplet state must be the ground state. Under equilibrium conditions, all the states  $|S, M_S\rangle$  of the triplet (the singlet  $|1,0\rangle$  and doublets  $|1,-1\rangle$  and  $|1,+1\rangle$ ) are populated and the MW absorption occurs in both transitions  $|1,0\rangle \leftrightarrow |1,+1\rangle$  and  $|1,-1\rangle \leftrightarrow |1,0\rangle$ . In low-frequency (X-band) EPR experiments, the splitting of these sublevels under the magnetic field is very small. At elevated temperatures, e.g. at 77 K as in our case, the difference in the population at these levels should be also small. Therefore, the EPR signal measured in dark is rather weak (Fig. 4.10a). Under illumination by light with the photon energies of  $\sim 1.352$  eV (the energy of the ZPL V2 in 4H-SiC) or higher, electrons from the sublevels of the triplet ground state are pumped to the excited state of the center. The excited electrons rapidly relax down to the singlet ( $S=0$ ) excited state and then radiatively recombine to the singlet  $|1,0\rangle$  level in the ground state, giving rise to the ZPL observed in PL. Only this singlet-singlet optical transition

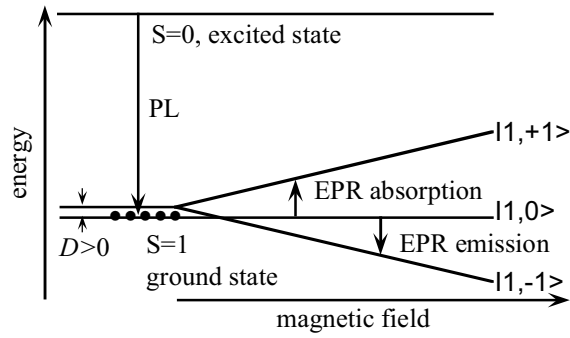


**Figure 4.11** The energy-level scheme for the  $T_{V2a}$  center in 4H-SiC. Under illumination by light with the photon energy  $h\nu \geq 1.4$  eV, only the singlet  $|1,0\rangle$  state is populated while the  $|1,+1\rangle$  and  $|1,-1\rangle$  states are empty since only the optical transition from the singlet ( $S=0$ ) excited state to the singlet sublevel  $|1,0\rangle$  of the triplet ground state is allowed, giving rise to the ZPL (at 1.352 eV for the  $V2$  ZPL) in PL. The low- and high-field EPR lines correspond to the MW absorption and emission, respectively.

is allowed while the optical transitions from the singlet excited state to the  $|1,+1\rangle$  and  $|1,-1\rangle$  sublevels of the ground states are forbidden. As a result, under light illumination only the singlet ground state  $|1,0\rangle$  is populated whereas the  $|1,+1\rangle$  and  $|1,-1\rangle$  states become empty (Fig. 4.11). Under this condition, the MW absorption transition  $|1,0\rangle \rightarrow |1,+1\rangle$  and the MW emission transition  $|1,0\rangle \rightarrow |1,-1\rangle$  will occur, giving rise to the EPR absorption and emission lines. Therefore, two EPR lines always have opposite phases. Since only the singlet state is populated under illumination, differences in population at sublevels of the triplet state become much larger compared to the case of equilibrium condition (in dark). This explains the dramatic increase of the EPR signal (approximately two orders of magnitude) under illumination.

As can be seen in Fig. 4.10, the EPR absorption gives rise to the low-field line. Therefore, the ZFS parameter  $D$  must be positive in this case. Since the transitions from the singlet ( $S=0$ ) excited state to the  $|1,+1\rangle$  and  $|1,-1\rangle$  sublevels of the triplet ground state are forbidden, only one ZPL line corresponding to the singlet-singlet transition can be detected. This explains why no splitting of the ZPL under the magnetic field could be observed in Zeeman experiments [4.27]. It should be noticed this model with the triplet ground state and a singlet excited state is the only alternative which could explain both the observed EPR line structure of the center and the Zeeman results.

Note that in the case of spin  $S=3/2$  ground state as suggested in Ref. 4.28, the EPR spectra in Fig. 4.10 can also be explained by a model similar to that in Fig. 4.11. For the case  $S=3/2$  ground state, considering an  $S=1/2$  excited state, three weak EPR lines are expected to be detected in dark. Under illumination by light, electrons from the ground state are pumped to the excited state and then radiatively recombine to the ground state. Only optical transitions from the  $|1/2, \pm 1/2\rangle$  levels of the excited state to the  $|3/2, \pm 1/2\rangle$  sublevels of the ground state are allowed. In this case an enhanced population difference will appear between the  $|3/2, -3/2\rangle$  and  $|3/2, -1/2\rangle$  sublevels and between the  $|3/2, +1/2\rangle$  and  $|3/2, +3/2\rangle$  sublevels of the ground state, giving rise to an emission-like  $|3/2, -1/2\rangle \rightarrow |3/2, -3/2\rangle$  and an absorption-like  $|3/2, +1/2\rangle \rightarrow |3/2, +3/2\rangle$  transition with increased EPR intensity. Since both the  $|3/2, \pm 1/2\rangle$  sublevels of the ground state are pumped from the excited state, there will no be increase in

their population difference and, consequently, the intensity of the central EPR line corresponding to the transition  $|3/2, -1/2\rangle \rightarrow |3/2, +1/2\rangle$  will not be increased. Therefore, two strong lines emerge in the EPR spectrum under light illumination, like in Fig. 4.10. Accordingly, the EPR results alone cannot decide if the spin of the ground state is  $S=1$ , or  $S=3/2$ . But, for  $S=3/2$  there will be more than one optical transition from the excited state to the ground state detected in PL and hence the splitting of the ZPL under magnetic field would be observable. This condition excludes the possibility of  $S = 3/2$ .

The explanation for the nonsplitting of the ZPL using an additional nonradiative level in between the excited and ground states, and assuming the same splitting in the triplet excited state and triplet ground state in Ref. 4.25, is also not satisfactory. It is possible in principle but difficult to have such coincidences of the energy levels in different SiC polytypes. Even for the cases of both the excited and ground triplet states having the same splitting, all the sublevels on the ground state will be populated under light illumination since more than one optical transition from the triplet excited state are allowed. This would lead to no difference in the intensity of the  $T_{V2a}$  signal when measuring in dark or under light illumination, which is in disagreement with the observation in Ref. 4.28 and in our work (the intensity of  $T_{V2a}$  signal increases by about two orders of magnitude under light illumination).

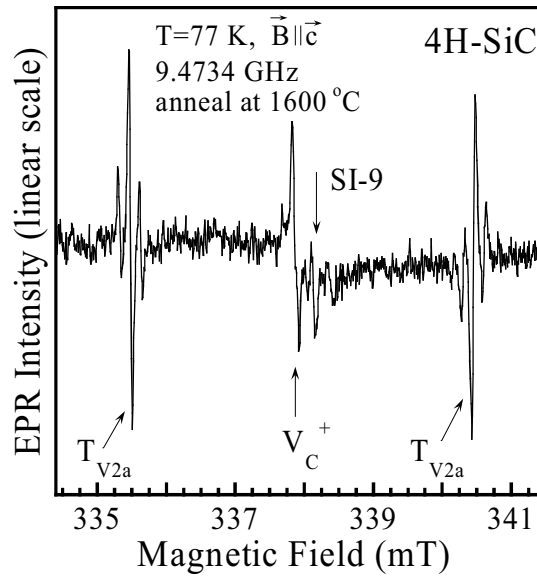


**Figure 4.12** EPR spectrum in a SI 4H-SiC sample annealed at 1600 °C for 30 minutes measured for the magnetic field  $\mathbf{B}$  along the  $c$ -axis under white light illumination.

I observed the  $T_{V2a}$  spectrum in all the studied samples (from few tens of different low doped n-type or SI wafers grown by HTCVD), but could not detect the undistorted ( $T_d$  symmetry,  $S=3/2$ )  $V_{Si}^-$  signal [4.28, 4.31] in any sample even of n-type conductivity. It was found that the  $T_{V2a}$  signal is often much weaker in slightly n-type samples than that in SI wafers. The failure in detection of the  $V_{Si}^-$  signal can not be due to the measuring conditions since this center can easily be observed either in dark or under light illumination. As also shown in Ref. 4.28, the illumination with a very powerful laser (up to 10 W) increases the  $T_{V2a}$  signal (up to the intensity level of  $V_{Si}^-$  line) but does not reduce the  $V_{Si}^-$  signal. The

absence of the undistorted ( $T_d$  symmetry,  $S=3/2$ )  $V_{Si}^-$  signal in our case also suggests that  $T_{V2a}$  is not the  $V_{Si}^-$  center with the spin  $S=3/2$  and  $C_{3v}$  symmetry as suggested in Ref. 4.28.

Fig. 4.12 shows the EPR spectrum in a SI 4H-SiC sample annealed at 1600 °C for 30 minutes in Ar gas. The spectrum was recorded for  $B$  along the c-axis and under white light illumination. The  $T_{V2a}$  signal reduces significantly but can be seen with its clear HF structure. In addition to  $T_{V2a}$ , the signals of  $V_C^+$  and SI-9 centers were also detected. The annealing was performed in a CVD system so the sample was slowly cooled down from 1600 °C. The observation of the  $T_{V2a}$  center after annealing at such high temperatures is unexpected since it is known from previous studies that the center is annealed out at around 750 °C (See in section 4.2 and also in Ref. 4.23) and has a similar annealing behavior as the  $V_{Si}^-$  signal [4.13].

From this annealing behavior and the fact that the  $V_{Si}^-$  signal has not been detected in any as-grown sample, it cannot be ruled out that the  $T_{V2a}$  center is not related to the isolated silicon vacancy as generally believed. The recent observation of the ligand HF structure due to the interaction with four nearest C neighbors [4.24, 4.28-4.30] is a strong support for the isolated  $V_{Si}$  model, but still cannot rule out the possibility of long-distance pairs along the c-axis, which are possible in hexagonal SiC polytypes.

A more probable explanation may be that the annealing in as-grown SI-SiC material may occur in a different manner than in irradiated SiC. In unirradiated SI-SiC samples  $V_{Si}$  first can transform to the  $V_C$ - $C_{Si}$  pairs by trapping a nearest neighbor C atom and then can be released from the pairs at higher temperatures when the complexes are disassociated. On the other hand, in electron-irradiated p-type substrates (see section 4.2), intrinsic defects, like carbon vacancies and interstitials and impurities (Al and also N) are present with rather high concentrations. Being transformed back from the  $V_C$ - $C_{Si}$  pairs,  $V_{Si}$  may interact with other defects and impurities available to form complexes. That may explain why the recovery of the  $V_{Si}$  signal was not detected in the irradiated samples when the  $V_C$ - $C_{Si}$  pairs annealed out.

#### 4.3.4 Conclusions

In summary, I have observed the EPR spectrum of the  $T_{V2a}$  center in as-grown SI 4H-SiC grown by HTCVD in the absence of the undistorted  $V_{Si}^-$  signal. The spectrum with only two EPR lines, together with the Zeeman results showing the nonsplitting of the zero phonon line of  $T_{V2a}$ , confirms the spin  $S=1$  of the center. The  $T_{V2a}$  spectrum arises from a spin triplet ground state and its associated PL line can corresponds to the radiative transition from a singlet excited state to the singlet sublevel of the triplet ground state. In as-grown SI material the  $T_{V2a}$  signal reduces significantly but can still be detected after annealing at 1600 °C.

Note that the  $T_{V2a}$  center is present in all as-grown SI material grown by HTCVD with the concentration comparable to that of shallow dopants (N and B) and may play an important role in carrier compensation processes.

## Chapter 5

### Ion implantation

Ion implantation is the key technique for the selective doping of SiC being unavoidable in the fabrication of microelectronics structures.

In this chapter the physical concept of ion implantation is discussed. Firstly the energy transfer between the nuclei of the implanted projectiles and the target atoms is described and the topological features of the damaged zones left behind after implantation are summarized. Section 5.2 deals with the channeling phenomenon that governs the movement of projectiles along low index crystallographic directions in single crystals. The influence of crystal defects on the channeling process is described in section 5.3. Finally, section 5.4 gives a brief summary of electronic stopping processes both in elemental targets and multi-elemental compounds.

The major part of my work on implantation into SiC was performed with 500 keV N<sup>+</sup> ions. Accordingly, this energy will be used in the following mathematical expressions to show the representative features of ion implantation.

#### 5.1 Nuclear energy loss and defect formation

For ion implantation in the commonly applied energy range non-relativistic approximation of the movement of projectiles can be applied. For example the velocity of a N ion with energy of 500 keV is:  $v = 2.6 \times 10^6 \text{ m s}^{-1} \ll c$ . The formula in Equation 2.5 for the energy transmitted to a PKA in an elastic nuclear collision in the laboratory frame of reference is modified to the expression [5.1]:

$$T = 4E \frac{mM}{(m+M)^2} \cos^2 \varphi \quad (5.1)$$

Here the notations are consistent with Equation 2.5. For a N ion with 500 keV energy a head-on collision with a target Si or C atom gives  $T = 444 \text{ keV}$  and  $497 \text{ keV}$ , respectively. These energies are much higher of 4 orders of magnitude than the displacement thresholds. Considering unscreened Rutherford scattering for nuclear collisions, the cross-section for scattering at a greater angle than a chosen minimum  $\theta_{min}$  in laboratory system is [5.2]:

$$\sigma = \pi P^2 = \pi \left( \frac{Z_1 Z_2 k e^2}{2E} \right)^2 \left( \frac{1 + \cos \Theta_{min}}{1 - \cos \Theta_{min}} \right) \quad (5.2)$$

Here  $Z_1$  and  $Z_2$  are the atomic numbers of the projectile and the recoil,  $k$  is the Coulomb constant,  $P$  is the impact parameter (see Fig. 2.5), and  $e$  is the charge of electron, respectively. Note that  $\theta_{min}$  corresponds to a maximum impact parameter  $P_{max}$  considering the fact that the target is in the form of a close-packed crystal with atomic density of  $N_{SiC}$  and therefore  $P$  cannot be chosen to be arbitrarily big.

For 500 keV N ions in SiC  $\theta_{min}$  is less than  $0.01^\circ$ . Deflections to large scattering angles can be expected for  $P \ll P_{max}$  when the projectile is involved in a close encounter event with the target nucleus. These small impact parameters are the order of  $10^{-14} \text{ m}$ , which is



comparable to the nuclear radius and much smaller than the Bohr radius. Accordingly, the cross-section of these processes is not affected by the screening of electron shells. Nevertheless, for impact parameters comparable to the Bohr radius, the screening from electrons has to be considered. Therefore generally a screened Coulomb potential and the corresponding screened nuclear cross-section is used to model elastic collision processes to satisfy the requirement both for small and large impact parameters. For that purpose, the so-called ‘universal’ interatomic potential has been introduced [5.3]:

$$V(r) = \frac{Z_1 Z_2 e^2}{r} \Phi\left(\frac{r}{a}\right) \quad \text{where} \quad \Phi(x) = \sum_{i=1}^n A_i \exp(-B_i x) \quad (5.3)$$

Here  $a$  is the ‘universal’ screening length  $a = 0.885 a_0 (Z_1^{0.23} + Z_2^{0.23})^{-1}$ , and  $a_0$  is the Bohr radius. The parameters  $A_i, B_i$  can be optimized for a wide energy range and a large number of different projectile-target systems.

In a close encounter the energy 10-100 keV deposited into the nuclear subsystem of the target leads to the formation of atomic collision cascades started by the PKAs. As it has been calculated, the energy deposition of the sub-cascades takes place at the position where the collision between the ion and the PKA occurs [5.4]. In accordance, cascades are usually dense and their extent is small compared to the penetration depth of the ions. Cascade processes come to rest leaving behind a large number of displaced host atoms. For instance when 500 keV N ions are implanted into SiC, more than  $10^2$  Si or C displacements per implanted atom (dpa) are created. For the average mean free path between elastic nuclear collisions during random scattering Equation 2.6 gives  $\lambda = 0.3 \mu\text{m}$  being an order of magnitude smaller than that derived for 2.5 MeV electrons. Moreover, for 500 keV N ions the electronic stopping power  $S_e$  is about  $1 \text{ keV nm}^{-1}$  at the target surface. High  $S_e$  leads to shallow ion penetration  $< 1 \mu\text{m}$ . Accordingly, for ion implantation with similar parameters (energy, fluence, and fluence rate), the amount of defects is about hundred times higher and the damaged zone extends over a thousand times thinner layer, as compared to electron irradiation.

In contrast to the case of electrons the mean topological features of damaged zones caused by ions are the high density of displacements within one cascade and the geometrical overlap of individual cascades induced at the same target position by consecutive ion impacts when irradiating to high fluences. This topology gives high probability of both intra-cascade interactions between primary defects, and interactions between already relaxed damaged areas and unrelaxed “hot” cascades. Note that inter-cascade interactions between “hot” cascades are not likely since the time between consecutive ion impacts creating displacements in the same target region at commonly used low fluence rates of  $\Phi = \sim 10^{12} \text{ ions cm}^{-2} \text{ s}^{-1}$  is the order  $\sim 100$  sec [5.5] while characteristic cascade relaxation times are  $\sim 10^{-12}$  sec [5.6]. Nevertheless, both recombination and clustering of defects should take place and larger defect complexes can be formed leading to the accumulation of local strain and the structural relaxation of the surrounding atomic configuration. Moreover, when creating atomic displacements in an already imperfect crystal, the threshold energy of atomic displacements  $E_d$ , determined from electron-irradiation experiments, is no longer valid.  $E_d$  in damaged crystals depends on several parameters and is expected to be lower than in undamaged crystals.

Due to these circumstances, either the multiplication of the number of atomic displacements or the suppression of primary defects generated in atomic collision cascades

can occur making the description of damage build-up processes a complicated task. Contrary to linear defect accumulation during low-fluence electron irradiation, for ion implantation the amount of damage vs. fluence usually shows non-linear dependence. Both sublinear and superlinear dependence can be found. Anyway, in SiC, at sufficiently low temperatures, the gradual increase of fluence finally leads to complete amorphization when the crystal lattice is totally disordered. SiC can be amorphized at room temperature by ion-irradiation and the amorphous phase is expanded in volume by  $\sim 11\%$  as confirmed by X-ray photoelectron spectroscopy (XPS) and electron energy loss spectroscopy (EELS) measurements [5.7]. To explain the qualitative features of defect accumulation, semi-empirical models of the underlying physical processes are often proposed. Usually the shape of the damage vs. fluence curve alone provides enough information to decide the rightness of a certain model assumption [5.8]. These models then contain a number of free parameters to fit the experimental results quantitatively.

In Appendix 2 phenomenological models and mechanisms for the irradiation-induced crystalline-to-amorphous transformation in ceramics are briefly reviewed, and the specific model for the direct-impact, defect-stimulated (D-I/D-S) amorphization, taking place during ion implantation into SiC, is discussed.

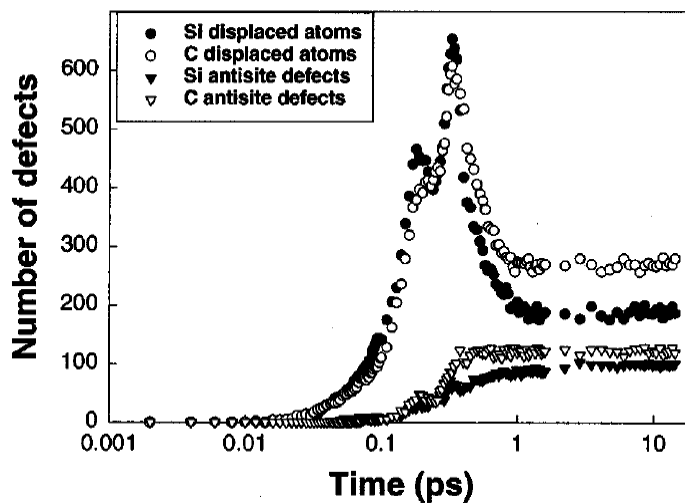


**Figure 5.1** *The number of vacancies and antisites as a function of time in collision cascades induced by 550 keV Si ions in SiC taken from Ref. [5.6].*

In the implantation process, the initial stage of displacement cascades relaxes into a stable or metastable defect configuration. Since for SiC the length scales of cascade processes are of the order of 10 nm, and the time scales of cascade relaxation are of the order of 1 ps [5.6] (see Fig. 5.1), such processes are experimentally inaccessible. Only the end stage can be experimentally observed. To shed light on the problem besides the semi-empirical description one possibility is to perform molecular dynamics (MD) simulations of in-situ cascade relaxation processes and of the residual defect structure. Some detailed MD studies have been performed to follow damage accumulation in SiC in the function of implantation fluence and an overall picture have been suggested for the processes taking place during irradiation [5.9]. However, a systematic experimental observation of this scenario, following the end damage stages in the function of fluence has not yet been reported. Only mosaics of the overall picture have been studied. In section 7.3 a detailed experimental study of damage accumulation during ion implantation into 6H-SiC is presented.

## 5.2 Channeling in the crystal

Now let us take into account the ordered crystalline structure of the target that can give rise to the so-called channeling phenomenon when ions travel in solids. Fig. 5.2 shows schematic picture of a single crystal with atomic rows lying parallel in the paper plane. If a uniform flux distribution of energetic ions enters into the crystal parallel to the atomic strings, basically two different cases can be considered:

- (a) A low fraction of projectiles is involved immediately in close encounter events with the atoms of one of the uppermost monolayers. They can totally backscatter or start random scattering in the crystal. The net of the particles propagating randomly in the sample is often called as the random fraction  $\chi_R$  of the beam.
- (b) For the rest of projectiles a correlated sequence of scatterings can continue for hundreds of atoms, until an incident particle is slightly steered away from the closest row of atoms. Interaction with an adjacent row is similar, so that the motion is oscillatory, bouncing from row to row with a wavelength hundreds of angstroms long. An important feature of this motion is that particles cannot get close enough to the atoms of the solid to undergo close-encounter events. The phenomenon is called channeling and particles type (b) represent the channeled fraction of the beam (i.e.  $1-\chi_R$ ).

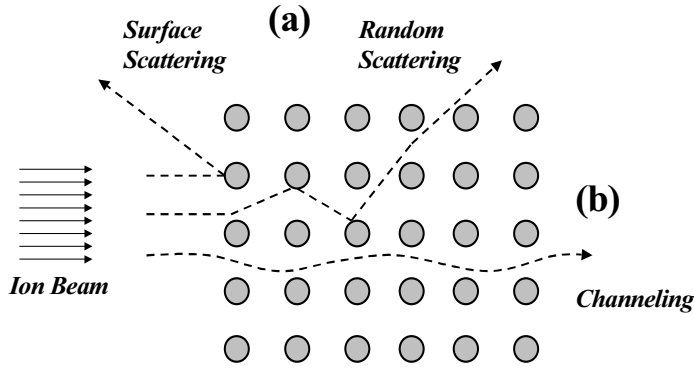


**Figure 5.2**  
Schematic picture of  
(a) surface scattering,  
random scattering and  
(b) channeling  
trajectories in a crystal.

Channeling should occur in both one and two dimension. In 1D the oscillatory motion of the projectile is confined by parallel atomic strings whereas in 2D by parallel planes of atoms. Channeling in one dimension is called axial channeling while two-dimensional channeling is referred to as planar channeling. In the following we will focus on the details of axial channeling, however, the description for planar channeling is quite similar.

Channeling can be described in a continuum description of the atomic rows or planes, that is, by considering the rows or planes of atoms as continuous strings or sheets of charge [5.10]. Nevertheless, if particles penetrate close to an atomic row they sense the roughness of the string potential because of the discrete nature of the atomic row and the thermal vibrations. This suggests a minimum distance of approach to the string  $P_{min}$ , for which the continuum model and the channeling concept are valid. There is a corresponding maximum incident angle, called critical angle,  $\Psi_{crit}$ , for which the incident particles can be steered by the atomic rows. Experimentally the critical angle is determined by measuring the close-encounter probability from just beneath the surface as a function of angle between the beam and the symmetry direction of the crystal. This process is called angular scan. The angular width at the half maximum, the half angle  $\Psi_{1/2}$ , (Fig 5.3) is taken as a measure of the critical

angle.  $\Psi_{1/2}$  can also be estimated starting from theoretical considerations. Some of the most precise critical angle formulas have been derived by Barrett [5.11] from numerical simulations of the channeling process. The functional dependence of  $\Psi_{1/2}$  in this manner is:

$$\Psi_{1/2} = kR \left( \frac{m\langle u \rangle}{a_{TF}} \right) \Psi_1, \text{ where } \Psi_1 = \sqrt{\frac{Z_1 \bar{Z}_2 e^2}{Ed}} \quad (5.4)$$

Here  $\bar{Z}_2$  is the average atomic number of the host atoms of the crystal and  $d$  is the mean interatomic spacing in the target, along the channeling axis, respectively. In general  $\Psi_1$ , that should be considered as the most straightforward estimation of  $\Psi_{crit}$ , already predicts the correct  $Z_1$ ,  $\bar{Z}_2$ ,  $d$  and  $E$  dependence. In Equation 5.4,  $R(\xi) = [f_{rs}(\xi)]^{1/2}$  is the square root of the Molière string potential that has been tabulated by Barrett. The quantities  $k$  and  $m$  are free parameters, and from a number of experimental data have been optimized for axial channeling as  $k = 0.83$ , and  $m = 1.2$ , [5.11].  $a_{TF}$  is the Thomas-Fermi screening radius  $a_{TF} = 0.885a_0(Z_1^{1/2} + Z_2^{1/2})^{-2/3}$ , and  $\langle u \rangle$  is the root-mean-square (r.m.s.) displacement of host atoms with respect to their equilibrium lattice sites, respectively. The value of  $\langle u \rangle$  in perfect, undamaged crystals can be considered as the r.m.s. thermal vibrational amplitude, whereas in damaged crystals  $\langle u \rangle$  increases (interstitial atoms displaced more than thermal vibrations) and therefore  $\Psi_{1/2}$  decreases.

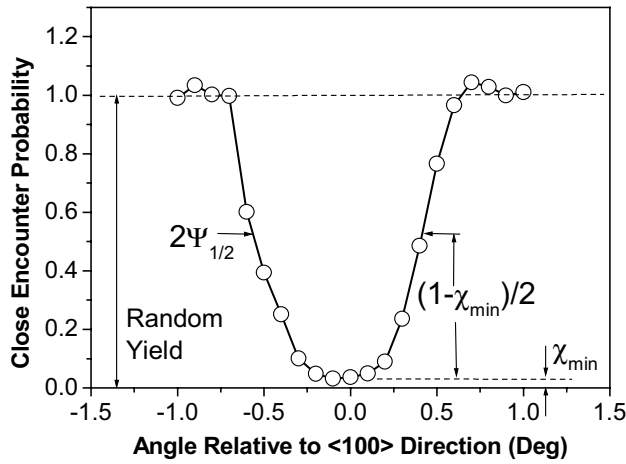


**Figure 5.3** Close-encounter probability as a function of the angle between the beam and the symmetry direction of the crystal. The actual data points are for the case of 1.5 MeV He particles incident on Si <100> at 300 K (measurement of the author).

In addition to  $\Psi_{1/2}$  there is another parameter describing the angular scan curve. In Fig. 5.3 the minimum in the close-encounter probability is referred to as the minimum yield,  $\chi_{min}$ . The minimum yield represents the fraction of backscattered particles that is in Fig. 5.2 corresponds to trajectories of type (a). In general a small fraction of  $\chi_{min} \approx 1-5\%$  of the projectiles give the minimum yield.

Even in a perfect crystal, channeled particles can be scattered into nonchanneled trajectories as they penetrate the material. This process is referred to as dechanneling. In the perfect crystal the channeled particles undergo many small angle scattering events with electrons. The angle with which these particles cross the center of the channel slowly increases because of this multiple scattering (MS), and thus an increasing number of particles come closer to the rows and planes. Such particles can then collide with lattice atoms

displaced out from their static rest positions because of thermal vibrations. In these close-encounter collisions some of the particles are scattered through angles too great ( $\Psi > \Psi_{crit}$ ) to allow particles to maintain their channeled trajectories. The combination of multiple scattering by electrons and scattering by thermally displaced atoms at the channel walls leads to an increase with depth of the dechanneled fraction  $\chi_R$  of the particles. While scattering by electrons will always be present, the scattering by thermal displacements is strongly dependent on the vibrational amplitude of the atoms and, consequently, can be minimized by reducing the temperature.

The amount of dechanneling also depends on the crystallographic orientation and is minimized by channeling along low-index crystallographic axes. However, if the crystal is oriented such a way that the angle between the direction of the crystallographic axis and of the impinging particles is sufficiently larger than  $\Psi_{crit}$ , the channeled particle fraction  $1 - \chi_R$  is minimized. In such case the close encounter probability is chosen to be 1 (Fig. 5.3), and the orientation is called “random”.

The measure of angular scan allows the orientation of the target along low index crystallographic directions with respect to the ion beam. In this case the sample can be fixed on a two-axis goniometer system and its tilt and angular coordinates are varied in small steps until the backscattering yield is minimized. This procedure is applied in ion beam analysis techniques in the adjustment of backscattering/channeling experiments, see in section 6.2.5.

### 5.3 Dechanneling by defects

The presence of defects can greatly enhance dechanneling over that found in the perfect crystals. Each type of defect has a particular influence on the trajectory of a travelling particle and can be associated with a corresponding dechanneling factor  $\sigma_D$ . In this section we consider two classes of defects leading to enhanced dechanneling in the crystal. First, displaced atoms in the center of the channel provide much stronger scattering than the electrons in multiple scattering events. These atoms, for sufficiently close encounters, can directly scatter particles beyond the critical angle by one single collision (see Fig. 5.4a). Second, extended defects can cause distortions or curvature of the channeled wall; this gives greater dechanneling than that due to the wall roughening caused by thermal vibrations. Thermal vibrations are the order of  $\sim 0.1$  Å. Defect-induced distortions may be comparable to thermal displacements over a single atomic spacing, but the cumulative effect of the distortions is larger when viewed over the many tens of atom spacings. Dechanneling occurs when the resulting distortions of the channels become significant relative to the channeling critical angle  $\Psi_{crit}$  (see Fig. 5.4b). Generally, the probability of dechanneling per unit depth  $dP_D/dx$  is given by the product of the defect dechanneling factor and defect density  $c_D$  [5.12]:

$$\frac{dP_D}{dx} = \sigma_D c_D(x) \quad (5.5)$$

The units of  $\sigma_D$  and  $c_D$  depend on the kind of defect giving rise to scattering so that the probability of dechanneling per unit depth  $dP_D/dx$  has units of  $\text{cm}^{-1}$ .

For point-scattering centers, e.g. for interstitial atoms,  $\sigma_D$  can be thought of as a cross-section for dechanneling and  $c_D$  is given by the density of interstitial atoms per unit volume at a given depth  $x$ . The quantity  $\sigma_D$  for isolated atoms in a channel is the cross-section for the

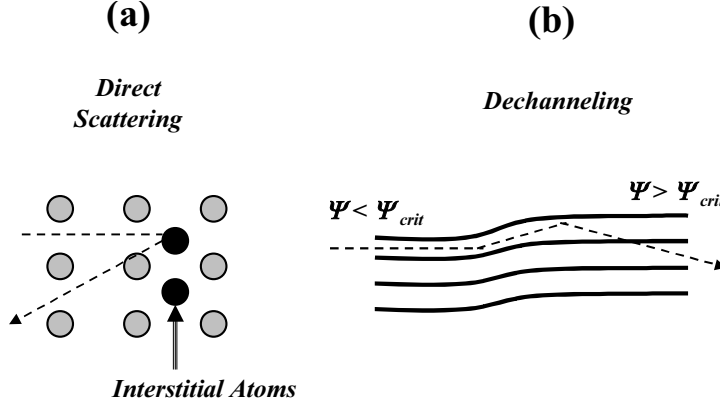


**Figure 5.4** Dechanneling of initially channeled incident particles in a crystal (a) by interstitial atoms and (b) by extended defects making a long-range curvature of the lattice.

close-impact collision probability of scattering a particle through an angle  $\theta$  greater than the critical angle. For this purpose the unscreened Rutherford total cross-section from Equation 5.2 can be used, however, with replacing the minimum angle  $\theta_{min}$  by  $\theta_{crit}$ .

In real crystals the relaxed equilibrium position of isolated self-interstitials is not well known at high defect concentrations ( $\geq 1\%$ ) typically required for channeling effect studies of defects. In practice a random distribution of atom position within the channel is assumed. In this case a detailed knowledge of the flux distribution of the channeled particles within the channel is not required, and only the fraction of the particles that remain channeled is utilized. Consequently, one obtains a unique dechanneling factor for point defects in this *random position* approximation.

In general, for low defect concentrations, the contribution of point scattering centers to dechanneling can be easily calculated in the function of depth. However, this single scattering phenomenon holds just for  $< \sim 10^{17} \text{ cm}^{-2}$  total areal density of isolated atoms traversed by the beam [5.12]. Above this threshold, multiple scattering events for nuclear scattering must also be taken into account similarly to that for multiple scattering by electrons. Multiple scattering plays especially significant role when larger amorphous clusters are embedded in a single-crystalline matrix or in polycrystalline layers if the crystallites are small and randomly oriented with respect to the single-crystalline substrate.

In case of totally amorphous layers the amount of dechanneling can be obtained using the MS theory. The mean number  $m$  of collisions of the particles with host atoms in an amorphous layer of thickness  $t$  and atomic density  $c$  can be expressed as [5.12]:

$$m = \pi a_{TF}^2 c t \quad (5.6)$$

For values of  $m > 0.2$  the MS theory has to be applied. For example, in SiC for a uniform defect density of  $\sim 1\%$ , the single scattering approximation applies to a maximum thickness of 200 nm. This is commonly the order of the penetration depth of implanted ions, so it is necessary to consider multiple scattering events in the evaluation of ion-channeling measurements to extract the depth distribution of implantation-induced damage. However, the discussion of the MS theory is beyond the scope of this thesis. Further details can be found in works reported by Meyer [5.13], and Sigmund and Winterborn [5.14].

Now let us concentrate on extended defects. For linear and two-dimensional defects,  $c_D$  has the dimensions of  $\text{cm}^{-2}$  and  $\text{cm}^{-1}$  thus giving the total length and the total area of

defects per unit volume. The dimensions of the corresponding dechanneling factors  $\sigma_D$  are cm and cm<sup>0</sup> (dimensionless), respectively. Such defects can be dislocations, stacking faults, or, for example, strained crystalline rows or planes at the borders of crystalline/amorphous interfaces. Since such kinds of defects consist only of small distortions from the ideal lattice, the presence of the defects can be detected through the dechanneling process rather than by direct scattering from the defect itself. It is reflected in the gradual increase of the random fraction  $\chi_R$  of the projectiles with depth.

## 5.4 Electronic Energy Loss

Let us discuss another process causing energy dissipation to particles penetrating material: the electronic energy loss.

The energy lost by inelastic collisions of the projectiles with the electron shells of target nuclei can be described in terms of the electronic stopping power,  $S_e$ , that is defined as the energy loss per unit length,  $dE/dx$ . Sometimes the energy loss is expressed in terms of the so-called stopping cross-section  $\varepsilon = 1/N(dE/dx)$ .

The electronic stopping depends on the ion velocity  $v$  and generally three different regions can be distinguished. (1) The first is the low ion velocity range from  $v \approx 0.1v_0$  to  $Z_I^{2/3}v_0$ , where  $v_0$  is the Bohr velocity. In this range  $S_e$  is roughly proportional to the ion's velocity. (2) The second range is of very high velocities when  $v \gg v_0$ , where the ion is fully stripped of its electrons and the energy loss is proportional to  $Z_I^2$ , as expressed by the Bethe-Bloch formula [5.12]. The energy loss then decreases with increasing velocity, which can be understood by considering that here the interaction time is the key parameter, which certainly decreases with velocity. (3) The third region is the intermediate region between (1) and (2) where the ion is only partly ionized and  $S_e$  is maximal. Charge exchange processes play an important role in this range. Here, in order to model the stopping power, a so-called effective charge is introduced.

Based on a large set of experimental data and theoretical calculations to date the electronic energy loss for all kinds of projectiles in many elemental targets have been derived. Ziegler and his co-workers have given an empirical parametrisation method for the estimation of stopping powers in amorphous (i.e. isotropic) materials [5.15]. These stopping powers could be referred to as ZBL stopping powers ( $S_e^{ZBL}$ ). The knowledge of accurate electronic stopping powers is essential to estimate the *projected range* ( $R_p$ ) of particles defined as the mean depth measured in perpendicular direction from the target surface at which they come to halt. An analytical approach of Ziegler et al. based on transport theory, together with the ZBL stopping power database, led to the development of the widely used SRIM (Stopping and Range of Ions in Matter) code [5.16]. SRIM is under continuous development and essentially can be used for the simulation of ion implantation into amorphous targets, when projectiles are assumed to undergo random scattering in the material.

Energy loss in multi-elemental compounds can be estimated assuming that the interaction processes between ions and component target atoms are independent of the surroundings. Therefore the stopping power of a compound  $A_xB_y$  ( $x+y = 1$ ) can be estimated as [5.12]:

$$\varepsilon^{AB} = \frac{x\varepsilon^A + y\varepsilon^B}{x+y} \quad (5.7)$$

Formula 5.7 is known as Bragg's rule that is basically assumed to be energy independent. In general, it works fairly well for projectile energies well above the stopping power maximum, whereas largest deviations can be observed around the maximum. These deviations are 10-20 % and usually can be attributed to chemical bonding effects in the target.

For particles, passing through channeling trajectories in crystals the electronic stopping power will be different as compared to projectiles propagating through random scattering. This should be obvious when considering that the electron density is not homogeneously distributed within the axial or planar channels and thus the local electron density, seen by the projectile depends on the actual impact parameter  $P$  of the collision events. In general, this 'local' approximation of the electron density gives a realistic description of the physics involved in the motion of the projectile in a crystalline target. As channeled particles are focused into the center of the channel, their stopping power is expected to be lower than the ZBL random stopping power. The knowledge of channeling stopping powers ( $S_e^{channel}$ ) is especially important in ion-channeling measurements for adequate energy-depth conversion in the evaluation of the depth distributions of target species or irradiation-induced damage. It is important to stress that in practice  $S_e^{channel}$  depends on the target thickness because of the ion flux distribution and projectile charge state. For very thin crystals, the ion flux distribution is nearly uniform and the projectile charge state is equal to the incident one. After distances of the order 100 nm, equilibrium ion flux distributions [5.17] and projectile charge states [5.18] are achieved. If the crystal is too thick, than  $S_e^{channel}$  may approach the random  $S_e^{ZBL}$  due to dechanneling at crystal defects, thermal vibrations and electronic multiple scattering. Consequently, experimental values of  $S_e^{channel}$  represent the average of the stopping power of highly and poorly channeled particles and depend on the actual measurement conditions. To calculate  $S_e^{channel}$ , a semi-empirical expression can be used, based on the impact-parameter dependent Oen-Robinson formula [5.19]:

$$S_e^{channel} = S_e^{ZBL} \frac{\exp\{-C_{el} 0.3[R_0(E, P)/a]\}}{\int_0^{P_{max}} 2\pi P dP \exp\{-C_{el} 0.3[R_0(E, P)/a]\}} \quad (5.8)$$

where  $a$  is the universal screening length (adopted from SRIM) and  $R_0(E, P)$  is the distance of closest approach in a binary collision depending on the projectile energy  $E$ , and the impact parameter  $P$ , respectively.  $C_{el}$  is an empirical parameter depending on the energy and the direction of incident ions.  $C_{el}$  can be fitted to experimental results. Equation 5.8 is used in an improved version of the SRIM code, called Crystal-TRIM. This program has been originally written by Matthias Posselt for Si [5.20] and later was modified by András Ster and Matthias Posselt for SiC [5.21]. Note that another parameter, the screening parameter  $C_\lambda$  of the ZBL electronic stopping cross-section is also used in the program [5.20, 5.21] in the calculation of electronic stopping processes. Crystal-TRIM takes into account the crystalline structure of the target and allows the simulation of ion implantation for different projectile-target orientations. Crystal-TRIM is used in this thesis in the discussion of experimental results. Further details of the code can be found in Refs. 5.20, and 5.21.



## Chapter 6

### **Profiling crystal defects by Ion Backscattering Spectrometry combined with Channeling (BS/C)**

In this chapter the underlying physical concept of Ion Backscattering Spectrometry (BS) is discussed.

Firstly, some words about notations. Generally, a backscattering technique is referred to as Rutherford Backscattering Spectrometry (RBS) if the cross-section of the analyzing particle with respect to the target atom is Rutherford-type. In this thesis within the energy range applied in He backscattering measurements on SiC, the scattering reactions can be described by Rutherford cross-section for Si, but exhibit a non-Rutherford cross-section for C. Therefore, a simplified notation Backscattering Spectrometry (BS) will be used instead of RBS. If BS is combined with channeling in the crystal the technique can be referred to as BS/C.

In the next section typical parameters of the accelerator and its complementary tools, the scattering chamber and the detection system is briefly summarized. The short introduction is then followed by the details of the BS/C technique.

#### **6.1 Accelerator, scattering chamber, and detector system**

Charged particles, extracted from a gas or solid phase ion source, can be accelerated to high energies by crossing them through a large potential difference. For this purpose, a high voltage must be generated. A widely used method to produce high voltages was realized by Van de Graaff in 1931 [6.1]: a fast moving insulating belt carries charge, which is sprayed at the belt at one electrode, and removed on another one. In this way voltages up to megavolts can be produced. The Van de Graaff accelerator was the pioneer tool for nuclear physics in the 1960s. However, nowadays these devices are still extensively used in materials analysis. The experiments in this thesis have been performed with the EG-2R Van de Graaff accelerator at the Central Research Institute for Physics in Budapest. This equipment has been installed in 1969, and nowadays is working for materials analysis of thin layer structures. The maximum accessible voltage is 5 MV, however, in practice the energy range above 4.5 MeV is usually not employed. Fig. 6.1 shows the schematic picture of the accelerator-scattering chamber-detector system.

To produce a monochromatic beam consists only of one specific ion species a 90° deflection magnet is applied as mass and charge state separator. Then a combination of vertical and horizontal deflection magnets and multi-sector slits guide the beam to the sample chamber allowing collimation and focusing.

Since in BS/C technique usually the comparison of different spectra provides quantitative information about the sample, one limitation factor is the reproducibility of the number of incident particles in the analyzing beam. For Budapest accelerator the particle number is determined by a transmission Faraday cup [6.2] which combines the good characteristics of a Faraday cup and the beam chopper techniques. In this method, a rotating beam chopper periodically detects the beam current and the precise number of incident ions is determined by simple current integration. The surrounding Faraday cup isolates the system

from the disturbing current of secondary electrons sputtered from the sample surface. Our helium BS test measurements showed an average particle number reproducibility of 1% that offers accurate BS/C analysis.

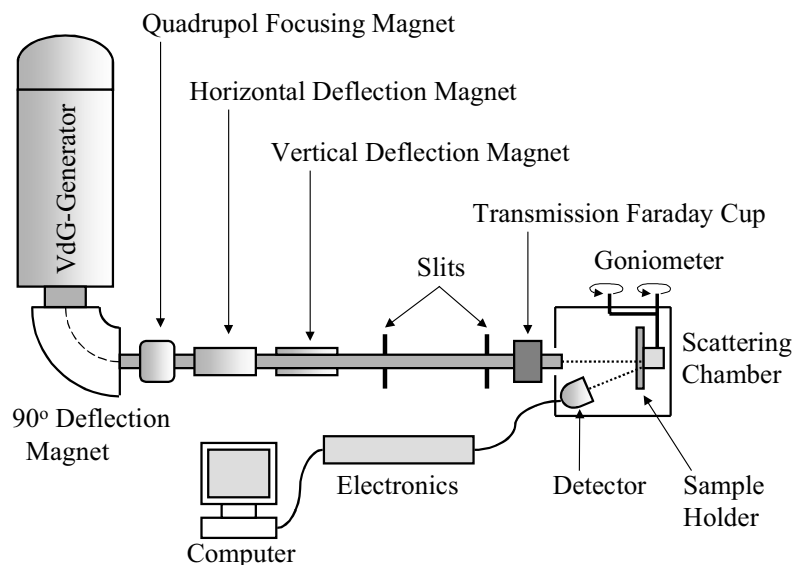


**Figure 6.1** Schematic picture of the EG-2R Van de Graaff accelerator-beam guiding-scattering chamber-detector system in Budapest.

The sample is fixed on an aluminum sample holder connected to a two-axis goniometer system capable of determining the target orientation with a precision of  $0.01^\circ$  both in tilt and angular dimensions. It is important to prevent the sample from possible beam-heating effects, providing good thermal coupling between the sample and the holder. In addition, the beam current can be kept low, usually at about 10-20 nA for the same purpose. Another reason to keep low ion current is to avoid the so-called pile-up effect when detecting backscattered particles. If the time response of the electronics of the detector system is not fast enough to separate the individual impacts on the detector due to the high time rate of encounter events, two or more individual impacts will be detected as one signal leading to false results and loss of information. The problem can be solved adjusting low beam current to decrease the time rate of encounter events to be detected.

It is also important to protect the sample from surface sputtering and ion-mixing caused by the analyzing He beam itself. In our case, the sputtering in a standard BS/C experiment always less than one atomic layer of the sample, due to low sputtering rates for SiC. It is also valid for N and Al implantation in the applied fluence ranges.

In the sample chamber the vacuum is better than  $10^{-4}$  Pa to avoid hydrocarbon deposition. This carbon content is carried by the analyzing particles through the collision with residual free gas molecules in the chamber. To eliminate these free particles, liquid  $N_2$  cooled traps are used along the beam path and around the wall of the chamber. A control 3.5 MeV He analysis using Si sample revealed that in our standard measurement conditions the surface carbon deposition is negligible ( $\sim 2 \times 10^{15}$  C atoms  $cm^{-2}$ , being about 1 monolayer of Si).

The backscattered He particles are detected with ORTEC solid-state surface barrier detectors operating under forward bias of 50 V or 100 V. The signal is amplified and transmitted to a multi-channel analyzer connected to a computer-controlled data acquisition

set. BS/C measurements can be monitored online. The sample position can be changed by a remote-controlled stepping motor system, installed on the sample holder.

## 6.2 Backscattering Spectrometry/Channeling

BS methods have become the predominant ion beam techniques for quantitative analysis of medium and heavy elements in thin films. Main reasons are non-destructive nature, simplicity and identification power, offering the possibility of simultaneous multi-element profiling, and good depth resolution. Moreover, BS/C gives information on crystal orientation and quality allowing the simultaneous depth profiling of irradiation-induced damage in multi-component crystals like SiC.

In BS experiments, the detector is placed at an angle larger than  $90^\circ$  with respect to the beam direction and only backscattered particles are detected. The backscattering yield vs. the energy of the projectiles is measured and the spectrum holds information about two important things: (1) the masses and (2) the depth distribution of the target constituents.

BS/C experiments can be understood by considering three important physical subjects, kinematics, stopping power, and cross-section. Moreover, two effects, the energy straggling and multiple scattering limit the accuracy of BS. All these factors are treated in this section.

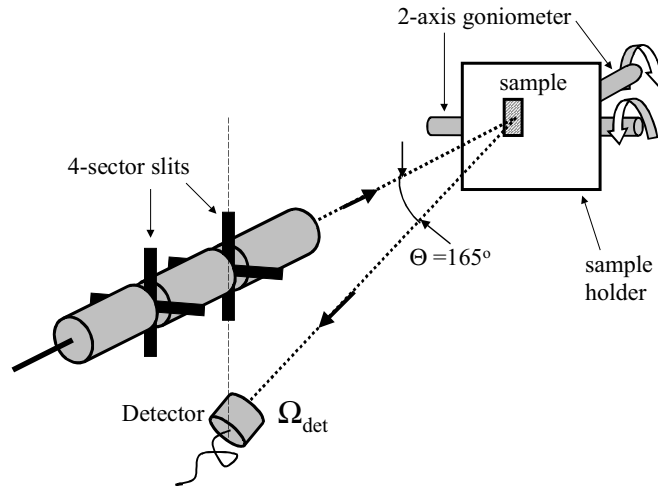


**Figure 6.2** Schematic view of the experimental setup for channeling experiments arranged in Cornell geometry.

### 6.2.1 Kinematic factors: qualitative analysis

A typical geometry of a scattering experiment is given in Fig 6.2. This arrangement where the detector is placed below the plane determined by the incoming beam and the sample surface normal is called Cornell geometry. Another possibility is IBM geometry, where the incoming beam, the detector, and the sample surface normal are co-planar. All the measurements reported in this thesis were performed in Cornell geometry with a backscattering angle of  $165^\circ$ . Restricting ourselves to the case of elastic scattering, the energy  $E_f$  of the scattered projectile can be calculated from the laws of conservation of energy and momentum [6.3]:

$$E_1 = K_1 E_0 = \left[ \frac{M_1 \cos \Theta \pm (M_2^2 - M_1^2 \sin^2 \Theta)^{1/2}}{M_1 + M_2} \right]^2 E_0 \quad (6.1)$$

At a fixed detection angle, the so-called kinematic factor  $K_1$  only depends on the mass ratio  $M_1/M_2$ . The plus sign in Equation 6.1 holds when  $M_1 < M_2$ , whereas for  $M_1 > M_2$  there are two solutions and therefore there are two different kinematic factors  $K_1$  for the scattered particle at the laboratory angle  $\theta$ , corresponding to different recoil angles  $\varphi$ .

In principle, the sample components could be identified in a BS experiment because projectiles scattered at different target masses all have different energies according to Equation 6.1. For example for 3.55 MeV He ions scattered at  $\theta = 165^\circ$  the kinematic factors for Si and C are  $K_1(\text{Si}) = 0.57$  and  $K_1(\text{C}) = 0.26$ , respectively. However, these values are only valid at the sample surface and for a fixed angle  $\theta$ . In a real experiment, the scattering situation is not ideal and the overall energy resolution  $\delta E$ , and thus the depth resolution  $\delta x$ , is limited by several factors. These effects will be described here focusing on 3.55 MeV  $^4\text{He}^+$  BS/C analysis and the actual measurement conditions used in this thesis.

- (1) The energy resolution of the detector  $\delta E_{det}$  accounts for the first factor. Normally, our ORTEC detectors have an energy resolution of 16-20 keV in the applied energy range.
- (2) The energy spread of the projectile energy  $\delta E_0$  is the second contribution. It is usually largely depends on the type of the accelerator used. For the EG-2R Van de Graaff accelerator in Budapest  $\delta E_0$  can be the order of  $\sim 1$  keV that means  $\sim 0.1$  % of the accelerator energy.
- (3) The finite size, i.e. the solid angle  $\Omega$  of the detector is also a factor of limitation. This means that the angle of detection is not exactly  $\theta$ , but rather  $\theta \pm \Delta\theta$ . In our case the radius of the active window of the detector is 4 mm and the distance  $d$  between the detector and the sample is 12.5 mm ( $\Omega = 2.5$  msrad), resulted in  $\delta E_{size} = 10$  keV energy spread for a 3.55 MeV He projectile backscattered from a surface Si target atom at  $\theta = 165(\pm 1.9)^\circ$ .
- (4) The finite size of the beam spot causes angular differences in the detector and thus an uncertainty of the recoil kinematic energy,  $\delta E_{spot}$ . In our case the dimensions of the analyzing beam are usually  $0.5 \times 0.5$  mm, so that  $\delta E_{spot} < \delta E_{size}$ .
- (5) The fifth factor, playing role in the accuracy of energy measurements, is the divergence of the accelerator beam. Using two sets of four-sector slits to collimate the beam to the dimensions given above, the maximum beam divergence is about  $0.05^\circ$ . This divergence still gives good channeling conditions considering that Barrett's formula in Equation 5.4 gives an angular half width  $\Psi_{1/2} = 0.4^\circ$  for the analyzing He ions.

The mass resolution in BS measurements is defined as  $\delta M_2 = ((\delta E / \delta E_0) / (dK_1 / dM_2))$ . One can deduce from Equation 6.1 that for fixed  $\delta E / \delta E_0$  mass resolution improves with increasing projectile mass. Moreover,  $dK_1 / dM_2$  is largest at  $\theta = 180^\circ$ , therefore a very backward angle is promising for an optimal mass resolution. Besides the larger information depth, this is the reason to use a backscattering angle  $\theta = 165^\circ$  in our experiments.

### 6.2.2 Stopping power: depth profiling

When the accurate stopping power  $S_e$  for the analyzing beam-target system is known it can be used to extract depth information from measured energy spectra. This can be seen in Fig. 6.3 for a BS experiment. A projectile impinges on the target at an angle  $\Psi_1$  with respect to the surface normal and leaves the sample at angle  $\Psi_2$ , respectively. A recoil from the surface has an energy  $E_1 = K_1 E_0$ . When the close encounter event occurs at a depth  $t$ , the energy of the recoil upon leaving the sample is [6.3]:

$$E_2 = K_1 \left( E_0 - \frac{t}{\cos \Psi_1} \int S_e^{in}(x) dx \right) - \frac{t}{\cos \Psi_2} \int S_e^{out}(x) dx \quad (7.2)$$

For a BS/C channeling experiment, performed in a perfect crystal the electronic stopping powers along the inward ( $S_e^{in}$ ) and outward ( $S_e^{out}$ ) paths are equivalent to the channeling ( $S_e^{channel}$ ) and random ( $S_e^{ZBL}$ ) stopping powers.

The energy difference  $\Delta E$  between a recoil originating from the surface and another recoil originating from depth  $t$  is:

$$\Delta E = E_1 - E_2 = t \left( \frac{K_1}{\cos \Psi_1} \int S_e^{in}(x) dx + \frac{1}{\cos \Psi_2} \int S_e^{out}(x) dx \right) \equiv t[S] \quad (6.3)$$

The quantity  $[S]$  is the ‘energy loss factor’ that makes the relationship between energy and depth information. It also relates the energy resolution  $\delta E$  to depth resolution  $\delta t$  via  $\delta t = \delta E/[S]$ . Here  $\delta t$  is the minimum thickness that can be experimentally resolved.

Now, taking into account Equation 6.3 and the limitation factors (1)-(5) described in the previous paragraph, the overall depth resolution achieved in a 3.55 MeV BS/C measurement on SiC at Budapest accelerator can be calculated. Using for this purpose the DEPTH code [6.4] developed by E. Szilágyi results in  $\delta t \approx 30$  nm at the sample surface.

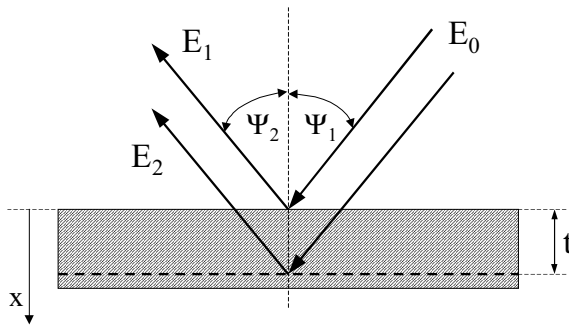


**Figure 6.3** Schematic model of depth profiling in backscattering analysis. Recoils scattered from the surface have energy  $E_1$ , while recoils scattered from depth  $t$  have energy  $E_2$ . Note that the  $x$ -axis is perpendicular to the surface of the sample.

### 6.2.3 Differential cross-sections: quantitative analysis

The scattering cross-section can be determined exactly when the interaction of the projectiles with the target atoms is governed by Coulomb repulsion. In this case the energy of the projectile is within the so-called ‘Rutherford window’. Above the lower limit of this window the energy is sufficiently high so that the impact parameter of the collision is low

enough compared to the Bohr radius, and therefore screening by electrons can be neglected. On the other hand, the upper limit is exceeded when the projectile energy is so high that the distance of closest approach reduces to the dimension of nuclear size and nuclear forces starts play role in the scattering process. However, the borders of the Rutherford window are functions of the scattering angle  $\theta$ . Within the Rutherford window, the differential cross-section for scattering of a projectile into a solid angle  $d\Omega$  centered around an angle  $\theta$  in the laboratory frame of reference can be given as [6.3]:

$$\left(\frac{d\sigma}{d\Omega}\right)_{\text{projectile}} = \left(\frac{Z_1 Z_2 e^2}{4E}\right)^2 \frac{4\left(\sqrt{M_2^2 - M_1^2 \sin^2 \Theta} + M_2 \cos \Theta\right)^2}{M_2 \sin^4 \Theta \sqrt{M_2^2 - M_1^2 \sin^2 \Theta}} \quad (6.4)$$

The total yield  $Y_j$  of scattered projectiles for a specific element  $j$  as measured in the detector is written as:

$$Y_j = N_j Q \Omega \sigma_j \quad (6.5)$$

where  $N_j$  is the number of target atoms per unit area,  $Q$  is the total number of incident projectiles,  $\Omega$  is the solid angle of the detector and  $\sigma_j$  is the differential cross section averaged over the surface of the detector. When  $Y_j$ ,  $Q$ ,  $\Omega$ , and  $\sigma_j$  are known it is easy to determine  $N_j$  and thus to quantify results. This process only works if the cross-sections are well known, which is often the case in standard BS work.

Since the differential cross section in Equation 6.4 scales with  $Z_2^2$ , standard RBS is more sensitive for the detection of elements with high  $Z$ . For example,  $(d\sigma/d\Omega)_{\text{projectile}}$  for silicon at  $\theta = 165^\circ$  is about 7 times higher than for carbon. Since the kinematic factor  $K_l$  is larger for Si than for C the He backscattering yield of C can be detected at lower energies. Consequently, in a sample, several microns thick, the carbon yield overlaps with a broad silicon background originated from the bulk material. These conditions makes the detection of backscattering yield from the carbon sublattice of SiC quite difficult, when measuring within the Rutherford window (i.e. at standard RBS energies of 1-2 MeV).

Using a simple estimation of  $\sim 0.3 Z_1 Z_2^{2/3}$  MeV [6.3], the high-energy borders of the Rutherford window for scattering of He ions on Si and C atoms are about 3.5 MeV and 2 MeV, respectively. Above these energies, the nuclear forces start to play role in scattering processes. The cross-section then no longer shows a smooth dependence on the incident energy and in principle smaller than the Rutherford value. However, resonances in the cross-section may exist. These resonances usually show strong angular dependence and often can be advantageous for BS, because – especially at higher energies – the cross-section can be orders of magnitude larger than the Rutherford value. The width of these resonances can vary over a large range from several keV to hundreds of keV. The use of broad resonances (overlapping resonances), exhibiting a constant cross-section in a sufficiently large energy range, is favorable because the yield than only depends on the concentration (see Equation 6.5) and therefore efficient depth profiling can be realized. An example of such a resonance structure with a width of hundreds of keV exists in the elastic reaction  $^{12}\text{C}(\alpha, \alpha)^{12}\text{C}$  in the energy range 3.2-4 MeV.

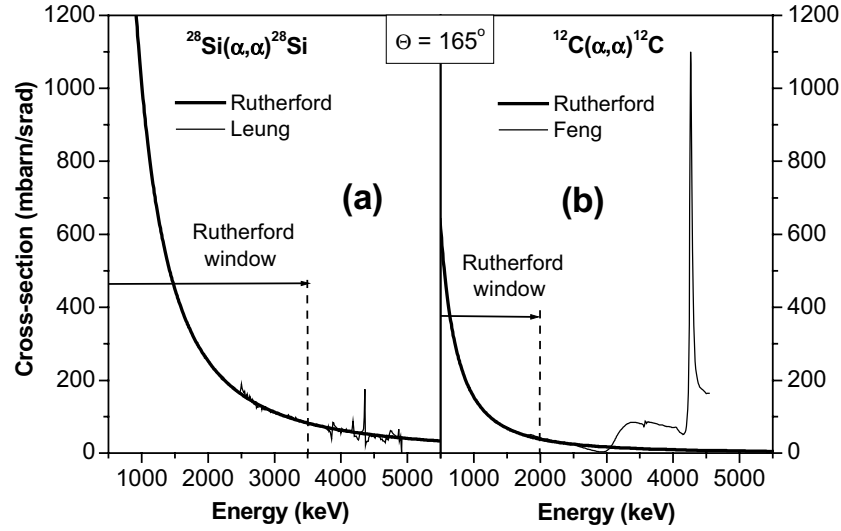


**Figure 6.4** Cross-sections of  $^{28}\text{Si}(\alpha,\alpha)^{28}\text{Si}$  [6.5] and  $^{12}\text{C}(\alpha,\alpha)^{12}\text{C}$  [6.6] elastic scattering reactions along with the corresponding Rutherford cross-sections. The Rutherford windows are marked by arrows.

Fig. 6.4 shows the cross-section of the  $^{28}\text{Si}(\alpha,\alpha)^{28}\text{Si}$  and  $^{12}\text{C}(\alpha,\alpha)^{12}\text{C}$  scattering reactions in a wide energy range. Data are taken from tabulated values reported by Leung [6.5] and Feng [6.6], respectively. The plateau in the cross-section of carbon below 3.5 MeV has been used throughout the BS/C experiments presented in this thesis. It offers the possibility to have a large analyzable depth range of several hundreds of nm, while sensitivity is also enhanced as the cross-section in this region at  $\theta=165^\circ$  is about 6 times the Rutherford value. Since in this energy range for the cross-section of silicon still the Rutherford value applies (see Fig. 6.4), the He backscattering yield from the C sublattice is comparable to that from the Si sublattice. It can be seen in Fig. 6.5a that shows a non-channelled, i.e. random BS spectrum, recorded on SiC with 3.55 MeV energy He ions. In addition Fig. 6.5b shows a conventional random RBS spectrum recorded on the same sample at 1.5 MeV He energy. The benefit of 3.55 MeV BS contrary to 1.5 MeV RBS for carbon depth profiling is obvious.

Besides 3.55 MeV BS/C we mention two alternative techniques applied to overcome the problem of carbon depth profiling in SiC. The first is the use of  $^{12}\text{C}(\alpha,\alpha)^{12}\text{C}$  nuclear resonance for C at 4.265 MeV  $\text{He}^+$  energy, giving an enhancement factor of 120 in the cross-section of C as compared to the Rutherford value [6.7]. As Fig. 6.4 shows this resonance peak is very sharp, giving an increased signal only from a narrow depth region of the C sublattice. The second method is  $^{12}\text{C}(\text{d,p})^{13}\text{C}$  nuclear reaction in combination with channeling [6.8, 6.9]. Unlike the conventional BS/C method, this technique gives a silicon-background free signal from C atoms because the nuclear reaction is accompanied by an energy release of 2.723 MeV and therefore the spectrum for C is shifted toward high energies.

The depth resolution at the surface in our standard measurement conditions – as calculated by DEPTH code – is about 90 nm using the resonance method, and 180 nm for the 0.94 MeV  $^{12}\text{C}(\text{d,p})^{13}\text{C}$  reaction. These are significantly higher values than for 3.55 MeV BS/C (~30 nm).

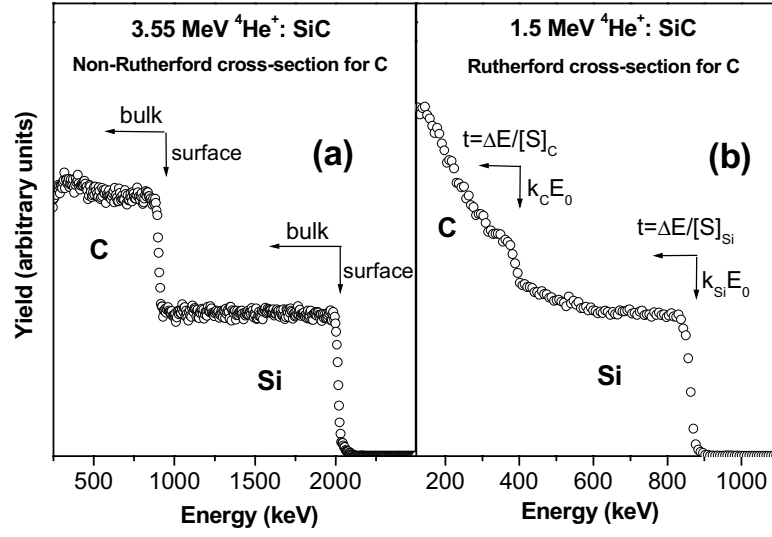


**Figure 6.5** Random BS spectra recorded on silicon carbide both with (a) 3.55 MeV and (b) 1.5 MeV energy He ions. (a) The spectrum edges corresponding to backscattered He particles from surface Si and C atoms and energy regions representing He backscattering from bulk Si or C are marked by arrows. (b) The kinematic factors and layer thicknesses as calculated from energy shifts with respect to the surface edges are schematically depicted.

#### 6.2.4 Straggling, multiple scattering and Doppler broadening: limits in depth resolution

The energy loss of an ion penetrating material is not a continuous process, but rather can be described by a large number of discrete steps. Thus the progress of energy loss exhibits statistical nature. As a consequence, statistical fluctuations in the number of interactions and in the energy transfer result in a spreading of energy, a phenomenon, called energy straggling. Since straggling broadens measured energy distributions it limits the depth resolution. Bohr has given a simple formula for straggling in the high-energy limit:

$$\Omega_B^2 = (1.44eVnm)^2 4\pi NZ_1^2 Z_2 \Delta x \quad (6.6)$$

where  $\Omega_B^2$  is the Bohr value for the variance of the energy loss fluctuation  $\Omega$ ,  $\Delta x$  is the thickness of the traversed material and  $N$  is the atomic density of the target. Straggling increases with the square root of the distance traversed in the material. At a certain depth, straggling will become the dominant contributor over other limitation factors and will limit the energy resolution. Bohr's model assumes fully ionized projectiles of charge  $Z_1 e$ . This assumption is fulfilled only in the Bethe-Bloch region, where  $v_{ion} \gg v_0$ . At lower energies ions are not fully stripped of their electrons and corrections have to be introduced. Firstly Lindhard and Scharff [6.10] have derived corrections, later Chu [6.11] has developed a model for this purpose. However, for 2-4 MeV He ions in targets of low-Z components ( $Z < \sim 20$ ) different models provide quite similar results [6.3]. Fig. 6.6 shows  $\Omega_B$  for He ions in SiC in the function of depth using  $\bar{Z}_2 = 10$  and  $N = N_{SiC}$  in Equation 6.6.

Due to multiple scattering, the trajectories of incoming and outgoing particles in BS experiments are not completely straight. This effect results in changes in angles  $\theta$  and  $\varphi$  and thus influences both the kinematic factors and the cross-sections. Sigmund and Winterborn give an estimation of both the angular and lateral spread due to multiple scattering [6.12]. Nevertheless, this contribution in our case is negligible.



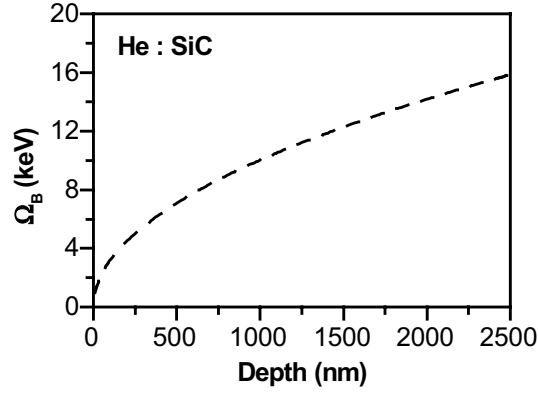


**Figure 6.6** Bohr straggling  $\Omega_B$  in the function of depth for He ions penetrating SiC.

There is one more fundamental physical effect that accounts for limit in depth resolution at non-zero temperatures. Target atoms are subjected to thermal vibrations, that can be an additional source of uncertainty of the energy transmitted in individual collisions with the incoming projectiles, provided that the velocity of projectiles is comparable to the velocity of thermal motion. This phenomenon, called Doppler broadening, gives a contribution to straggling that can be described by a Gaussian function with standard deviation of:

$$\Omega_D^2 = \frac{2mE}{M} kT \quad (6.7)$$

where  $k$  is the Boltzmann constant and  $T$  is the temperature. However, in our case this contribution is negligible. First, because  $\Omega_D$  for a 3.55 MeV He-SiC system is the order of 0.1 keV. Second, because an ion with velocity of  $\sim 10^6 \text{ ms}^{-1}$  passes one atom spacing of  $\sim 1 \text{ nm}$  within  $10^{-15} \text{ sec}$ . This time is much shorter as compared to the reciprocal frequency of thermal vibrations. For example, in SiC the maximum phonon frequency is  $\sim 1000 \text{ cm}^{-1}$  [6.13] with corresponding time constant of about  $10^{-13} \text{ sec}$ . Consequently, the ion senses a ‘frozen’ lattice of static atoms displaced from their equilibrium positions. The statistical nature of the system gives the possibility to describe the distribution of thermal displacements by one Gaussian function and thus handle the problem analytically. This solution can be applied in statistical computer programs – like Crystal-TRIM [6.14] – in the simulation of ion implantation into crystalline targets. However, the value of the r.m.s. thermal vibrational amplitude must be an input parameter.

### 6.3 Disorder analysis

The quantitative depth profiling of irradiation-induced defects in single-crystalline materials using BS/C techniques requires the acquisition of the channeling/backscattering yield of the analyzing particles in the function of their energy (see Fig. 6.5) that is the BS/C spectrum. Then the well-known values of  $Y_j$ ,  $Q$ ,  $\Omega$ , and  $\sigma_j$  in Equation 6.5, as well as the electronic stopping power of the analyzing He ions are used to extract the depth distribution of disorder. This purpose in real BS/C experiments always requires the recording of three corresponding spectra, which are usually measured on different spots of the same sample. These spectra – shown schematically in Fig. 6.7 – are the following:

1. The first spectrum is taken in channeling direction on an undamaged (virgin) spot of the perfect crystal, when the analyzing beam is accurately aligned along the low-index crystallographic direction of the sample that is usually the c-axis for SiC. The perfect alignment is found by the measurement of the angular scan curve. In this case the backscattering yield is minimized, and the spectrum is called virgin or virgin aligned spectrum.
2. In the second measurement the crystal is tilted away from aligned direction by an angle larger than  $\psi_{crit}$  so that the incident particles are not channeled and encounter atoms as they were arranged in a random fashion. This spectrum is called random spectrum and is used to normalize backscattering yields of aligned channeling spectra. In practice, when recording random spectra, the sample is usually tilted off by  $7^\circ$  from the c-axis, and is continuously rotated in order not to prefer any specific crystallographic direction.
3. The third spectrum is taken in channeling direction on the implanted spot of the crystal, aligned exactly the same manner as in case of the virgin spectrum. It can be referred to as the implanted aligned spectrum.

These spectra are measured under the same external conditions, i.e. beam spot size, beam current, measurement fluence, the same adjustment of the collimator and focusing system of the analyzing beam, and same detection system. Therefore, any difference in the detected yields  $Y_j$  between the virgin and random spectra can only originate from the different sample orientations. Moreover, any difference in the yields between the virgin and the implanted aligned spectra can only be attributed to the presence of crystal defects as excess dechanneling sources in the implanted sample.

In disorder analysis of implanted samples one can treat the beam in the crystal at depth  $x$  as the product of two components (see Fig. 5.2): a non-channeled or random fraction  $\chi_R$ , and a channeled fraction  $1-\chi_R$ , respectively. The random component at depth  $x$  originates from particles that are initially non-channeled and particles that are initially channeled but are dechanneled during their path to a depth  $x$ . The presence of defects in the crystal in concentration  $c_D(x)$  and dechanneling factor of  $\sigma(x)$  leads to the increase in the random fraction  $\chi_R$ . In the analysis the random fraction as a function of depth in the virgin spectrum  $\chi_V(x)$  is compared to the yield of the implanted aligned spectrum  $\chi_D(x)$ , and both of them are normalized to the random spectrum. Obviously,  $\chi_V(0) = \chi_{min}$ , whereas  $\chi_V(x)$  includes the fraction initially not channeled,  $\chi_{min}$ , and the low fraction dechanneled in the perfect crystal by thermal vibrations and multiple scattering events. Note for a perfect undamaged single crystal SiC layer  $\chi_{min}$  is 2-3 % along the c-axis when bombarding by 3.5 MeV He ions.

The dechanneling fraction of the implanted crystal  $\chi_R(x)$  can be calculated as [6.15]:

$$\chi_R(x) = \chi_V(x) + [1 - \chi_V(x)] \prod_i \exp \left[ - \int_0^x \sigma_{Di} c_{Di}(x) dx \right] \quad (6.8)$$

where  $c_{Di}$  and  $\sigma_{Di}$  are the density and the normalized dechanneling probability for the  $i$ th type defects. In general both direct scattering from point defects and dechanneling from multiple scattering events and thermal vibrations as well as extended defects contributes to  $\chi_R(x)$ .

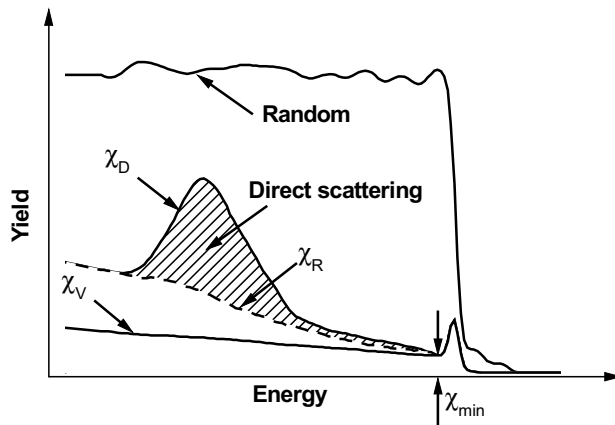


**Figure 6.7** Change in backscattering yield with energy (depth) through a region of disorder that gives rise to both dechanneling and direct scattering. The corresponding virgin and random yields are also depicted.

Fig. 6.7 shows the change in backscattering yield in the function of depth through a disordered region that causes both dechanneling and direct scattering. The difference between yields  $\chi_D$  and  $\chi_R$  originates from direct backscattering on point defects. The solution of Equation 6.8 for  $c_D(x)$  requires an iterative procedure because of the direct and dechanneling contributions. In the presence of only one specific type of defect, e.g. interstitials, the problem can be solved in a relatively simple manner by dividing the sample into small depth intervals. The defect distribution is derived numerically starting from the surface. Finding  $c_D$  in the first interval allows the calculation of the amount of dechanneling for the next interval. The procedure is continued until the end of the disordered region is reached. This evaluation procedure of disorder can be processed using the RBX code developed by E. Kótai [6.15]. RBX requires the measured virgin, random and implanted aligned spectra as an input dataset. Using the virgin and random spectra as references the implanted aligned spectrum can be fitted step-by-step as described above. Reaching the end of the disordered region, the difference in the measured and calculated dechanneling yield behind the damaged region shows the validity of our assumption about the defect type and disorder structure. The assumed depth distribution of disorder can be varied independently in the Si and C sublattices of SiC. RBX also takes into account detector resolution, multiple scattering and Bohr straggling, as the dominant factors limiting depth resolution. The program is under continuous development. BS/C spectra in this thesis were evaluated using the RBX code. Further details of the program can be found in Ref [6.15].

Combination of channeling with other methods can yield specific information on ion bombardment caused lattice imperfection. For example, axial and planar channeling together with Mossbauer spectroscopy proved to be appropriate methods for investigation of ion implantation-induced lattice damage in highly oriented pyrolytic graphite [6.16]. The degradation of the mosaic spread of the damaged carbon layers was found after Co and Xe implantation [6.16].

## **Chapter 7**

### **BS/C studies on ion-implanted SiC**

In this chapter my own BS/C studies on implantation-induced defects in single crystal 4H and 6H-SiC wafers are summarized.

Firstly, section 7.1 reports damaging effects during 3.5 MeV He BS/C measurements induced by the analyzing beam itself. Here the aim is to optimize the measurement conditions, i.e. reach a satisfactory measurement statistics whilst keeping the amount of induced damage at low level by varying the measurement fluence and fluence rate. The main features of damage accumulation vs. the implanted He fluence are discussed in this section.

Section 7.2 presents 3.5 MeV He BS/C measurements of the depth distribution of damage in both the Si and C sublattices of SiC implanted with 200 keV Al ions to different fluences. The shape of damage distributions, extracted from BS/C spectra are compared to the results of SRIM computer simulations and effective displacement energies are derived both for the Si and C sublattices.

Finally, section 7.3 gives a comprehensive study of damage formation in 6H-SiC as measured after 500 keV N implantation. The disorder accumulation as a function of the fluence for different initial directions of the implanted ions with respect to the crystallographic c-axis of 6H-SiC is investigated. The possible role of point defects and extended defects in damage formation is discussed. The efficiency to reduce damage by means of channeling implantation is also studied and compared to the results of Crystal-TRIM computer simulations. As an additional result, the (average) electronic stopping power for the analyzing He ions along the c-axis of hexagonal SiC in standard measurement conditions is determined, and is used for an adequate energy-depth conversion in the evaluation of the aligned BS/C spectra of the Si and C sublattices of ion-implanted SiC.

## 7.1 Damage accumulation in 4H-SiC induced by 3.5 MeV He ions during Backscattering Spectrometry/Channeling (BS/C) measurements

### 7.1.1. Introduction

In general, BS/C can be considered as a non-destructive method since using high energy, low-mass ions, the analyzing ion beam induces defects only in a dilute concentration in the region where BS claims reliability. At the  $R_p$  of the He ions ( $\sim 9 \mu\text{m}$  at 3.5 MeV in SiC for irradiation along random direction), the defect concentration is higher. However, these defects are far away from the active layer of the device being close to the surface. In case of Si, these defects can be removed by annealing at relatively low temperatures. On the contrary, SiC, being a compound semiconductor with good thermal conductivity, is much more sensitive to irradiation than Si [7.1]. In contrast to Si, even implantation with light ions (H or He) can induce amorphization of single crystalline SiC at room temperature [7.2]. Thus, the damage caused by the probing beam may interfere with the results of channeling analysis. Therefore, an understanding of the damage formation during channeling analysis, especially, for damage located in the surface region, is of crucial importance to proper measurement evaluation.

It has been shown that 1.7 MeV energy He ions with a relatively low fluence can induce a low damage level extending up to the surface of the irradiated SiC, which stems primarily from the low level of elastic energy deposition [7.3]. In this region, defect distribution can be considered as constant [7.4]. The higher damage level at  $R_p$  gives rise to a change in color of the sample. At higher fluences, a distinguished amorphous layer was formed around  $R_p$ , and clusters of point defects were found in the upper layer [7.5]. The damage accumulation in the sample is accompanied by swelling of the implanted area, which is originated from the defects near the surface, as confirmed by the higher swelling found for irradiation along random direction compared to channeling direction [7.4].

Recently, an effective technique called Smart-Cut [7.6] was proposed for transferring a thin single crystalline SiC layer onto an inexpensive insulating substrate to reduce the costs. To this end H, or most recently, H and He implantation was proposed for layer splitting [7.7]. Also for the "ion cut" technique, it is essential to study the H and He ion implantation induced damage near the SiC surface.

In the present study I investigate the damage accumulation induced by 3.5 MeV He ions in the near-surface region of 4H-SiC with the fluence ranging from that commonly used for RBS/C analysis ( $10^{16}/\text{cm}^2$ ) to the one needed for layer splitting techniques ( $10^{17}/\text{cm}^2$ ). The effect of He ion beam density on the defect formation is also investigated.

### 7.1.2. Experimental details

A  $\langle 0001 \rangle$  4H-SiC wafer was exposed to a 3.5 MeV  $\text{He}^+$  ion beam with a beam size of  $\sim 0.5 \times 0.5 \text{ mm}^2$  at different beam intensities using the 5 MeV Van de Graaff accelerator in Budapest. An advantage is that the high ion energy of 3.5 MeV reduces the nuclear cross-section and thus the ion induced damage in the surface region, as compared to the conventionally used RBS analysis in the 1-2 MeV He energy region.

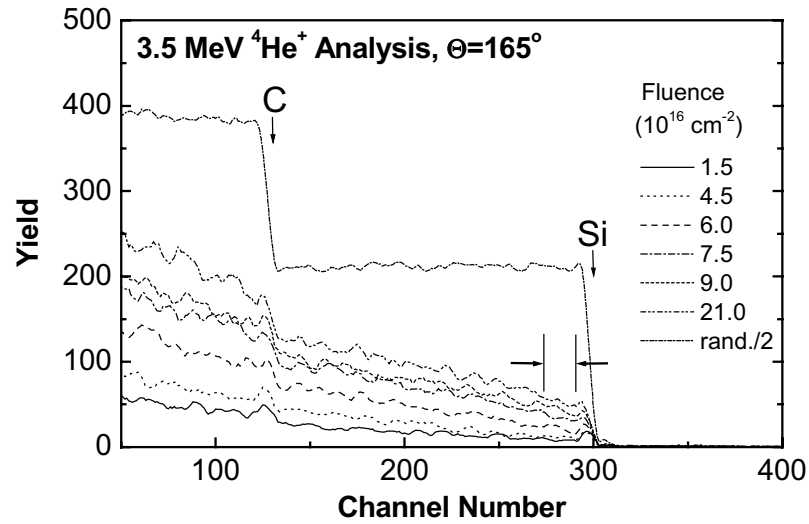
The samples were irradiated along channeling direction (c-axis) with total implanted charge of 100  $\mu\text{C}$ , in 5  $\mu\text{C}$  steps. RBS/C spectra at backscattering angle of  $165^\circ$  were taken simultaneously in Cornell geometry during each step of irradiation. The aligned spectra were

recorded also alternately with  $7^\circ$  off-normal random irradiation with low beam density. This case, though the effect is a mixture of random and channeled irradiation, for simplicity, it is marked as random irradiation. The actual values of ion beam densities as well as irradiation fluences were corrected using the irradiated areas of the samples determined by optical microscope after finishing the RBS measurements.

The swelling of He implanted SiC was measured by Alfa-step 100 apparatus (TENCOR Instruments) across the implanted area. According to Alpha-step results, the height change over the implanted area remains less than 4% of the average height.

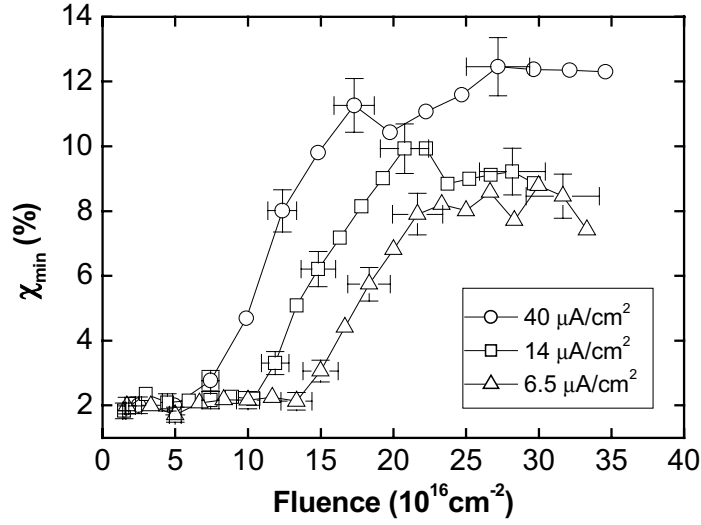
### 7.1.3. Results and discussion

Fig. 7.1 shows channeling spectra obtained with  $40 \mu\text{A}/\text{cm}^2$  beam density at a regular scattering angle ( $165^\circ$ ). The accumulated fluences include also the measuring fluence. As one can see, the spectrum height increases with fluence, but not linearly. This reveals that damage accumulation occurs during irradiation. In our case, due to light ion mass and high energy, the damage distribution in the surface region can be considered as homogeneous, which is supported by the shape of the RBS channeled spectra. The damage accumulation near the surface region then can be followed by the minimum yield ( $\chi_{\min}$ ) determined using the area integral of the region marked by the horizontal arrows in Fig. 7.1.



**Figure 7.1** BS channeled spectra of 4H-SiC irradiated with  $40 \mu\text{A}/\text{cm}^2$  He ion beam density. The random yield was divided by a factor of 2 to fit the scale. The region used for  $\chi_{\min}$  determination is marked by the arrows.

The development of the minimum yield for different beam densities as a function of irradiation fluence is drawn in Fig. 7.2. For each beam density, the  $\chi_{\min}$  vs. fluence curve can be divided into three regions. At low fluence,  $\chi_{\min}$  remains unchanged with its value around 2% {region (1)}. After this region,  $\chi_{\min}$  increases almost proportionally with fluence {region (2)}, and later it tends to be saturated {region (3)}. The higher the beam density, the sooner the  $\chi_{\min}$  starts to increase with fluence and later on, in {region (3)}, the higher density increases the saturation  $\chi_{\min}$ , however, non-linearly.



**Figure 7.2**  $\chi_{\min}$  as a function of fluence for 4H-SiC irradiated along channeled direction with different 3.5 MeV He ion beam densities.

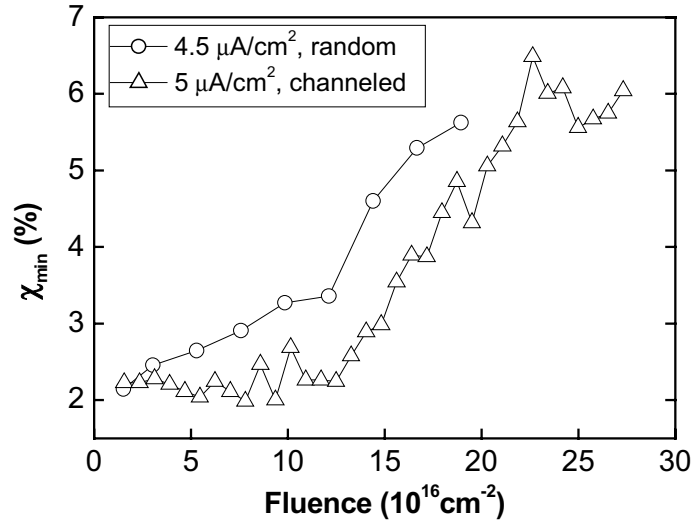


**Figure 7.3**  $\chi_{\min}$  as a function of fluence for 4H-SiC irradiated along channeled and random direction with low 3.5 MeV He ion beam density.

For comparison, irradiation along random direction for the lowest beam density (around  $5 \mu\text{A/cm}^2$ ) was also carried out. The  $\chi_{\min}$  values are about 30-40% higher for random irradiation compared to those of channeled irradiation, as seen in Fig. 7.3. It is obvious that the probability of elastic nuclear collisions between ions impinging in random direction and the target atoms is higher compared to channeled irradiation, thus giving rise to formation of more defects.

First we have to verify whether the increase of  $\chi_{\min}$  can be due to the surface damaged layer. This is less likely, because the so-called anomalous surface amorphization during ion bombardment is very weak for high-energy light ions [7.8]. The evaluation of channeled spectra by RBX code revealed [7.9] that the differences in  $\chi_{\min}$  compared with the first

channeled spectrum (considered as a virgin) can be caused by damage levels increasing up to 10 % and distributed homogeneously in the function of depth.

The effect of ion beam density on damage accumulation can also be followed by measuring swelling of the irradiated area. Swelling on SiC can be easily observed even by naked eye, being impossible on Si. The height of the swelling measured by Alfa-step, as a function of irradiation fluence, is shown in Fig. 7.4. Higher ion beam density results in bigger step-height over the fluence range studied. The effect of random irradiation seems to be very strong in spite of low beam density used for this kind of irradiation. The data show non-linearity in the dependence of swelling on fluence, which is consistent with the observations on 1.5 MeV He<sup>+</sup> implanted 6H-SiC, where lower fluence range was applied [7.4]. These observations confirm the fluence rate dependence of beam induced defects, since it has been shown that the volume expansion of the ion damaged crystal, i.e. the step-height is proportional to the defect density plus an additional relaxation occurring at the onset of the crystalline to amorphous transition [7.10].

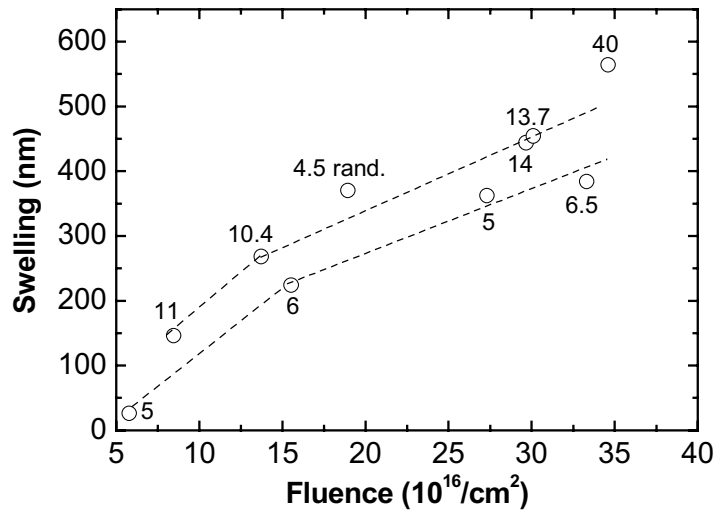


**Figure 7.4** Swelling as a function of fluence for 4H-SiC irradiated along channeled direction. The numbers refer to the ion beam densities ( $\mu\text{A}/\text{cm}^2$ ). The value for random irradiation is marked by 'rand'.

The presence of {region (1)} in the damage accumulation process can be explained by several reasons. Firstly, full-cascade SRIM simulations, performed for 3.5 MeV He implantation into SiC along random direction with displacement energies of 20 and 30 eV for C and Si reveals a damage generation rate per unit depth of  $2 \times 10^4$  (vacancy/ion)  $\text{cm}^{-1}$ . Using this generation rate, for a fluence of  $10^{16} \text{ cm}^{-2}$  the fraction of displaced atoms will be 0.002, i.e. one order of magnitude lower than  $\chi_{\min}$ . However, in practice the generation rate is expected to be lower as the implantation has been performed along channeling direction. Therefore, the damage created close to the surface in the low-fluence region {region (1)} may be within the statistical fluctuation of  $\chi_{\min}$ .

On the other hand, it is well known that the defect level in single-crystalline SiC, due to present growth technologies, can be higher than in Si. These as-grown defects may act as sink for the irradiation defects at the starting stage of implantation. Although the point defects generated by the ion beam are not as mobile as they are in Si, sometimes their recombination



can be observed even at room temperature [7.5,7.11]. Therefore, we tentatively think that the recombination of primary defects at intrinsic sinks may be enhanced by the higher concentration of those defects in SiC, which characterize the starting stage {region (1)}. Later, as these sinks begin to saturate the concentration of stable defects can start to increase {region (2)}. The different threshold fluences to start {region (2)} for different fluence rates suggest that the faster the defect generation, the higher the amount of stable defects formed per unit time.

The sublinear nature of damage accumulation in {region (3)}, where the damage level tends to saturate about 10 % (well below amorphization), is in agreement with the observations of Matsunaga et al. [7.12] performed on electron-irradiated SiC. This behavior shows the nature of damage formation in the near-surface region for He implantation to be an extreme case of ion beam-induced disorder formation processes in SiC. As it can be derived from Equation A2.1 in Appendix 2, here the dominant contributor to damage formation is term  $S_d$ , that describes the accumulation of single point defect in residual crystalline regions. Thus term  $f_a$ , that accounts for direct-impact, defect-stimulated amorphization processes in collision cascades seems to be absent. It is expected, since He implantation-induced cascades in the surface region are extremely dilute, and the probability to directly produce amorphous nuclei in the core of a cascade can be negligible. Accordingly,  $f_a$  can be eliminated and the level of disorder can be kept at ~10 % for a long time that can be due to dynamic recombination of point defects during subsequent irradiation. Note, my complementary checking measurements up to fluences  $\sim 10^{18}$  ions/cm<sup>2</sup> showed that the saturation still keeps in the investigated fluence region.

#### 7.1.4. Conclusions

Fluence rate dependence of near-surface damage induced by 3.5 MeV He<sup>+</sup> analyzing beam was found in the low-fluence region. The higher the fluence rate, the higher damage level develops at the same fluence. For each ion beam density, the fluence dependence shows that in the applied fluence range ( $\leq 3.5 \times 10^{17}$  ions/cm<sup>2</sup>) there is an effective fluence region where the  $\chi_{\min}$  increases almost proportionally with fluence, whereas it remains almost unchanged (not approaching amorphisation) for higher fluences. It can be due to extremely dilute collision cascades formation in the near-surface region during He irradiation.

The defect generation rate can be significantly reduced if the irradiation is performed along channeling direction, i.e. parallel to the c-axis of hexagonal SiC.

The observations in the present study suggest that for BS/C analysis, it is worth keeping He<sup>+</sup> fluence rate as low as possible to ensure low damage levels in the near surface region. Accordingly, fluence rates of 5-8  $\mu\text{A}/\text{cm}^2$  and measurement fluences at or below  $5 \times 10^{16}$  ions/cm<sup>2</sup> (corresponding to 20  $\mu\text{C}$  total charge) have been applied in BS/C measurements performed in this thesis on ion-implanted SiC.

## 7.2. Investigation of aluminum implantation induced damage in the silicon and carbon sublattices of 6H-SiC

### 7.2.1. Introduction

As it was already mentioned, the fundamental understanding of the accumulation of damage induced by irradiation in both the Si and C sublattices of SiC is essential for advanced technological applications. To improve this knowledge, at first an appropriate experimental technique with satisfactorily good sensitivity and depth resolution has to be found for depth profiling. At second, theoretical calculations are also necessary to forecast the nature of damage accumulation processes and the efficiency of damage production caused by the implanted ions.

The displacement energy  $E_d$  is a useful and important parameter when damage production is calculated from the amount of energy deposition into the nuclear subsystem of the target. Calculations, based on binary collision approximation (BCA) can be realised by atomistic computer simulations e.g. by SRIM or Crystal-TRIM programs. In addition, molecular dynamics (MD) simulations can be performed, however in this case much higher computational power is required. For relatively low implantation fluences leading to damage levels well below the amorphization of SiC MD simulations predict a similar defect composition as assumed in BCA methods. Gao et al. have shown by MD simulations that in the low-fluence, low-temperature range ion irradiation into SiC leads to the formation and accumulation of single point defects like vacancies and interstitials [7.13]. Furthermore, Devanathan's simulations gave 35 eV and 21 eV for  $E_d$  of Si and C atoms in SiC [7.14].

If the irradiation-induced damage in SiC consists mainly of primary point defects than the shape of the depth distribution of disorder is expected to be similar than that derived from full-cascade Monte-Carlo computer simulations, e.g. the SRIM program. In SRIM an undamaged amorphous structure is considered for each individual ion during their subsequent irradiation, moreover, zero target temperature is assumed. Therefore, some discrepancy between measured and calculated damage levels is expected. The difference can be eliminated by the change of the displacement energy in the program. The result of the fit can be called as the 'effective' displacement energy. As SRIM is valid only for amorphous targets, a meaningful comparison between experiment and calculation require the implantation along random direction in order to avoid crystal channeling effects accompanied by damage reduction and ion range shift.

In this section BS/C using 3.5 MeV  $^4\text{He}^+$  ions along the  $\langle 0001 \rangle$  axial channeling direction of SiC was applied to measure depth profiles of implantation-induced defects both in the Si and C sublattices. Single crystal 6H-SiC samples were irradiated at room temperature along random direction with 200 keV  $\text{Al}^+$  ions at relatively low fluences in order to prevent the samples from amorphization. The shapes and heights of defect profiles extracted from BS/C measurements were compared to the results of full-cascade SRIM simulations and effective displacement energies for Si and C were determined.

### 7.2.2. Experimental details

N-type  $3.5^\circ$  off-axis single crystalline 6H-SiC wafer from CREE Res. Inc. was used. The Al implantation was performed in the Heavy Ion Cascade Implanter operating at the Central Research Institute for Physics in Budapest. This equipment is an electrostatic accelerator operating in the energy range 100-450 keV. The irradiation can be performed on a

large sample spot of maximum  $8 \times 8 \text{ mm}^2$  by moving the beam across the implanted area with an electronic beam steering system. The lateral homogeneity of fluence is about 1 %.

Four samples were implanted with 200 keV  $\text{Al}^+$  ions at room temperature. The irradiation was performed along random direction by tilting the samples  $7^\circ$  off normal. Implanted ion fluences were  $3.5 \times 10^{13}/\text{cm}^2$ ,  $7 \times 10^{13}/\text{cm}^2$ ,  $1.4 \times 10^{14}/\text{cm}^2$  and  $2.8 \times 10^{14}/\text{cm}^2$ . During implantation low ion fluence rate ( $5 \text{ nA}/\text{cm}^2$ ) was chosen to avoid beam-heating effect.

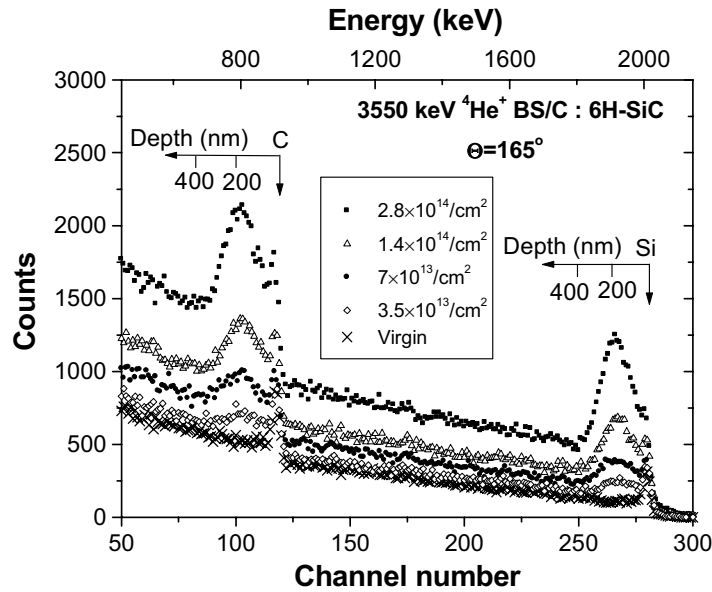
To investigate the damage induced by ion bombardment in the carbon and silicon sublattices, 3.5 MeV  $\text{He}^+$  BS/C experiments were performed along the  $\langle 0001 \rangle$  crystalline axis of 6H-SiC. The measurements were done in a scattering chamber containing a two-axis goniometer. Analyzing He ions were generated by the 5 MV Van de Graaff accelerator operating at the Central Research Institute for Physics in Budapest. The beam was collimated with two sets of four-sector slits to the dimensions of  $0.5 \times 0.5 \text{ mm}^2$ , while the beam divergence was kept below  $0.05^\circ$ . In the scattering chamber the vacuum was better than  $10^{-4} \text{ Pa}$ . To reduce the hydrocarbon deposition, liquid  $\text{N}_2$  cooled traps were used along the beam path and around the wall of the chamber. Backscattered  $\text{He}^+$  ions were detected using an ORTEC surface barrier detector mounted in Cornell geometry at scattering angle of  $165^\circ$ . Low current of 20 nA was used to reduce the damage created by the analysing beam itself during the measurements [7.15]. The beam current was measured by a transmission Faraday cup [7.16]. Damage curves were extracted from BS spectra using RBX code [7.9].

Swelling of Al implanted spots was measured by Alfa-step 100 profilometer (TENCOR Instruments).

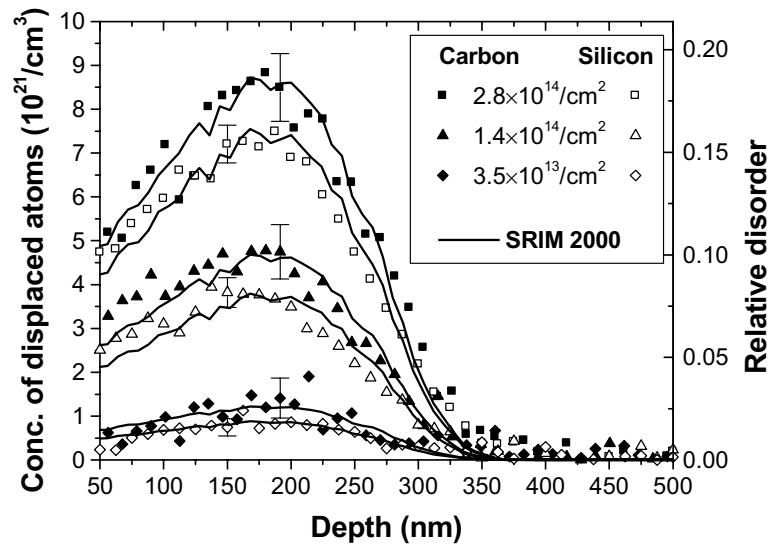
### 7.2.3. Results and discussion

Fig. 7.5 shows aligned 3.5 MeV  $^4\text{He}^+$  BS spectra of 6H-SiC samples implanted with different fluences. Due to the large non-Rutherford cross-section for C in this energy region, not only Si damage peak, but also that of C can be observed well on the spectra. Depth scale of Si and C damage were calculated using a crystalline SiC density of  $9.64 \times 10^{22} \text{ atom cm}^{-3}$ , i.e. the change in the density of the material due to ion implantation induced swelling was neglected. The validity of this assumption was confirmed by profilometric measurement across the border of the implanted area on the samples. The swelling, even at the highest  $\text{Al}^+$  fluence was below 10 nm. It means a maximum 3% discrepancy from the calculated depth scale.

Si and C damage profiles extracted from BS/C spectra are shown in Fig. 7.6. It can be seen that the shape of damage distributions is similar for Si and C, and its maximum locates around a depth of 180 nm, but the amplitudes are different. For each fluences the C damage level is higher than the Si damage level. Furthermore, the C/Si integrated total damage ratio decreases with fluence, being about 1.3 for the lowest, whereas 1.1 for the highest fluence applied. Similar decreasing tendency of the C/Si peak damage ratio has already been observed for 50 keV  $\text{He}^+$  and 2 MeV  $\text{Au}^+$  implantation at room temperature [7.17] and will be shown for 500 keV  $\text{N}^+$  implantation in Section 7.3.



**Figure 7.5** Aligned BS spectra of 6H-SiC samples implanted with 200 keV  $\text{Al}^+$  ions at room temperature. Channeling measurements were performed along the  $\langle 0001 \rangle$  crystalline axis. For comparison a virgin spectrum is also shown.



**Figure 7.6** Depth profiles of lattice damage induced by 200 keV  $\text{Al}^+$  implantation into 6H-SiC. Symbols: experimental data; Solid lines: SRIM 2000 simulations

To obtain the effective displacement energies full-cascade SRIM damage distributions were calculated.  $E_d(\text{C})$  and  $E_d(\text{Si})$  were varied in SRIM to find the best agreement between the integrals of measured and calculated damage distributions. The results of SRIM simulations are shown in Fig. 7.6, whereas the corresponding effective displacement energies are depicted in Fig. 7.7. As expected, the effective  $E_d(\text{C})$  values are always lower than  $E_d(\text{Si})$  for all fluences, and scatter between 14.8 eV and 19.3 eV for C and between 24.8 eV and 26.8 eV for Si, respectively. The changing ratio between C and Si disorder by different ion fluences can be explained by the fluence dependence of the effective displacement energies, which may be caused by deviations from the undamaged crystal.

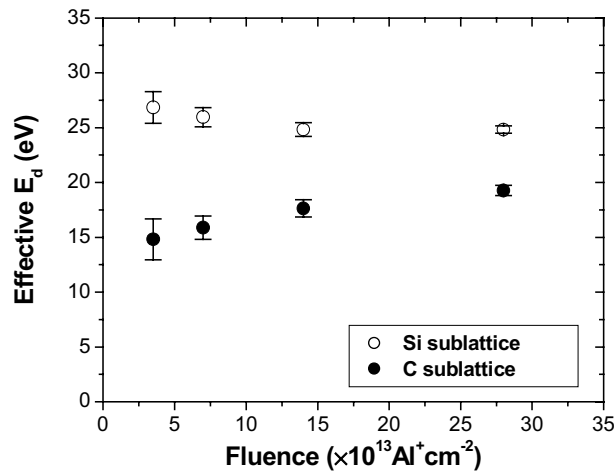


**Figure 7.7** Effective displacement energies for carbon and silicon sublattices of 6H-SiC. These values were determined by full-cascade SRIM simulations, finding the best agreement between calculated and measured damage curves.

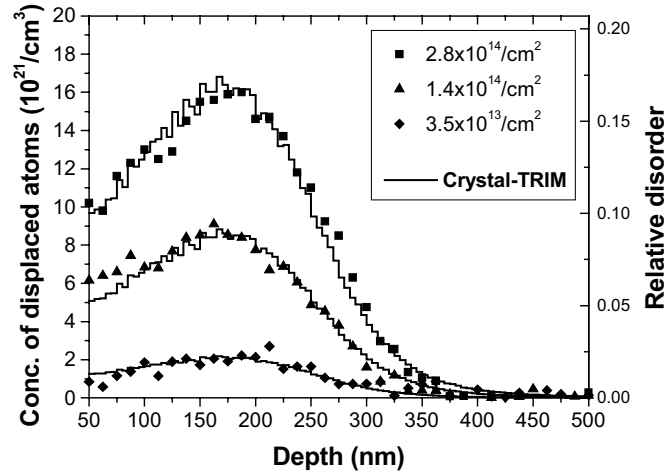


**Figure 7.8** Depth profiles of total lattice damage in C and Si sublattices together induced by 200 keV  $\text{Al}^+$  implantation into 6H-SiC to different fluences. Symbols: experimental data; Solid lines: Crystal-TRIM simulations.

Note in Fig. 7.6 that at greater depths SRIM simulated damage curves are slightly under the measured ones. This may be due to the fact, that SRIM neglects possible channeling effects that may occur in a crystalline material even if implanted particles are initially not channeled. In contrast, in Crystal-TRIM the crystalline structure of 6H-SiC can be taken into account. In order to check the possible role of channeling the total displacement profile – C and Si together – calculated by Crystal-TRIM program was compared to the total damage profile determined from BS/C experiments. In Fig. 7.8 Crystal-TRIM simulations are shown along with the measured data. A good agreement is found between Crystal-TRIM and BS/C at the tails of damage distributions. This comparison shows that some channeling at the tails of damage distributions should really occur. Otherwise the damage distributions calculated by SRIM and Crystal-TRIM are very similar, so that random implantation conditions can be considered and therefore channeling effects does not influence significantly the extracted effective displacement energies.

#### **7.2.4. Conclusions**

Relatively low damage levels (relative disorders  $< 0.2$ ) were created by  $\text{Al}^+$  ion implantation in 6H-SiC at room temperature. The depth distribution of accumulated damage in both Si and C sublattices were simultaneously measured by 3.5 MeV  $\text{He}^+$  BS/C analysis. For all applied ion fluences, higher damage levels were found in the carbon sublattice than in the silicon one. The C/Si integrated total damage ratio decreased with increasing fluence. Effective displacement energies were found to be between 24.8 eV and 26.8 eV for silicon and between 14.8 eV and 19.3 eV for carbon, respectively. These values are rather close to those resulted in electron irradiation experiments ( $E_d(\text{C}) = \sim 20$  eV, and  $E_d(\text{Si})$  is in the range 20-40 eV) and molecular dynamics calculations ( $E_d(\text{C}) = 20$  eV,  $E_d(\text{Si}) = 35$  eV), see section 2.5, and the references therein.

### 7.3. The influence of crystallographic orientation and ion fluence on damage accumulation in nitrogen implanted 6H-SiC

#### 7.3.1. Introduction

Recently, it has been shown that ion implantation into SiC causes deactivation of both donor (nitrogen) and acceptor (phosphorus) atoms accompanied by free charge carrier reduction [7.18, 7.19]. The deactivation is assumed through reaction with irradiation-induced point defects [7.19]. In addition, theoretical calculations [7.20] show that post-implantation annealing can lead to the formation of extremely stable dopant-defect related complexes and should explain the experimentally observed saturation of free carrier concentration [7.18].

If the implantation is performed along low index crystallographic directions, ion channeling occurs resulting in deeper dopant penetration and lower defect generation. However, the shape of the ion profiles obtained by channeling implantation is very sensitive to the implantation fluence due to cascade overlap and ion-defect scattering processes that lead to the dechanneling of projectiles initially moving within axial or planar channels. To date, only a few theoretical and experimental studies have been directed to the effect of channeling during ion implantation into 6H-SiC [7.13, 7.21-7.27]. In statistical computer simulations the damage accumulation related model parameters, like the probability for the recombination and/or clustering of defects,  $C_a$  [7.26], were usually utilized for helping to fit ion ranges [7.21-7.27] resulted by channeling implantation. A direct experimental observation of the depth distribution of implantation-induced disorder with satisfactory depth resolution for channeling implantation has not yet been reported. Furthermore, there is a lack of data concerning the rate of channeling to random disorder reduction in function of the implantation fluence. In this work I present a study on damage depth profiles induced by 500 keV N implants along the  $\langle 0001 \rangle$  axis and from different tilt angles into 6H-SiC. I use the Crystal-TRIM [7.26, 7.27] code for calculations and 3.5 MeV  $^4\text{He}^+$  ion backscattering analysis in combination with channeling as experimental technique.

For an adequate energy-depth conversion in the evaluation of damage distributions from BS/C spectra, the electronic stopping power of the analyzing He ions along the  $\langle 0001 \rangle$  axial channel of 6H-SiC is required. In this work, Crystal-TRIM simulations of 3.5 MeV  $^4\text{He}^+$  implantation and a simultaneous analysis of the BS/C spectra of the Si and C sublattices of slightly damaged SiC were used to determine the channeling to random ratio of the electronic stopping power for He.

#### 7.3.2. Experimental details

In this work n-type, double-side polished  $\langle 0001 \rangle$  on-axis single crystalline 6H-SiC samples from CREE Res. Inc. were used with a corresponding maximum nitrogen doping concentration  $\leq 10^{18} \text{ cm}^{-3}$ . All the experiments were performed with the 5 MV EG-2R Van de Graaff accelerator in Budapest.

Firstly the direction of the c-axis for each sample was determined by 1.5 MeV  $^4\text{He}^+$  angular scans. Then the crystal was tilted  $7^\circ$  off from the c-axis, and the azimuthal coordinates of the six equivalent (11-20) planes were also determined.

After performing angular scans the samples were implanted on virgin spots at room temperature by 500 keV  $\text{N}^+$  ions with different fluences in the range  $2.5 \times 10^{14} \text{ cm}^{-2} - 2 \times 10^{15} \text{ cm}^{-2}$ . To avoid any planar channeling the tilting plane was rotated by  $15^\circ$  from one of the (11-

20) planes. The choice of these conditions is based on an earlier channeling experiment which has shown that the equivalent (11-20) and (1-100) planar channels around the c-axis of 6H-SiC follow each other subsequently by  $30^\circ$  rotation steps [7.28]. The implantation for three different fluences ( $2.5 \times 10^{14}$ ,  $5 \times 10^{14}$ ,  $7.5 \times 10^{14} \text{ cm}^{-2}$ ) have been performed at tilt angles of  $0^\circ$ ,  $0.5^\circ$ ,  $1.2^\circ$ ,  $1.6^\circ$  and  $4^\circ$  with respect to the c-axis. One set of samples was implanted up to a fluence of  $9 \times 10^{14} \text{ N}^+ \text{ cm}^{-2}$  at tilts of  $0^\circ$ ,  $0.5^\circ$ ,  $1.6^\circ$  and  $4^\circ$  with respect to the c-axis. Another implantations were performed at higher fluences at tilts of  $0^\circ$  (with  $1.5 \times 10^{15}$ ,  $2 \times 10^{15}$ , and  $3 \times 10^{15} \text{ cm}^{-2}$ ) and  $4^\circ$  (with  $1.5 \times 10^{15}$ , and  $2 \times 10^{15} \text{ cm}^{-2}$ ), respectively. For the fluence of  $5 \times 10^{14} \text{ cm}^{-2}$ , one sample was implanted rotating continuously around the c-axis, while tilted off by  $7^\circ$  in order to avoid both planar and axial channeling to reach random implantation conditions. The transformation between the actual tilt and angular coordinates of the goniometer system and the crystallographic indices of 6H-SiC was performed by a software written by E. Szilágyi at the Research Institute for Particle and Nuclear Physics in Budapest. Low ion flux rate of  $\sim 2 \times 10^{12} \text{ cm}^{-2} \text{ s}^{-1}$  was chosen to avoid beam-heating effect during N implantation.

In order to get a homogeneous fluence distribution within the implanted spots, the N beam was collimated with two sets of four-sector slits to the dimensions of  $3 \times 3 \text{ mm}^2$ , while the maximum beam divergence was kept below  $\sim 0.15^\circ$ . After the implantation only a central part of  $0.6 \times 0.6 \text{ mm}^2$  of the implanted spot was analysed, and therefore an average divergence of  $\sim 0.1^\circ$  was considered for the nitrogen bombardment. For 500 keV N implantation, the angular half-width  $\Psi_{1/2}$  for  $\langle 0001 \rangle$  axial channeling in 6H-SiC is about  $1.7^\circ$  according to Equation 5.4 using a Debye temperature of 1120 K [7.29] (the corresponding root-mean-square atomic displacement is 0.005 nm [7.29]). Accordingly, with the above mentioned beam divergence, good channeling conditions can be achieved. The irradiation fluences were corrected in a similar manner by optical microscopy measurements, as it has been described for He implantation in Section 7.1.2.

For each ion fluence and irradiation tilt angle the local fluence at the damage peak in displacements per atom (dpa) was determined using full-cascade Crystal-TRIM simulations under the assumptions of 6H crystalline structure of the sample and a damage accumulation parameter of  $C_a = 1.0$ . In the calculation of electronic energy loss, the screening parameter of the ZBL electronic stopping  $C_\lambda = 1.02$ , and  $C_{el} = 1.2$  were applied (for the parameters  $C_a$ ,  $C_\lambda$ , and  $C_{el}$  see section 5.4 and later section 7.3.6, and also Ref. [7.26]). A target temperature of 300 K and a beam divergence of  $0.1^\circ$  were assumed in the simulations to reproduce the experimental conditions.

Following the nitrogen implantation, 3.55 MeV  $^4\text{He}^+$  BS/C measurements were carried out in standard conditions, similarly to that described in Section 7.2.2 for aluminum implanted samples (i.e. with the same vacuum, goniometer, collimator, and detection system). Low beam current of 15 nA and low measurement fluence of  $20 \mu\text{C}$  were used to reduce the damage created by the analysing He beam itself.

Damage depth distributions were evaluated from BS/C spectra using the RBX code. Non-Rutherford BS/C spectra of the carbon sublattice have been evaluated using Feng's tabulated scattering cross-section data [7.30], whereas slight deviations from Rutherford cross-section were considered for Si by means of Leung's enhanced cross-section database [7.31].

Isochronal annealing of the samples implanted with  $7.5 \times 10^{14} \text{ N}^+ \text{ cm}^{-2}$  was performed in a tube furnace in pure nitrogen atmosphere for 10 minutes subsequently at 400, 600, and



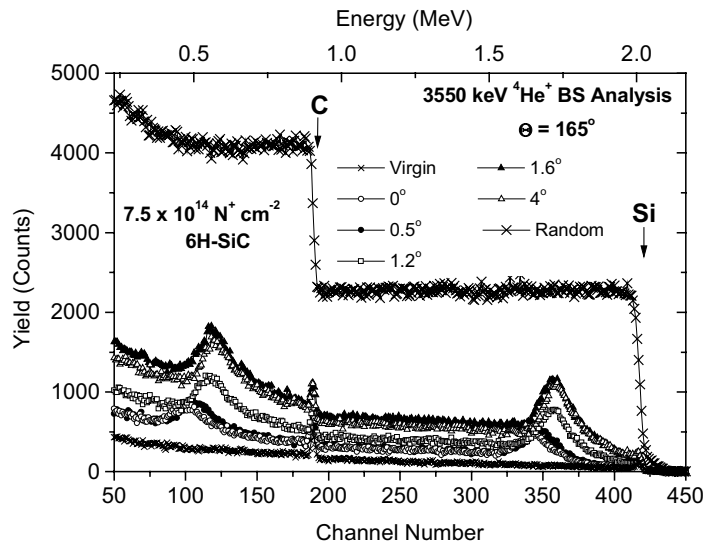
800 °C, respectively. After annealing BS/C measurements and the evaluation procedure were repeated on the samples.

## Results and discussion

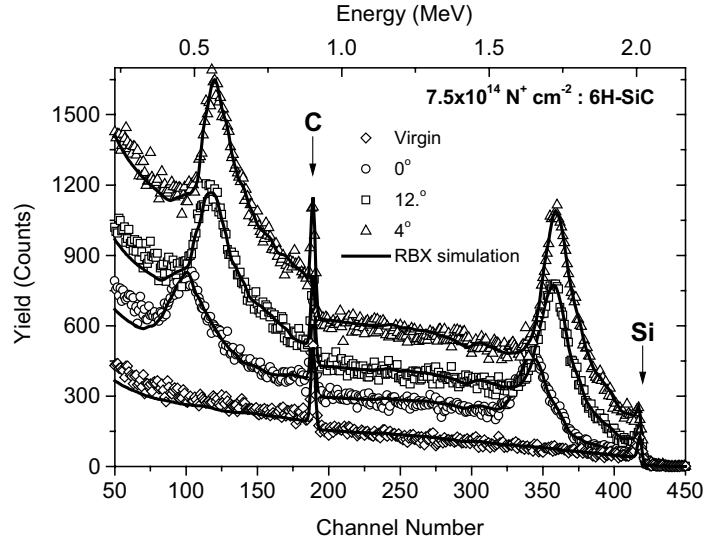
### 7.3.3 BS/C spectra

Fig. 7.9, as an example, shows BS/C spectra of 6H-SiC implanted with  $7.5 \times 10^{14} \text{ N}^+ \text{ cm}^{-2}$  at tilt angles of  $0^\circ$ ,  $0.5^\circ$ ,  $1.2^\circ$ ,  $1.6^\circ$ , and  $4^\circ$  with respect to the c-axis. For comparison, a channeling spectrum of a non-implanted (virgin) sample and a random spectrum are also shown. One can see that besides Si, the C sublattice is also readily resolved. The spectra show the difference between the depth distributions and levels of disorder induced by the nitrogen ions implanted from different directions. The spectrum of the  $0^\circ$  and  $0.5^\circ$  implant between channels 380-410 overlap with the virgin one, indicating a very low disorder level in the surface region. For  $1.2^\circ$ , there is a gradual increase in the yield from the surface to the damage peak, while for  $1.6^\circ$  and  $4^\circ$  a significant disorder can be observed already at the surface. In addition a remarkable shift of the disorder peak toward higher energies (i.e. channel numbers) can be observed from  $0^\circ$  to  $4^\circ$ , respectively.

To extract disorder depth distributions from the BS/C spectra RBX simulations were performed assuming histogram-type damage structures with a sublayer thickness of 50 nm. A constant disorder concentration was considered within one sublayer. Fig. 7.10 shows the virgin,  $0^\circ$ ,  $1.2^\circ$ , and  $4^\circ$  implanted aligned spectra from Fig. 7.9 along with the corresponding RBX simulations. Both the disorder peaks and the dechanneling yields behind the damaged regions can be well simulated.



**Figure 7.9** 3.55 MeV  $^4\text{He}^+$  BS/C spectra of 6H-SiC, implanted with  $5 \times 10^{14} \text{ N}^+/\text{cm}^2$  from  $0^\circ$ ,  $0.5^\circ$ ,  $1.2^\circ$ ,  $1.6^\circ$ , and  $4^\circ$  tilts with respect to the c-axis. Virgin and random spectra are also shown for comparison.



**Figure 7.10** 3.55 MeV  $^4\text{He}^+$  BS/C spectra of 6H-SiC, implanted with  $7.5 \times 10^{14} \text{ N}^+/\text{cm}^2$  from  $0^\circ$ ,  $1.2^\circ$ , and  $4^\circ$  tilts with respect to the c-axis. A virgin spectrum is also shown for comparison. Solid lines are the corresponding RBX simulations.

In the RBX program:

- (i) Single point defects and their clusters were considered as direct scattering centers. The dechanneling contribution of these defects contains dechanneling due to direct scattering events according to Equation 6.8, and dechanneling from multiple scattering events.
- (ii) If necessary, besides the dechanneling contribution for (i) an excess dechanneling contribution was introduced. This contribution was considered as an extra factor of the product in the right-hand side of Equation 6.8, with a constant probability of dechanneling per unit depth,  $dP_D/dx$ . This contribution can originate from slightly displaced atoms, relaxed under lattice strain (introduced by primary point defects) and/or from defect complexes and extended defects with different  $\sigma_{Di}$  with respect to the analyzing He ions. Local strain can also be formed at the boundaries of larger amorphous clusters embedded in the residual crystalline matrix, because of the lower density of amorphous SiC as compared to the crystalline phase. Hereafter the dechanneling contribution, due to this term is called *strain*.

The parameters used in RBX simulations for different fluences and implantation tilt angles are shown in Table 7.1. Strain parameters are relative values of the excess dechanneling probabilities  $dP_D/dx$ , normalized to the highest value found. The relative disorders,  $n_D$ , at the Si and C damage peaks are also shown. One conclusion is that for  $n_D < \sim 0.2$ , regardless of the direction of implantation, the measured BS/C spectra can be well simulated assuming the presence of single point defects and their small clusters. On the other hand, for higher disorder levels the strain term has to be introduced with increasing value as  $n_D$  increases. Fig. 7.11 shows the extracted strain parameters as a function of peak disorder. The introduction rate for strain (i.e. the slope of the strain-disorder curve) is high and almost constant for  $\sim 0.2 < n_D < \sim 0.45$  and becomes significantly lower for strongly disordered samples up to the amorphization threshold. The second stage suggests the presence of strain relaxation processes that can be associated with the overlap between strain fields in damaged

zones. A possible way of strain relaxation in implantation-damaged SiC layers is the structural transformation, i.e. the amorphization of the material, accompanied by volume expansion toward the sample surface [7.32]. This expansion appears as surface swelling, a step at the boundary of unirradiated/irradiated areas, and can be detected by profilometric measurements. As Table 7.1 shows considerable surface swelling was observed by profilometric measurements for samples with peak disorder levels  $n_D > 0.9$ , i.e. close to amorphization. At and below this relative peak disorder level no significant swelling was observed for any implantation fluence and direction.

Fluence ( $10^{14} \text{ cm}^{-2}$ )	Tilt angle (degree)	Relative disorder at damage peak		Stopping correction $\alpha$	Strain parameter	Swelling (nm)
		Si	C			
2.5	0	0.04	0.063	0.8	-	-
	0.5	0.065	0.09	0.8	-	-
	1.2	0.115	0.14	1	-	-
	4	0.15	0.15	1	-	-
5	0	0.093	0.137	0.8	-	-
	0.5	0.105	0.14	0.8	-	-
	1.2	0.16	0.18	1	-	-
	1.6	0.2	0.235	1	-	-
	4	0.23	0.23	1	-	-
7.5	0	0.145	0.19	0.8	-	-
	0.5	0.175	0.2	0.8	-	-
	1.2	0.31	0.29	1	0.18	-
	1.6	0.45	0.45	1	0.71	-
	4	0.44	0.42	1	0.53	-
9	0	0.25	0.25	0.8	0.18	-
	0.5	0.34	0.34	0.8	0.41	-
	1.6	0.45	0.46	1	0.65	-
	4	0.48	0.43	1	0.59	-
15	0	0.7	0.78	0.9	0.59	-
	4	0.98	0.98	0.8	0.94	50
20	0	0.96	0.95	0.8	0.94	40
	4	1	1	0.8	0.94	150
30	0	1	1	0.8	1	60

**Table 7.1** Parameters used in the RBX evaluation of 3.55 MeV  $^4\text{He}^+$  BS/C spectra of 500 keV  $\text{N}^+$  implanted 6H-SiC samples along with surface swellings detected by profilometric measurements.

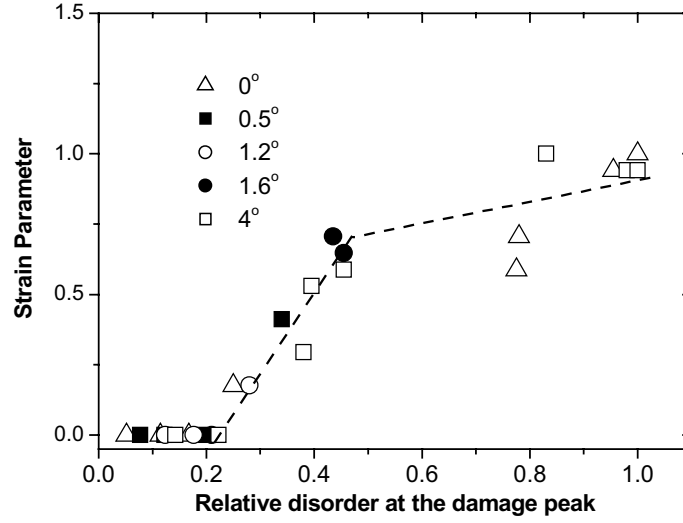


**Fig. 7.11** Strain parameters as a function of the relative disorder at the damage peak induced by 500 keV N implantation with different fluences and tilts with respect to the *c*-axis of 6H-SiC. Strain data are determined from excess dechanneling contributions in the RBX simulated spectra and are normalized to the highest value found.

#### 7.3.4 Electronic stopping power for channeled high-energy light ions in SiC

When using BS/C techniques to investigate the depth distribution of implantation-induced disorder in crystalline targets, besides satisfactory energy resolution, accurate knowledge of electronic stopping powers  $S_e$  of the analyzing ions both along random and channeling directions is required for an adequate energy-depth conversion. Nevertheless, there is a lack in bibliography concerning  $S_e$  for high-energy He ions in SiC along the  $\langle 0001 \rangle$  direction ( $S_e^{\langle 0001 \rangle}$ ), the commonly used channeling direction in BS/C experiments.

A recent study [7.33] has shown the validity of Bragg's rule for the random  $S_e^{ZBL}$  of helium ions in SiC within a wide energy range of 0.5–2.4 MeV. The agreement between experimental stopping data [7.33] and Bragg's rule gives no evidence for strong Si–C chemical bonding effects that can limit the additivity rule in multielemental targets especially around the stopping peak where the maximum ion-target interaction occurs ( $\sim 0.5$  MeV for He in SiC).

As a most straightforward approximation of Equation 5.8, particles penetrating a crystalline target along channeling direction are considered to lose electronic energy proportional to the random  $S_e^{ZBL}$  rate:

$$S_e^{channel}(E) = \alpha S_e^{ZBL}(E) \quad (7.1)$$

where  $\alpha$  is constant and does not depend on energy. For 3.5 MeV  $^4\text{He}^+$  ions in SiC the energy dependence of  $S_e^{ZBL}$  is very weak (see. Fig. 7.12) therefore Equation 7.1 can be a reasonable relation. Equation 7.1 is generally used in the RBX program in the evaluation of BS/C spectra, when the analyzing He ions penetrate in the  $\langle 0001 \rangle$  direction, i.e. before they are backscattered from Si or C target atoms, or dechanneled by crystal defects.

To date, there are only available experimental data on proton stopping powers along the  $\langle 0001 \rangle$  direction of 6H-SiC. A study of Kokkoris et al. [7.34] on 1.7–2.5 MeV energy protons resulted a channeling to random  $S_e^{\langle 0001 \rangle}/S_e^{ZBL}$  ratio of  $\alpha = \sim 0.8$  in 6H-SiC. They found  $\alpha$  to be energy independent in the studied range in agreement with the assumption in Equation 7.1.

Based on Kokkoris's work, I have reproduced the  $\alpha = 0.8$  value for 2 MeV protons with Crystal-TRIM by varying the  $C_{el}$  parameter in Equation 5.8. I have found the best agreement with the experimental results at  $C_{el} = 1.25$ . This  $C_{el}$  value was applied to predict  $S_e^{<0001>}$  for 3.5 MeV  $^4\text{He}^+$  ions. I also performed Crystal-TRIM simulations for 3.5 MeV energy protons for comparison. The results for  $S_e^{<0001>}$  and  $S_e^{ZBL}$  as functions of the penetration depth for  $^1\text{H}^+$  and  $^4\text{He}^+$  ions in undamaged 6H-SiC are shown in Fig 7.12. All the stopping powers are nearly constant between 0–1000 nm, which is the depth range of damage distributions induced by 500 keV  $\text{N}^+$  implantation, and thus the information depth of the BS/C analysis. Integrating the simulated stopping powers in this depth region the ratios  $\alpha = (S_e^{<0001>})_{\text{average}} / (S_e^{ZBL})_{\text{average}}$  are about 0.8 both for H and He, respectively.

In the RBX evaluation procedure, the  $\alpha$  stopping correction was introduced in the energy-depth conversion. The resulted  $\alpha$  values are indicated in Table 7.1.

The validity of  $\alpha = 0.8$  for He is reflected in the extracted damage depth distributions in the Si and C sublattices of SiC. Fig 7.13a shows the RBX damage profiles for Si and C in 6H-SiC after  $5 \times 10^{14} \text{ cm}^{-2}$  N implantation along the  $<0001>$  direction. Here  $\alpha = 1.0$  (equivalent to  $S_e^{ZBL}$ ) was used for the incoming channelled He ions in the RBX evaluation. Clearly, the damage profile for carbon is broader and its peak located deeper as compared to the silicon one.

In contrast, in Fig 7.13b using  $\alpha = 0.8$  in RBX the Si and C damage peaks both located at a depth of about 760 nm. Furthermore, the Si peak is shifted by  $\sim 50$  nm, and the C peak is by  $\sim 25$  nm deeper as compared to that of in Fig 7.13a. As it has been shown by Simionescu et al., the energy deposition of the sub-cascades takes place at the position where the collision between the ion and the PKA occurs [7.35]. In accordance, the extension of a sub-cascade initiated by the PKA is small compared to the ion range. Full-cascade Crystal-TRIM simulations, following the motion of recoiled target atoms in sub-cascades, also do not predict any difference in the Si and C defect distributions. Therefore, cascade kinetics *per se* seems to be unable to account for the significant asymmetry in the Si and C defect distributions in Fig 7.13a.

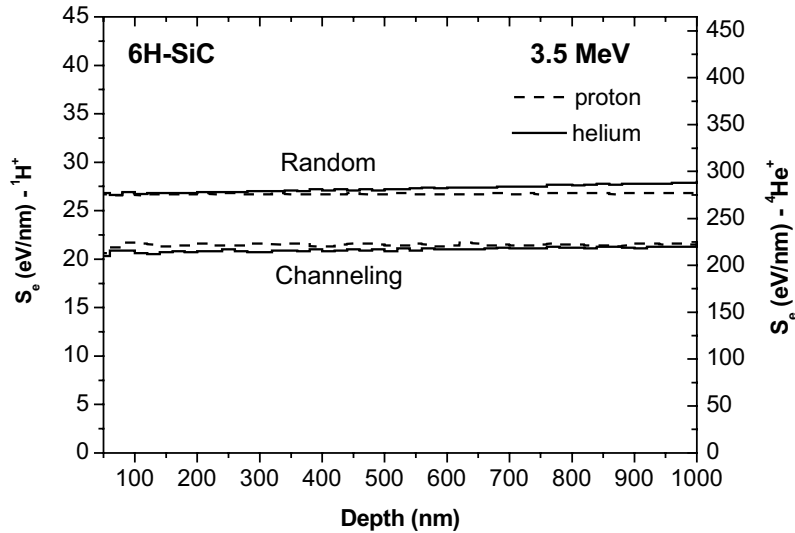


**Figure 7.12** Crystal-TRIM simulations of the electronic energy loss of 3.5 MeV H and He in 6H-SiC as a function of depth both along random and channeling direction with respect to the  $c$ -axis. Note the different scales for H and He.

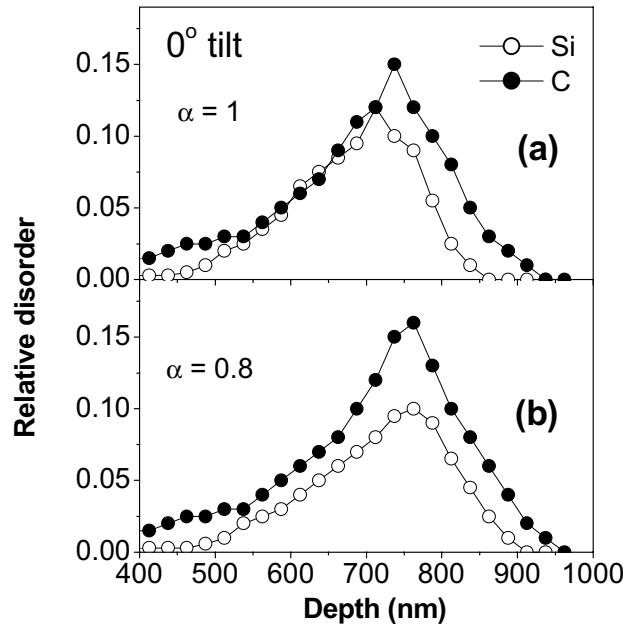


**Figure 7.13** The relative disorder as a function of depth in both the Si and C sublattices of 6H-SiC, implanted with  $5 \times 10^{14} \text{ N}^+ \text{ cm}^{-2}$  along the  $c$ -axis, as extracted from the RBX evaluation of 3.55 MeV  $^4\text{He}^+$  BS/C spectra. The energy-depth conversion in RBX was performed assuming a channeling to random electronic stopping correction  $\alpha$  of (a) 1.0, and (b) 0.8 for the analyzing He ions, respectively.

Furthermore, at room temperature the migration of defects is unlikely due to extremely low self-diffusion coefficients [7.36] as well as previously reported annealing temperatures of vacancies and interstitials in irradiated SiC [7.37, 7.38]. Taking into account the previous considerations I conclude that the peak shift between Si and C in Fig 7.13a is not justifiable by the features of the damage formation itself, but is due to the improper use of the ZBL helium stopping power along the  $\langle 0001 \rangle$  axis of SiC in the RBX evaluation. The same effect was observed for tilt =  $0.5^\circ$ , too. Nevertheless, such a significant deviation from  $\alpha = 1$  was not found for the  $1.2^\circ$ ,  $1.6^\circ$ , and  $4^\circ$  tilt implants (Table 7.1). This can be explained by the fact that for higher tilts the crystal is considerably disordered already at the surface, while for  $0^\circ$  and  $0.5^\circ$  it remains almost perfect in a depth region of 0-400 nm (Fig. 7.9), and in this case  $S_e$  for channeled helium ions is more close to the ideal  $S_e^{\langle 0001 \rangle}$  stopping power. Nevertheless, for highly disordered samples, a stopping correction  $\alpha$  also has to be used (Table 7.1) to get the same damage peak positions for Si and C. It can be explained by the observed volume expansion (Table 7.1) that leads to the reduction of atomic density and average electron density in the material. This process is reflected in the lower electronic stopping powers as compared to that in crystalline SiC.

### 7.3.5 Disorder profiles

Fig. 7.14 shows RBX profiles of the relative disorder in SiC using the parameters in Table 7.1 along with the results of full-cascade Crystal-TRIM simulations. Here the total amount of disorder together in the Si and C sublattices is normalized to the total random yield of SiC. The resulted damage levels are the relative disorders averaged over the Si and C sublattices and hereafter will be called as averaged relative disorders.

The essential difference between channeling and random implantation is that – for a given fluence – the defect peak is shifted significantly deeper for on-axis irradiation. Increasing the tilt from  $0^\circ$ , the defect peak moves toward the surface and approaches the position of the random peak that is at about 560 nm. No further move can be observed at tilt angles  $\geq 1.2^\circ$ , though the damage for  $1.2^\circ$  tilt is conspicuously less than for  $1.6^\circ$ . The inset in Fig 7.14 shows RBX damage profile for a sample implanted with  $5 \times 10^{14} \text{ cm}^{-2}$  while rotating around the c-axis and tilted off by  $7^\circ$  in order to avoid any channeling effect. The resulted profile is very similar to the corresponding  $4^\circ$  tilt one, confirming that  $4^\circ$  can be considered as the case of random irradiation. This is consistent with the calculation based on Equation 5.4, giving a value of  $1.7^\circ$  as the critical angle for channeling ( $\Psi_{1/2}$ ) for 500 keV N ions along the  $\langle 0001 \rangle$  axis of SiC.

The most remarkable effect in Fig. 7.14 is that much less damage was created by on-axis implantation than by random irradiation for each fluence value. The fall of total damage and the damage peak shift in case of channeling implantation is due to the fact that the distribution of impact parameters is shifted toward higher values for channeled ions and a larger portion of the kinetic energy is dissipated in electronic stopping processes. As channeled ions slow down nuclear collision events takes place with increasing probability – giving rise to defect formation in deeper region.

Nevertheless, for a given implantation tilt angle, there is also a change in the shape of the damage depth profile as the fluence increases. As Fig 7.14 shows for channeling implantation the damage peak gradually shifts toward the surface with increasing fluence. It can be clearly seen for  $0^\circ$  and  $0.5^\circ$  tilts, implying that in this fluence region the trajectory of a channeled nitrogen ion is strongly affected by the pre-damage induced by the previous bombardment, i.e. the collision cascade zones caused by consecutive ion impacts overlap. These conditions can give rise to interactions between relaxed and unrelaxed damage zones generated at the same target position and therefore secondary damaging processes can occur besides simple accumulation of primarily generated point defects.

### 7.3.6 Computer simulation of damage accumulation

Solid lines in Fig. 7.14 represent the results of atomistic computer simulations. In Crystal-TRIM threshold energies for single atomic displacements  $E_d$  of 20 eV and 30 eV for C and Si were used for all implantation tilt angles and fluences. This assumption is based on the results of sub-threshold electron-irradiation experiments, as described in Section 2.5. In the simulation of damage build-up only one semi empirical parameter,  $C_a$  has been varied which includes any deviation from the used  $E_d$ , recombination and clustering as well as the scattering efficiency of the defects with respect to the implanted nitrogen ions. The probability  $p(x)$  that a  $\text{N}^+$  ion is randomly scattered by a defect at depth  $x$  is given by:

$$p(x) = C_a \frac{N_d(x)}{N_{\text{SiC}}} \quad (8.2)$$

where  $N_d(x)$  is the number of primary atomic displacements and  $N_{\text{SiC}}$  is the atomic density of crystalline SiC.

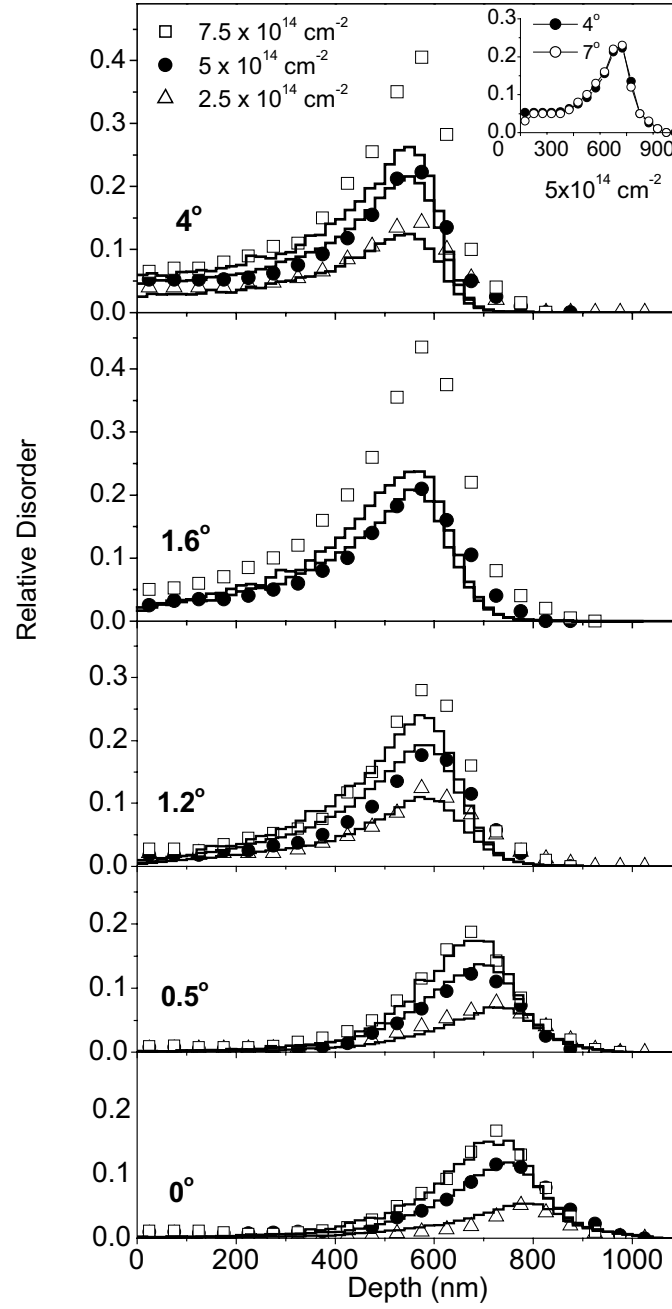


**Fig. 7.14** Depth distribution of averaged relative disorders in 6H-SiC implanted with different fluences of 500 keV N at different tilts with respect to the *c*-axis. Symbols: RBX evaluation, Solid lines: Crystal-TRIM simulation.

In Fig. 7.14  $C_a$  values of 2.7, 2.25 and 1.8 were used for the fluences of  $2.5 \times 10^{14}$ ,  $5 \times 10^{14}$  and  $7.5 \times 10^{14} \text{ N}^+ \text{ cm}^{-2}$ , respectively. Crystal-TRIM well reproduces the shapes and heights of the measured damage distributions at each implantation tilt angle for the lower fluences. In this case the disorder level at any depth is proportional to the number of primary atomic displacements (i.e. vacancies) in the same manner. In contrast, for the highest fluence at  $1.6^\circ$  and  $4^\circ$  tilt the measured disorder level around the damage peak is much higher than the simulated one. Since the effect appears only for  $n_D > \sim 0.2$  it can be attributed to the start of amorphization processes and the formation of larger defect complexes and amorphous



domains followed by the accumulation of strain and volume expansion as confirmed by BS/C and profilometric measurements.

The level of pre-damage has to exceed a critical threshold to start cascade overlap and enhanced dechanneling processes. Below this threshold the zero-fluence approximation is valid when ion ranges and damage shapes do not depend on fluence. An extrapolation toward the zero-fluence region for  $0^\circ$  tilt 500 keV  $N^+$  implantation has been performed by Crystal-TRIM as shown in Fig. 7.15. A threshold damage concentration of  $\sim 0.5\%$  with corresponding fluence of  $\sim 5 \times 10^{13} N^+/cm^2$  was found to reach zero-fluence conditions. This concentration is beyond the detection limit for 3.55 MeV BS/C analysis and therefore the experimental check is not available for fluences below  $\sim 10^{14} cm^{-2}$ . Note that the same order of threshold damage concentration being in the range 0.1–1 % can be estimated in Ref 7.21 for 1.5 MeV  $Al^+$  implantation into 6H-SiC. In that work the distortion of the ion distribution as a function of the fluence was followed by secondary ion mass spectroscopy (SIMS).

The variation in the shape of the damage curves in Fig. 7.14 reveals that the collision cascades have high probability to overlap in the investigated fluence range for 500 keV  $N$  ions. The  $C_d > 1$  values used in our Crystal-TRIM simulations also suggest that cascade-induced processes can dominate damage build-up against defect recombination at room temperature.

Similar effect was found in 6H-SiC after 2 MeV  $Au^{2+}$  [7.39] and 0.9 MeV  $Ge^+$  [7.40] implantation along random direction at 300 K, where  $\sim 6.2$  and  $\sim 4$  times higher disorder levels were observed by ion-channeling measurements as compared to the concentration of displacements per atoms predicted by SRIM simulations. In all these experiments the implanted fluences were far above the threshold for zero-fluence approximation, giving rise to cascade overlap during damage build-up processes.

My experimental results are in qualitative agreement with molecular dynamics simulations [7.41] that have been performed to describe the topological features and cascade overlap processes in implantation-induced displacement cascades. Calculations for 3C-SiC show the nucleation of small clusters from single point defects already at low implantation fluence. Increasing fluence, the concentration of these clusters increases and should induce considerable strain in the lattice. During continued cascade overlap, the small clusters coalesce and grow, due to lattice strain, to form larger clusters and amorphous domains. This amorphization process appears to be consistent with the direct-impact, defect-stimulated (D-I/D-S) model described in Appendix 2. In the next section the accumulation of implantation-induced disorder will be described on the basis of the D-I/D-S model.

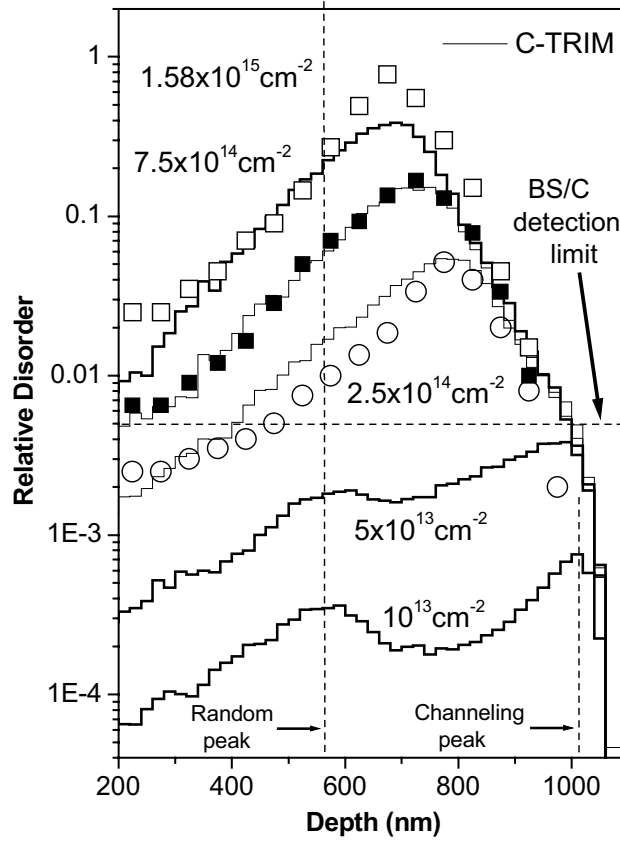


**Figure 7.15** The influence of ion fluence on the depth distribution of averaged relative disorder in 6H-SiC implanted with 500 keV N along the c-axis. Symbols: RBX evaluation of BS/C spectra, Solid lines: Crystal-TRIM simulation.

### 7.3.7 Disorder accumulation on the basis of the direct-impact, defect-stimulated amorphization model

The disorder accumulation on both the Si and C sublattices at the damage peak determined from BS/C experiments is shown in Fig. 7.16 as a function of the fluence in terms of displacements per atom,  $dpa$ . The  $dpa$  scale was determined from peak damage levels in Crystal-TRIM simulations using a damage accumulation factor of  $C_a = 1$ . Data for different implantation tilt angles are marked with different symbols. Complete amorphization corresponds to a relative disorder of 1.0. The solid lines are fits of the D-I/D-S disorder accumulation model (Equation A2.1), and the fit parameters are summarized in Table 7.2 along with other data taken from the literature for comparison.

In the low fluence and low damage region in Fig. 7.16 the disorder rate,  $dS/dD$  is sublinear and decreases with fluence. Since the amount of disorder in the zero-fluence region is expected to increase proportionally with fluence [7.42, 7.43], the reduced disorder rate in Fig. 7.16 is due to the higher probability of recombination of point defects and formation of simple clusters from interacting collision cascades. The imprint of cascade overlap is in agreement with the results of Crystal-TRIM simulations (See Fig. 7.15). The value of  $S_d^*$  is higher for C than for Si in accordance with the higher defect production rate for C due to its

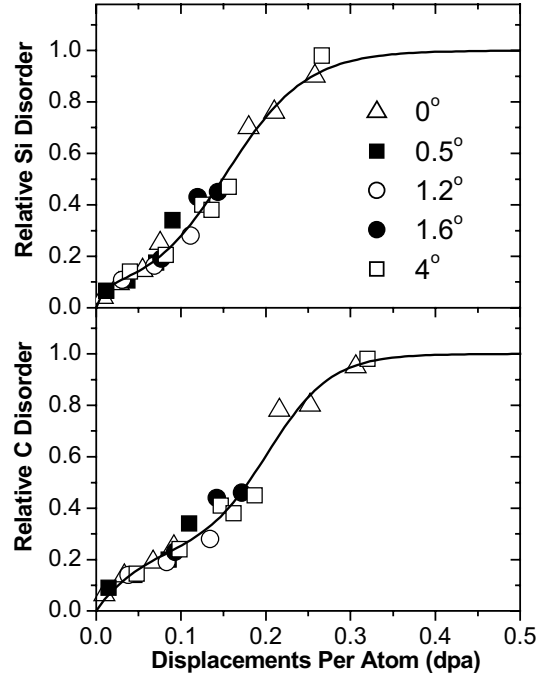


**Figure 7.16** The relative disorder at the damage peak as a function of displacements per atom in both the Si and C sublattices of 6H-SiC implanted with 500 keV N ions with different fluences at different tilt angles with respect to the c-axis. Symbols: experimental data, Solid lines: best fits of the direct-impact, defect-stimulated amorphization model.

Ion	Energy (MeV)	$\sigma_a$ (dpa <sup>-1</sup> )		$\sigma_s$ (dpa <sup>-1</sup> )		$S_d^*$		$B$ (dpa <sup>-1</sup> )	
		Si	C	Si	C	Si	C	Si	C
N <sup>+</sup>	0.5	0.7	0.1	25.6	20.7	0.085	0.25	100	17
Al <sub>2</sub> <sup>+</sup>	1.1	2	2	26.3	26.4	0.01	0.06	100	100

**Table 7.2** Parameters used in the best fits of the direct-impact, defect-stimulated amorphization model of SiC. Data for Al<sub>2</sub><sup>+</sup> taken from Ref. [7.44] are also shown for comparison.

lower displacement energy [7.14]. From the model fits, the results indicate that  $S_d$  is the primary contributor to the total disorder for  $n_D < 0.2$ . Increasing the fluence further, the disordering rate is enhanced, and according to the model fit,  $f_a$  is the dominant contributor to the total disorder for  $0.2 < n_D < 1.0$ . The significantly higher values for  $\sigma_s$  than for  $\sigma_a$  (Table 7.2) consistent with previous observations [7.44] and indicate that defect-stimulated amorphization is the primary mechanism leading to the amorphization of SiC.

As Table 7.2 shows, the  $\sigma_a$  parameter for 500 keV N is considerably lower than that observed for 1.1 MeV Al<sub>2</sub><sup>+</sup> ions [7.44] implanted at 300 K. This is in agreement with the fact that, due to its higher atomic number, the Al ion-induced collision cascades are denser as compared to the case of N implantation performed at nearly the same energy.

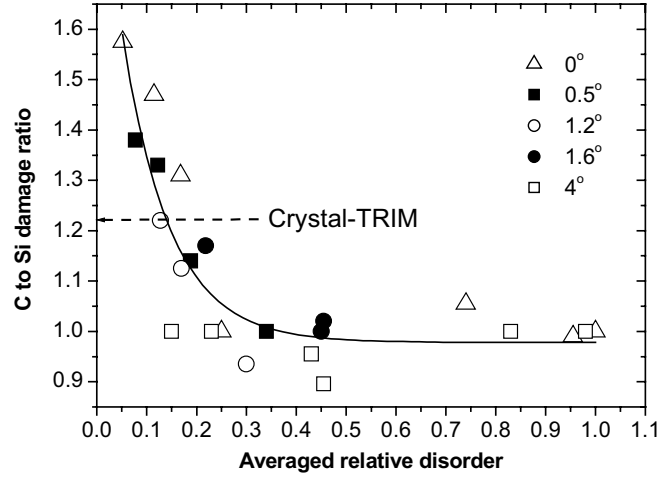


**Figure 7.17** C to Si damage ratios at the damage peak in function of the averaged relative disorder in 6H-SiC implanted with 500 keV N ions of different fluences at different tilts with respect to the c-axis. The prediction shown by Crystal-TRIM is labeled.

Fig. 7.17 shows C to Si disorder ratios at the damage peak in function of the averaged relative disorder. The data are summarized for different implantation tilt angles. As the transition occurs in damage build-up from the  $S_d$  dominated stage to the  $f_a$  dominated one, the amount of excess disorder on the C sublattice strongly decreases, and at  $n_D \approx 0.3$  saturates to 1.0. At this highly disordered stage the probability to bring either Si or C atoms to the amorphous state is higher than in a perfect lattice and the difference in the displacement energies of Si and C plays no longer role in damage formation. Consequently, higher  $C_a$  values are required in Crystal-TRIM to reconstruct disorder levels at the damage peak when  $n_D$  exceeds 0.2. The arrow in Fig. 7.17 shows the C to Si disorder ratio at the damage peak calculated by Crystal-TRIM, yielding a value of 1.22 for all fluences and crystalline orientations assuming displacement energies of 20 and 30 eV for C and Si, respectively. Since the arrow in Fig. 7.17 intersects the middle of the vertical range filled by experimental data it can be concluded that the orientation dependence of the *averaged lattice disorder* profile at a given fluence can be reconstructed using a fixed parameter set of  $E_d$  and  $C_a$  (see Fig. 7.14). However, the *separated Si and C sublattice disorders* can be overestimated or underestimated, according to the variation of the experimental C to Si disorder ratios.

### 7.3.8 Reducing the damage by channeling and annealing

Fig 7.18 shows random to channeling ratios of the integrated total amount of disorder as a function of the fluence. A value of  $\sim 7$  is predicted by Crystal-TRIM for the ideal case, i.e. for zero-fluence conditions. As BS/C experiments show, the ratio drops down to about 4 for  $2.5 \times 10^{14} \text{ N}^+/\text{cm}^2$  and further to 2 for  $5 \times 10^{14} \text{ N}^+/\text{cm}^2$ , then decreases slowly to  $\sim 1.7$  up to the threshold fluence for amorphization ( $1.5 \times 10^{15} \text{ N}^+/\text{cm}^2$  for  $4^\circ$  tilt). There is an anomalous increase to  $\sim 2.7$  at  $7.5 \times 10^{14} \text{ N}^+/\text{cm}^2$ . The reason for this can be seen in Fig. 7.14: this is the only fluence investigated where the dominant contributor to the total disorder is different for  $0^\circ$  and  $4^\circ$  tilt, respectively. It seems that effective disorder reduction by channeling implantation can be achieved at low disorder levels, when the accumulation of damage is suggested to be dominated by single point defects. At higher disorder levels the efficiency weakly depends on the fluence.

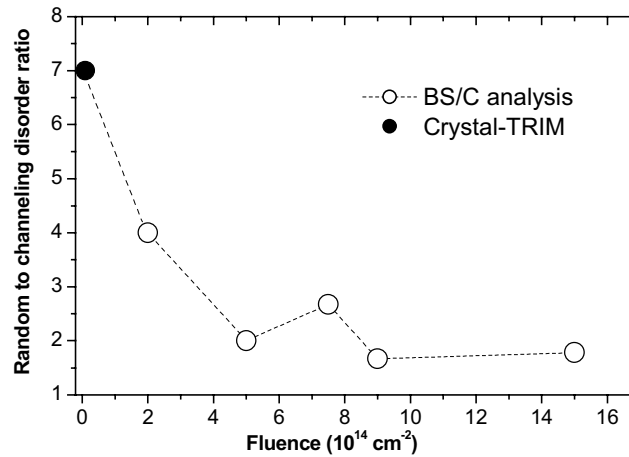


**Figure 7.18** Random to channeling ratios of the integrated disorders as a function of the fluence in 6H-SiC implanted with 500 keV N ions. Open symbols: results of BS/C analysis. Solid symbol: prediction for zero-fluence conditions calculated by Crystal-TRIM.

After nitrogen implantation, isochronal annealing was carried out (10 min) sequentially at temperatures 400, 600, and 800 °C on the sample implanted with  $7.5 \times 10^{14} \text{ N}^+/\text{cm}^2$ . Profiles of averaged relative disorder extracted from RBX evaluations for the as-implanted sample and for the same sample subsequently annealed at 400 °C are shown in Fig. 7.19 for different implantation tilts along with Crystal-TRIM simulations performed with  $C_a = 2.25$ . For tilts 0°, 0.5°, and 1.2° almost no change can be observed in the disorder profiles after annealing, whereas significant recovery occurs at the disorder peak for 1.6° and 4° tilts, respectively. The recovery appears in depth regions where  $n_D$  exceeds  $\sim 0.2$ , the threshold for prevailed amorphization and strain formation, as it is predicted by the D-I/D-S model. All annealing profiles are in good agreement with Crystal-TRIM simulations suggesting that for 1.6° and 4° tilt in Fig. 7.19 both the formation and the recovery of the excess disorder is induced by different mechanisms as compared to the rest still present after 400 °C annealing.

A possible reason for the different annealing behavior is that at 400 °C the presence of strain around the damaged zone could enhance disorder recovery together with thermal activation. The fact that mainly the disorder fraction  $n_D > 0.2$  can be recovered suggests that the amorphous zones of the sample can be re-ordered already at 400 °C, whereas single point defects and defect clusters in weakly damaged zones still survive. However, a partial annealing of point defects cannot be either excluded. My results are in agreement with a broad annealing step between 280-430 °C observed after room temperature implantation of  $\text{B}^+$  [7.45] and  $\text{N}^+$  [7.46] into SiC. The analysis of those partially damaged layers by sub-gap optical spectroscopy [7.45] has shown that already after annealing at temperatures up to 400 °C the amount of amorphous SiC decreases remarkably. It was also shown that above 530 °C the annealing proceeds in the same manner as the annealing of weakly damaged layers [7.46]. This feature is also consistent with my experiments.

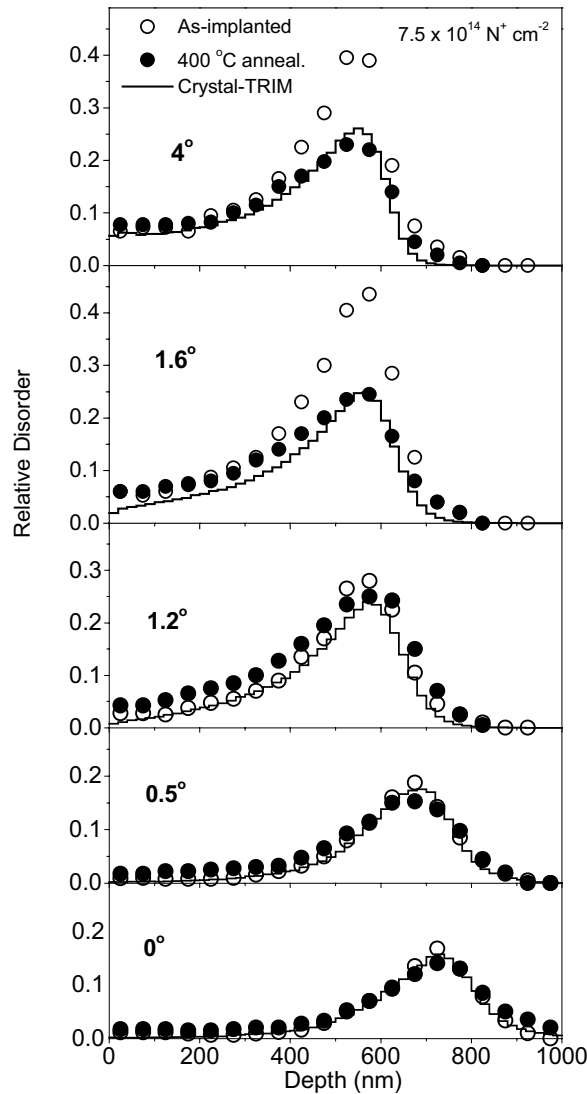


**Figure 7.19** The total relative disorder in the function of depth in 6H-SiC implanted with  $7.5 \times 10^{14} \text{ N}^+ \text{ cm}^{-2}$  at different tilts with respect to the  $c$ -axis. Solid/Open symbols: RBX evaluation of the BS/C spectra of as-implanted / 400 °C, 10 min. post-implantation annealed sample, Solid lines: Crystal-TRIM simulation. Labels in panel  $4^\circ$  apply to panels  $0^\circ$ ,  $0.5^\circ$ ,  $1.2^\circ$ , and  $1.6^\circ$ .

The residual relative disorder at the damage peak for both the Si and C sublattices, after annealing at different temperatures, was determined from BS/C experiments, and the results are shown in Fig. 7.20 for  $0^\circ$  and  $4^\circ$  tilts, respectively. The fractional recoveries at the damage peak (i.e., the ratio of the relative disorder reduction to the relative disorder present after irradiation at RT) after annealing at different temperatures are summarized in Table 7.3. After the first annealing step at 400 °C a reduction of 16 % can be observed in both sublattices for  $0^\circ$  tilt and a reduction of 52 % (40 %) occurs in the Si (C) sublattices for  $4^\circ$  tilt, respectively.

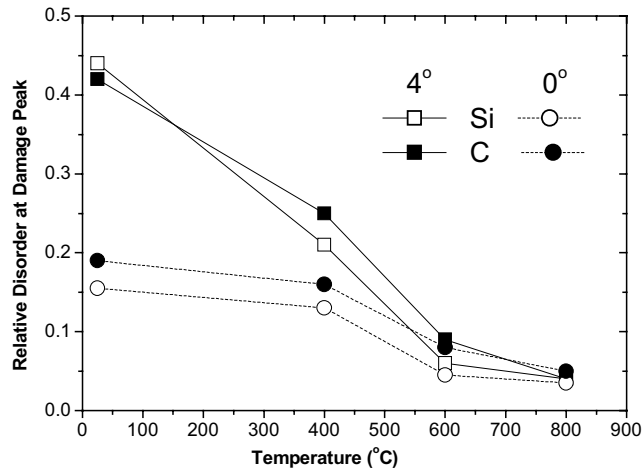


**Figure 7.20** Disorder recovery at the damage peak in both the Si and C sublattices of 6H-SiC, implanted with  $7.5 \times 10^{14} \text{ N}^+ \text{ cm}^{-2}$  at different tilts with respect to the *c*-axis and isochronally post-annealed at different temperatures for 10 min.

Annealing temperature (°C)	Fractional recovery at the damage peak (%)			
	0° tilt		4° tilt	
	Si	C	Si	C
400	16	16	52	40
600	55	42	34	38
800	4	7	4	12

**Table 7.3** Relative fractional recoveries at the damage peak in the Si and C sublattices of 6H-SiC implanted with  $7.5 \times 10^{14} \text{ N}^+ \text{ cm}^{-2}$  at different tilts with respect to the *c*-axis and sequentially annealed for 10 min. at different temperatures.

The different fractional recoveries indicate the changes in relative abundance of defect types from channeling to random implantation. Strong reduction of disorder occurs after a subsequent annealing at 600 °C with fractional Si (C) recoveries of 55 % (42 %) for 0° tilt and 34 % (38 %) for 4° tilt, respectively. Smaller fractions can be recovered after further annealing at 800 °C (Table 7.3). The annealing procedure ends up with residual disorder fractions of ~25 % and ~10 % for channeling and random implantation, respectively. However, the corresponding disorder levels, i.e.  $n_D$  values are about 0.04 each (Fig. 7.20). The somewhat lower fractional recovery in the C sublattice below 800 °C, followed by a higher fractional recovery in the C sublattice at 800 °C indicate the higher probability of complex defects and defect clusters present in the C sublattice. This is consistent with recent calculations [7.47] showing the aggregation of carbon interstitials to be energetically favored. The carbon clusters can possess higher thermal stability and therefore can be annealed out at elevated temperatures as compared to single carbon interstitials.

As Fig 7.20 shows, above 400 °C the annealing process is very similar for the 0° and 4° tilt implants. It seems that the majority of point defects and small clusters can be annealed out between 400-800 °C and some complex defects can survive even elevated temperatures.

### 7.3.9 Conclusions

I have performed a detailed investigation of damage accumulation in both sublattices of 6H-SiC in function of the implantation fluence and the orientation of the impinging N ions with respect to the  $\langle 0001 \rangle$  crystallographic axis using 3.55 MeV  $^4\text{He}^+$  backscattering spectrometry in combination with channeling. Firstly, for an adequate energy-depth conversion in the backscattering analysis, the electronic (average) stopping power for channeling direction has been determined for the analyzing He ions. Using Crystal-TRIM and the evaluation of BS/C measurement in both the Si and C sublattices of implanted SiC we found 0.8 times lower electronic stopping powers along the c-axis as compared to random direction.

I have shown that  $4^\circ/15^\circ$  tilt/rotation with respect to the c-axis enough to reach random implantation conditions. The influence of the ion fluence on the shape of the disorder profiles obtained by channeling implantation showed the presence of cascade overlap and the strong influence of implantation-induced disorder on the dechanneling of subsequently implanted ions already at relative disorder levels of 0.01. The detailed evaluation of the BS/C experiments show the presence of single point defects as dominant contributors to the implantation-induced disorder below a relative disorder level of  $\sim 0.2$ . Further accumulation of disorder is accompanied by the formation of strain and/or complex defects as reflected in excess dechanneling contributions. For high relative disorder levels ( $\sim 0.9$ ) it is also detected in significant surface swelling and in reduced introduction rate for strain. Amorphization of the material is reflected in decreasing C to Si disorder ratio rapidly approaching unity. The direct-impact, defect-stimulated phenomenological model for amorphization in SiC was used in the interpretation of damage build-up. The model showed that the role of stimulated amorphization is predominant in the amorphization process.

Crystal-TRIM well reconstructs the orientation dependence of both the shapes and heights of the measured damage distributions in most of the cases, however, at high damage levels the simulations deviate from the experimental results. The reason can be the formation of extended defect structures.

I found that the amount of damage in SiC can be significantly decreased by means of channeling implantation as compared to the case of random conditions. The efficiency is much higher at low fluences, before stimulated amorphization starts. The annealing of highly, but not totally disordered layers show the amorphous fraction to be recovered even at 400 °C, at lower temperature than required for point defect annealing. A higher amount of defect complexes is found in the C sublattice, however, neither the Si, nor the C sublattice can be totally recovered by annealing up to 800 °C.

In summary, both the mechanism of accumulation and thermal recovery of implantation-induced disorder along the  $\langle 0001 \rangle$  axial channel of 6H-SiC seem to be mostly affected by the actual disorder level and rather unaffected by the orientation of the ion beam.

In the scope of applications, significantly lower damage levels, achieved by channeling implantation, can decrease the probability to form dopant-defect related complexes during the irradiation or during post-implantation annealing. Since these complexes are expected to be electrically and optically inactive, they can significantly reduce the free carrier concentration and their reduction favours to accomplish the microelectronics application power of SiC.



## Summary

My contribution to the results and my conclusions presented in this thesis can be summarized in the following items:

1. I have studied the annealing behavior of the EI5 and EI6 centers in electron-irradiated p-type 4H-SiC by electron paramagnetic resonance (EPR). EI5 was previously attributed to the positively charged carbon vacancy at the cubic lattice site, whereas EI6 was correlated to the positively charged silicon antisite. I followed the EPR intensity of the hyperfine (HF) lines of the centers both with and without light illumination between room temperature and 1600 °C annealing.
  - a) Concerning the EI5 center, I have shown that the intensity change due to the change in the charge state of the defect may interfere with the intensity change due to the annealing of the defect. The HF lines of the center were still present after a 1350 °C anneal showing much higher thermal stability of the carbon vacancy than that previously reported [1].
  - b) I found that the annealing behavior of the EPR intensity of the EI6 center is similar to that for the EI5 center both with and without light illumination. Consequently – contrary to its previous identification – I proposed the EI6 center to be related to the positively charged carbon vacancy at the hexagonal lattice site of 4H-SiC [1].
2. I have identified the P6/P7 EPR centers in electron-irradiated 4H-SiC. I found four different spectra with the electron spin  $S = 1$ , two of them have  $C_{3v}$  symmetry (P6a,b) and the remaining two have  $C_{1h}$  symmetry (P7a,b). I analyzed the angular dependence of the spectra in the  $[11\bar{2}0]$  rotation plane of 4H-SiC. The  $g$  and  $D$  tensor parameters, the symmetry, and the correspondence between the number of spectra and the number of inequivalent lattice sites in 4H-SiC have confirmed that the P6a,b centers are related to the carbon vacancy–carbon antisite ( $V_C-C_{Si}$ ) pairs oriented along the  $c$ -axis and located at the cubic and hexagonal lattice sites of 4H-SiC, whereas P7a,b are also related to  $V_C-C_{Si}$  defects but are oriented along the other three tetrahedral bonding directions, respectively. I found that the annealing behavior of the P6/P7 centers in irradiated material confirms the theoretical calculations predicting the transformation of the Si vacancy into the  $V_C-C_{Si}$  pairs at elevated temperature [2].
3. I have detected the EPR spectrum of the  $T_{V2a}$  center in as-grown semi-insulating (SI) 4H-SiC grown by high-temperature chemical vapor deposition (HTCVD) in the absence of the EPR signal of the negatively charged silicon vacancy,  $V_{Si}^-$ . In my experiment the  $T_{V2a}$  spectrum with only two lines was detected. This argument, together with the results of previous Zeeman studies showing the nonsplitting of the photoluminescence (PL) zero phonon line of  $T_{V2a}$  confirm the spin  $S = 1$  of the center. Based on photo-EPR experiments I have concluded that the  $T_{V2a}$  spectrum arises from a triplet ground state and has a singlet excited state. I used this model to explain the origin of the associated PL line of the center by a radiative transition from the singlet excited state to the singlet sublevel of the triplet ground state [3].

4.
  - a) I have studied the disorder accumulation in 4H-SiC induced by 3.5 MeV He ions during backscattering spectrometry/channeling (BS/C) measurements. The disorder accumulation appears as a three-step process. In the first step at low fluence there is no additional disorder observed. The second step is an effective fluence region where the disorder level increases almost proportionally with fluence. I found fluence rate dependence of the near-surface damage in this stage of damage accumulation. In the third step the disorder level tends to saturation and does not approach amorphization as the fluence increases. The saturation can be due to extremely dilute collision cascade formation in the near-surface region during He irradiation. Based on these results, I have chosen optimal measurement fluence and fluence rate for 3.5 MeV He BS/C analysis in SiC [4].
  - b) I have determined the electronic stopping power for 3.5 MeV He ions along the  $\langle 0001 \rangle$  crystallographic axis of 6H-SiC in standard BS/C measurement conditions. I appointed that using 20 % lower (average) electronic stopping power for the  $\langle 0001 \rangle$  direction as compared to random direction an adequate energy-depth conversion in the evaluation of 3.5 MeV He BS/C spectra of the Si and C sublattices of SiC can be performed [8].
5. I applied the 3.5 MeV BS/C technique to measure the depth distribution of disorder in both the Si and C sublattices of 6H-SiC, irradiated with 200 keV Al ions to relatively low fluences along random direction at room temperature. All the implantation-induced relative disorder levels were below 0.2. Comparing the measured damage distributions to the results of SRIM computer simulations I have determined the effective displacement energies ( $E_d$ ) as a function of the implantation fluence both for the Si and C sublattices. I found in the applied fluence range  $E_d$  varying between 14.8 eV and 19.3 eV for the carbon sublattice and between 24.8 eV and 26.8 eV for the silicon sublattice, respectively [5].
6. Using 3.5 MeV He BS/C technique, I have determined the depth distribution of disorder, induced by 500 keV N implantation as a function of the fluence and the direction of irradiation with respect to the  $\langle 0001 \rangle$  crystallographic axis of 6H-SiC.
  - a) I have shown that the amount of damage can be significantly reduced by means of channeling implantation, especially at low fluences. I demonstrated that already a tilt angle of  $4^\circ$  relative to the  $\langle 0001 \rangle$  axis is equivalent to the random direction for implantation [6-8].
  - b) From BS/C spectrum analysis, profilometric measurements, computer simulations performed by the Crystal-TRIM code, and isochronal annealing experiments between room temperature and 800 °C I have concluded that the formation of disorder can be well described by the direct-impact, defect-stimulated amorphization model for SiC. The irradiation-induced disorder consists mainly of irradiation-induced point defects below a relative disorder level of about 0.2, whereas an amorphized fraction dominates damage build-up for higher disorder levels. The progress of disorder formation seems to depend only on the amount of nuclear energy deposited to Si and C target atoms for all of the applied initial orientations of the impinging N ions with respect to the crystallographic  $\langle 0001 \rangle$  axis [8].

## **Utilization of the new scientific results**

The results achieved by the use of electron paramagnetic resonance for the investigation of electron-irradiated SiC already led to a better understanding of formation and interaction of point defects. The findings are exploited in the control of processing of ion-implanted high power SiC diode and transistor structures.

The results obtained from the ion beam analytical study of ion implanted and annealed SiC are directly used in the tailoring of depth distribution of dopants and ion irradiation induced damage in SiC substrates in device processing.

The above research is conducted in collaboration with the Fraunhofer Institute for Integrated Systems and Devices FhG IISB, Erlangen.

## List of Publications

### This Ph.D. work is based on the following publications:

- [1] **Z. Zolnai**, N.T. Son, C. Hallin, and E. Janzén: Annealing behaviour of the carbon vacancy in electron-irradiated 4H-SiC, *Journal of Applied Physics* 96 (2004) p. 2406
- [2] **Z. Zolnai**, N. T. Son, B. Magnusson, C. Hallin, and E. Janzén: Annealing behaviour of vacancy- and antisite-related defects in electron-irradiated 4H-SiC, *Materials Science Forum* 457-460 (2004) p. 473
- [3] N.T. Son, **Z. Zolnai**, and E. Janzén: Silicon vacancy related  $T_{V2a}$  center in 4H-SiC, *Physical Review B* 68 (2003) p. 205211
- [4] N.Q.Khánh, **Z. Zolnai**, T. Lohner, L. Tóth, L. Dobos and J. Gyulai: He ion Beam Density Effect on Damage Induced in SiC During Rutherford Backscattering Measurement, *Nuclear Instruments and Methods in Physics Research B* 161-163 (2000) p. 424
- [5] **Z. Zolnai**, N.Q. Khánh, E. Szilágyi, E. Kótai, A. Ster, M. Posselt, T. Lohner, and J. Gyulai: Investigation of Ion Implantation Induced Damage in the Carbon and Silicon Sublattices of 6H-SiC, *Diamond and Related Materials* 11 (2002) p. 1239
- [6] **Z. Zolnai**, N.Q. Khánh, T. Lohner, A. Ster, E. Kótai, I. Vickridge, and J. Gyulai: Damage Distributions Induced by Channeling Implantation of Nitrogen into 6H Silicon Carbide, *Materials Science Forum* 433-436 (2003) p. 645
- [7] **Z. Zolnai**, A. Ster, N.Q. Khánh, E. Kótai, M. Posselt, G. Battistig, T. Lohner, and J. Gyulai: Ion Beam Analysis and Computer Simulation of Damage Accumulation in Nitrogen Implanted 6H-SiC: Effects of Channeling, *Materials Science Forum* 483-485 (2005) p. 637
- [8] **Z. Zolnai**, A. Ster, N.Q. Khánh, E. Kótai, M. Posselt, G. Battistig, T. Lohner, and J. Gyulai: Influence of crystallographic orientation and Ion Fluence on Damage Accumulation in Nitrogen Implanted 6H-SiC, manuscript for *Journal of Applied Physics*.

### Further publications related to the subject:

#### Journal papers:

- [9] T. Lohner, N.Q.Khánh, **Zs. Zolnai**: Spectroellipsometric Characterization of Ion Implanted Semiconductors and Ellipsometry, *acta physica slovacica*, Vol. 48 (1998) p. 441
- [10] E. Szilágyi, N.Q. Khánh, Z.E. Horváth, T. Lohner, G. Battisig, **Z. Zolnai**, E. Kótai and J. Gyulai: Ion Bombardment Induced Damage in Silicon Carbide Studied by Ion Beam Analytical Methods, *Materials Science Forum* 353-356 (2001) p. 271
- [11] N.T. Son, B. Magnusson, **Z. Zolnai**, A. Ellison, and E. Janzén: Defects in semi-insulating SiC substrates, *Materials Science Forum* 433-436 (2003) p. 45

- [12] E. Janzén, I. G. Ivanov, N. T. Son, B. Magnusson, **Z. Zolnai**, A. Henry, J. P. Bergman, L. Storasta and F. Carlsson: Defects in SiC, *Physica B* 334-342 (2003) p. 15
- [13] N.T. Son, B. Magnusson, **Z. Zolnai**, A. Ellison, and E. Janzén: Defects in high-purity semi-insulating SiC, *Materials Science Forum* 457-460 (2004) p. 437

**Conference papers:**

- [14] **Zolnai Zsolt**: Az MFA kutatási területei: Implantált SiC minták vizsgálata ionsugaras analízissel. Talk at the "Tavaszi szél 2000" meeting for young scientists and P.hD. students ( Apr 15, 2000, Szent István University, Gödöllő, Hungary), and in Abstract Book of the Conference
- [15] **Z. Zolnai**, N.Q. Khánh, E. Szilágyi, Z.E. Horváth, and T. Lohner: Native Oxide and Ion Implantation Damaged Layers on Silicon Carbide Studied by Ion Beam Analysis and Ellipsometry, Proc. " XV International Conference for Physics Students ICPS 2000" (Aug 4-11, 2000, Zadar, Croatia), <http://fizika.org/icps2000/sci/proc.html>
- [16] E. Szilágyi, E. Kótai, N.Q. Khánh, **Z. Zolnai**, G. Battistig, T.Lohner and J. Gyulai: Ion Implantation Induced Damage in Silicon Carbide Studied by Non-Rutherford Elastic Backscattering, Proc. 13<sup>th</sup> International Conference on Ion Implantation Technology, (Sept 17-22, 2000, Alpbach, Austria), IEEE (2001) p. 131
- [17] N.T. Son, B. Magnusson, **Z. Zolnai**, A. Ellison, and E. Janzén: Magnetic resonance of large-area semi-insulating SiC substrates, Proc. of the American Physical Society Meeting (Austin, Texas, USA; March 3-7, 2003) *Bulletin of The American Physical Society Meeting* **48** (2003) p. 1322

**Other publications:**

**Journal papers:**

- [18] P. Petrik, N. Q. Khánh, Z. E. Horváth, **Z. Zolnai**, I. Bársony, T. Lohner, M. Fried, J. Gyulai, C. Schmidt, C. Schneider and H. Ryssel: Characterisation of  $\text{Ba}_x\text{Sr}_{1-x}\text{TiO}_3$  films using spectroscopic ellipsometry, Rutherford backscattering spectrometry and X-ray diffraction, *Jornal of Non-Crystalline Solids* 303 (2002) p. 179
- [19] P. Petrik, N.Q. Khanh, Z.E. Horvath, **Z. Zolnai**, I. Barsony, T. Lohner, M.Fried, J. Gyulai, C. Schmidt, C. Schneider, H. Ryssel :Non-Destructive Characterisation of  $\text{SrBi}_2\text{Ta}_2\text{O}_9$  films, E-MRS Spring Meeting 2002, June 18-21, 2002, Strasbourg, France, *Materials Science in Semiconductor Processing* 5 (2002) p. 141
- [20] J. Balogh , I. Vincze, D. Kaptás, T. Kemény, T. Pusztai, L. F. Kiss, E. Szilágyi, **Z. Zolnai**, I. Kézsmárki, A. Halbritter, G. Mihály: Interface Magnetoresistance of Fe/Ag Multilayers, *physica status solidi (a)* 189 (2002) p. 621
- [21] D. Gogova, H. Larsson, R. Yakimova, **Z. Zolnai**, I. Ivanov, B. Monemar: Fast growth of high quality GaN, *physica status solidi (a)* 200 (2003) p. 13

**Conference papers:**

- [22] M. Serényi, Á. Nemcsics, J. Betko, **Zs. Zolnai**, N. Q. Khánh, Zs. J. Horváth: Sputtered a-SiGe:H layers for solar cell purposes Workshop on Solid State Surfaces and Interfaces II, SSSI-II, (2000 June 20-22, Bratislava, Slovakia) Book of Extended Abstracts p. 65
- [23] Zs. J. Horváth, M. Serényi, M. Ádám, B. Pődör, V. Rakovics, P. Turmezei, **Z. Zolnai**, I. Szabó, N. Q. Khánh: Vertical electrical transport in sputtered Al/a-SiGe/c-Si structures, 10th Joint Vacuum Conf., Sept. 28 - Oct. 2, 2004, Portoroz, Slovenia, Program and Book of Abstracts p. 123
- [24] Zs. J. Horváth, M. Serényi, M. Ádám, I. Szabó, V. Rakovics, P. Turmezei, **Z. Zolnai**, N. Q. Khánh: Electrical behaviour of sputtered Al/SiGe/Si structures, Solid State Surfaces and Interfaces IV, Nov. 8–11, 2004. Smolenice, Slovakia, Abstract Book p.16

**Number of independent citations**

The number of known independent citations is 18 until 8<sup>th</sup> of July 2005.

## Appendix 1

### Data evaluation in electron paramagnetic resonance

#### 1. Angular dependence measurements

In this section some details of the evaluation procedure from the measured data to the extracted spin Hamiltonian parameters of a paramagnetic center is briefly discussed.

Consider a  $x,y,z$  coordinate system which is identical to the principal axis system of the  $g$ -tensor of the studied EPR center. The axis of the external magnetic field  $\mathbf{B}$  in this system can be described with the angle  $\Theta$  between  $\mathbf{B}$  and the  $z$ -axis, and with the angle  $\varphi$  between the projection of  $\mathbf{B}$  in the  $xy$ -plane and the  $x$ -axis, respectively (see Fig. A1.1).

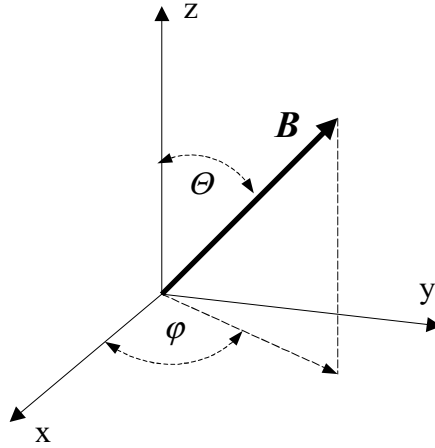


**Figure A1.1** Schematics of the coordinate system applied in the evaluation of spin Hamiltonian parameters from angular dependence measurements.

The  $g$ -value in a specific direction can be expressed with the principal  $g$ -values [A1.1]:

$$g = \sqrt{(g_x \sin \theta \cos \varphi)^2 + (g_y \sin \theta \sin \varphi)^2 + (g_z \cos \theta)^2} \quad (\text{A1.1})$$

For a spin  $S = 1$  center with axial symmetry  $g_x = g_y$ , and the anisotropic part of the fine structure parameter is  $E = (D_x - D_y)/2 = 0$ . Therefore it is no restriction to apply the magnetic field in the  $xz$ -plane (i.e.  $\varphi = 0$ ). Then the spin Hamiltonian of the center is given by [A1.1]:

$$H = \mu_B B (g_x S_x \sin \theta + g_z S_z \cos \theta) + D \left( S_z^2 - \frac{1}{3} S(S+1) \right) \quad (\text{A1.2})$$

Consider the case when  $g\mu_B B \gg D$  (Note, for the P6/P7 and  $T_{V2a}$  centers, discussed in this thesis, this assumption can be applied.). In this conditions the first order perturbation theory can be used to calculate the energy eigenvalues for the spin Hamiltonian in Equation A1.2. This procedure is resulted in the following formula [A1.1]:

$$E(M_S) = g\mu_B B M_S + \frac{1}{2} D \left[ \left( 3 \frac{g_z^2}{g^2} \cos^2 \theta - 1 \right) M_S^2 - \frac{1}{3} \left( 1 + \frac{g_z^2}{g^2} \cos^2 \theta \right) S(S+1) \right] \quad (\text{A1.3})$$

where  $E(M_S)$  denotes the energy eigenvalues of the system. The EPR transition from the state  $|M_S\rangle$  to  $|M_S + 1\rangle$  occur at the following magnetic field [A1.1]:

$$B = \frac{\hbar \omega}{g\mu_B} - \frac{D}{2g\mu_B} \left( 3 \frac{g_z^2}{g^2} \cos^2 \theta - 1 \right) (2M_S + 1) \quad (\text{A1.4})$$

From this it is seen that the transition is split into  $2S$  number of lines (i.e. into two branches for  $S = 1$ ) and the distance between them in the EPR spectrum is changing as the magnetic field is rotated. This so-called angular dependence pattern can be characterized by the spin Hamiltonian parameters:  $g$ , and  $D$ . In practice a discrete angular pattern is measured typically in  $5^\circ$  or  $10^\circ$  steps in the range  $0^\circ$ – $90^\circ$  for  $\theta$ . Then the parameters,  $g$  and  $D$  in Equation A1.4 are optimized with least square fits to the experimental data. Fig. A1.2 shows calculated angular dependence of the EPR transitions for a system characterized by Equation A1.2 with spin  $S = 1$ , an isotropic  $g$ -value of  $g = 2.0023$ , and fine structure parameter of  $D = 10^{-2} \text{ cm}^{-1}$  at microwave resonance frequency of  $\nu = 9.5 \text{ GHz}$ , respectively.

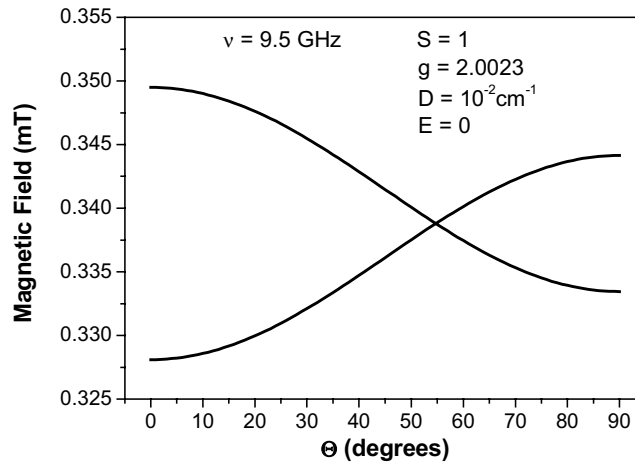


**Figure A1.2** Calculated angular dependence of the EPR transitions (magnitude of the resonant magnetic field) for a spin  $S = 1$  center with axial symmetry and an isotropic  $g$ -value of 2.0023 using a microwave excitation source with a frequency of  $\nu = 9.5 \text{ GHz}$ .

Note that during angular dependence measurements, which often require long data acquisition times the frequency of the microwave source varies to some small extent. This condition leads to the distortion of the measured angular dependence pattern. Therefore at each measurement step when the direction of the magnetic field is changed the (average) value of the frequency has to be stored. After the experiment has been completed, the resonant magnetic fields of the EPR transitions measured at different orientations of  $\mathbf{B}$  have to be calibrated to one fixed microwave frequency value. This can be done through Bohr's frequency condition, i.e. effective  $g$ -values for all of the transitions of the system measured at one fixed direction of  $\mathbf{B}$  can be expressed as  $g = \hbar \omega / \mu_B B$ , where  $\omega$  and  $B$  are the real



(average) frequency and resonance magnetic field, respectively. With these effective g-values all of the resonance field values can be calibrated through  $B_C = \hbar \omega_C / \mu_B g$ , where  $\omega_C$  is the fixed calibration frequency, and  $B_C$  is the calibrated resonance magnetic field, respectively. With this procedure the distortion of the angular dependence pattern is removed, and the fitting can be processed.

Another source of experimental error can be the inadequate calibration of the magnet. Usually the magnitude of the sweeping magnetic field  $B$  is controlled with the magnitude of the induction current in the magnet. This correlation has to be determined with satisfactory accuracy. A calibration of the magnet of the Bruker ER-200D X-band EPR spectrometer at IFM, Linköping University has been done in year 2002 and the correlation between the magnitudes of the nominal and real magnetic fields has been found to be as:

$$B_{real} = 1.00142 \times B_{nom} + 0.000112152 \text{ T} \quad (\text{A1.5})$$

This correction has been applied in the evaluation of EPR experiments presented in this thesis.

## 2. EPR spectrum simulation

An EPR spectrum of a paramagnetic center can be evaluated using appropriate computer programs. In this thesis EPR spectrum simulations in section 4.2 have been performed with the commercially available *WinEPR* software package [A1.2]. In this program three sets of parameters can be varied in order to simulate experimental spectra measured at a fixed orientation of the external magnetic field. Firstly, the instrument parameters, like microwave frequency, modulation amplitude, resolution (the number of channels in data acquisition), time constant and conversion time, center magnetic field and sweep width (the measurement window), and the order of the harmonic of the resonance signal (zero, first or second) can be considered as input parameters in the simulation. Secondly, the spin Hamiltonian parameters describing the EPR center can be given (the g-factor and the HF coupling constant). Mixtures of isotope spectra with their natural abundances giving rise to HF interaction with the paramagnetic electrons can be simulated using the database of *WinEPR*. The number of NN and NNN isotopes neighboring the paramagnetic center can be varied in the simulation. Therefore measured HF structures at a fixed sample orientation can be simulated. Thirdly, the line width and the line shape as Gaussian, Lorentzian, or a mixture of the two line shapes can be fitted. Further details about *WinEPR* can be found at Bruker's webpage (Ref. [A1.2]).

Note that *WinEPR* is still not appropriate to account for a number of physical parameters. For example, the phase of the output EPR signal as an additional information cannot be handled. However, other simulation programs have also been developed which can overcome a number of problems unsolved in *WinEPR*. For example, in the computer program, called *EPR*, developed by Antal Rockenbauer at the Chemical Research Center of the Hungarian Academy of Sciences in Budapest, the phase of EPR signals (mixing of absorption and dispersion signals) as well as the angular dependence of EPR spectra can be simulated. The program contains automatic parameter fitting procedure for liquid, solid single-crystalline or powder samples. Further details of the *EPR* program can be found in Ref. [A1.3].

## Appendix 2

### Mechanisms of Irradiation-Induced Amorphization in Ceramics: The Direct-Impact, Defect-Stimulated (D-I/D-S) Amorphization Model for SiC

The irradiation-induced crystalline-to-amorphous transformation in ceramics is of considerable interest, both fundamentally and technologically. Recently many different ceramic structures and composites are investigated and several different models have been developed to explain their amorphization process [A2.1].

In general, amorphization in ceramics should occur homogeneously or heterogeneously. Homogeneous amorphization is usually due to the progressive accumulation of point defects or one specific defect type. In this case amorphization may proceed spontaneously after a critical defect concentration is reached. It is shown in Fig. A2.1 as the defect accumulation model function. One example for such a process is quartz [A2.2].

However, ion irradiation leads to heterogeneous amorphization in a majority of ceramics. This process generally can be associated with a number of possible mechanisms, like direct-impact amorphization within individual collision cascades, the local accumulation of high defect concentrations during continued cascade overlap, or nucleation and growth of amorphous clusters in the material. Sometimes the combination of these processes takes place, such as direct-impact combined with cascade-overlap, or direct-impact combined with stimulated amorphization at crystalline/amorphous interfaces, as proposed for Si [A2.3] and SiC [A2.4], respectively. Fig. A2.1 shows the accumulated amorphous fraction,  $f_a$ , as a function of normalized fluence for different amorphization mechanisms.

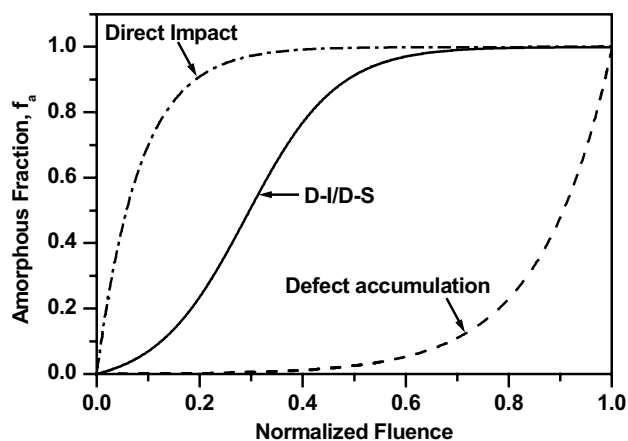


**Figure A2.1** Amorphous fraction as a function of normalized fluence for amorphization due to defect accumulation, direct-impact, and direct-impact/defect-stimulated (D-I/D-S) processes [A2.1].

To date several semi-empirical models have been suggested to explain the mechanisms associated with amorphization of SiC due to ion-irradiation. For a wide range of experiments, the accumulation of structural disorder and increase in amorphous fraction with fluence in SiC is consistent with and well described by the direct-impact, defect-stimulated

(D-I/D-S) model [A2.4]. In this model, the total disorder,  $S$ , produced under ion-beam irradiation and measured by ion-channeling methods consists of contributions from irradiation-induced amorphization, and irradiation-induced point defects and defect clusters in the residual crystalline regions. For low temperatures the expression for  $S$  is given by [A2.1]:

$$S = f_a + S_d \quad (\text{A2.1})$$

where  $f_a$  is the amorphous fraction and  $S_d$  is the relative disorder from irradiation-induced interstitials and small interstitial clusters in the residual crystalline regions. The term  $f_a$  can be well described by the D-I/D-S model. Here amorphous nuclei are directly produced in the core of a cascade and irradiation-induced point defects and/or subsequently implanted ions stimulate further amorphization at the crystalline-amorphous interfaces. If the probability for stimulated amorphization is taken as  $f_a(1 - f_a)$  than the differential change in  $f_a$ , due to an infinitesimal fluence,  $dD$  (expressed in displacements per atoms, dpa), can be written as:

$$df_a / dD = \sigma_a(1 - f_a) + \sigma_s f_a(1 - f_a) \quad (\text{A2.2})$$

where  $\sigma_a$  is the direct-impact amorphization cross-section, whereas  $\sigma_s$  is the effective cross-section for stimulated amorphization. The solution for the amorphous fraction is given by the expression [A2.1]:

$$f_a = 1 - (\sigma_a + \sigma_s) / \{ \sigma_s + \sigma_a \exp[(\sigma_a + \sigma_s)D] \} \quad (\text{A2.3})$$

This function will give a sigmodial-like accumulation of the amorphous fraction in SiC, see Fig. A2.1. Note that within the D-I/D-S model there must be some direct impact amorphization in order to reach complete amorphization, because otherwise  $f_a = 0$  if  $\sigma_a = 0$ .

Nevertheless, the ion irradiation in SiC primarily leads to the formation of Frenkel pairs in the residual crystalline material as proposed by molecular dynamics simulations [A2.5]. The contribution of these primary point defects to disorder can be expressed as [A2.6]:

$$S_d = S_d^* [1 - \exp(-BD)] (1 - f_a) \quad (\text{A2.4})$$

where  $S_d^*$  is the saturation level for the defect induced disorder observed, which is proportional to the local displacement rate, and  $B$  (dpa<sup>-1</sup>) is proportional to an effective recombination volume for the specific defects giving rise to  $S_d$ . Equation A2.4 is based on a simple defect accumulation model, which is consistent with the observed behavior for the accumulation of point defects in electron-irradiated 3C-SiC [A2.7], multiplied by the probability  $(1 - f_a)$  for a defect being produced in residual crystalline material.

## References

### Preface

- [P.1] J. Bardeen and W.H. Brattain, Phys. Rev. 74 (1948) 230.
- [P.2] W. Shockley, *Circuit Element Utilizing Semiconductor Material*, U.S. Patent 2569347 (1951)
- [P.3] G. L. Harris ed., *Properties of Silicon Carbide*, EMIS Datareviews Series No. 13, 1995
- [P.4] G.R. Hopkins and R.J. Price, Nucl. Eng. Des. /Fusion 2 (1985) 111.
- [P.5] B.G. Kim, Y. Choi, J.W. Lee, D.S. Sohn, and G.M. Kim, J. Nucl. Mater. 281 (2000) 163.
- [P.6] E. Janzén, I. G. Ivanov, N. T. Son, B. Magnusson, Z. Zolnai, A. Henry, J. P. Bergman, L. Storasta and F. Carlsson, Physica B 334-342 (2003) 15.
- [P.7] Carl-Mikael Zetterling ed., *Process Technology for Silicon Carbide Devices*, EMIS Processing Series No. 2, 2002
- [P.8] W. J. Weber, Nucl. Instrum. Methods Phys. Res. B 166-167 (2000) 98.

### Chapter 1

- [1.1] J.J. Berzelius, Ann. Phys. Lpz. 1 (1824) 169.
- [1.2] H. Moissan, Compt. Rend. Acad. Sci. Paris 140 (1905) 405.
- [1.3] E.G. Acheson, Engl. Patent 17911 (1892).
- [1.4] J.A. Lely, Bericht. Deutschen Keram. Ges. 32 (1955) 229.
- [1.5] Y. M. Tairov and V.F. Tsvetkov, J. Cryst. Growth 43 (1978) 209.
- [1.6] St. G. Müller, R.C. Glass, H.M Hobgood, V.F. Tsvetkov, M.Brady, D. Henshall, J.R. Jenny, D. Malta, and C.H. Carter Jr., J. Cryst. Growth 211 (2000) 325.
- [1.7] B.Harnisch, B. Kunkel, M. Deyerler, S. Bauereisen, and U. Papenberg, ESA Bulletin 95 (1998) 108.
- [1.8] X. Wang, K. Kato, K. Adachi, and K. Aizawa, Trib. Int. 36 (2003) 189.
- [1.9] R. H. Jones, L. Giancarli, A. Hasegawa, Y. Katoh, A. Kohyama, B. Riccardi, L.L. Snead, and W.J. Weber, J. Nucl. Mater. 307-311 (2002) 1057.
- [1.10] [www.iter.org](http://www.iter.org)
- [1.11] N.W. Ashcroft, and N.D. Mermin, *Solid State Physics*, Saunders College Publishing, 1976.
- [1.12] H. Morkoc, S. Strite, G. B. Gao, M.E. Lin, B. Sverdlov, and M. Burns, J. Appl. Phys. 76 (1994) 1363.
- [1.13] S. Strite, and H. Morkoc, J. Vac. Sci. Technol. B 10 (1992) 1237.
- [1.14] R. F. Davis, Proc. IEEE 79 (1991) 702.
- [1.15] A. Ellison, *Silicon Carbide Growth by High Temperature CVD Techniques*, Ph.D. Thesis No. 599, Linköping University, Linköping, Sweden, 1999.
- [1.16] W. von Münich, *Landolt-Brönstein: Numerical Data and Functional Relationships in Science and Technology* vol. 17, O. Madelung ed., Springer-Verlag, 1982.
- [1.17] T.P. Chow, Mat. Sci. Forum 338 – 342 (2000) 1155.
- [1.18] [www.ioffe.rssi.ru/SVA/NSM/Semicond](http://www.ioffe.rssi.ru/SVA/NSM/Semicond)
- [1.19] V.V. Afanas'ev, M. Bassler, G. Pensl, and M. Schulz, Phys. Stat. Sol. A 162 (1997) 321.

- [1.20] J.L. Cantin, H.J. von Bardeleben, Y. Shishkin, Y. Ke, R.P. Devaty, and W.J. Choyke, Phys. Rev. Lett. 92 (2004) 015502.
- [1.21] H.J. von Bardeleben, J.L. Cantin, L. Ke, Y. Shishkin, R.P. Devaty, and W.J. Choyke, Mater. Sci. Forum 483-485 (2005) 273.
- [1.22] A. Lloyd Spetz, L. Unéus, H. Svenningstorp, P. Tobias, L.-G. Ekedahl, O. Larsson, A. Göras, S. Savage, C. Harris, P. Mårtensson, R. Wigren, P. Salomonsson, B. Häggendahl, P. Ljung, M. Mattsson, and I. Ludström, Phys. Stat. Sol. A 185 (2001) 15.
- [1.23] E. Morvan, O. Noblanc, C. Dua, and C. Brylinski, Mater. Sci. Forum 353-356 (2001) 669.
- [1.24] [www.nichia.co.jp](http://www.nichia.co.jp)
- [1.25] [www.infineon.com](http://www.infineon.com)
- [1.26] G. L. Harris ed., *Properties of Silicon Carbide*, EMIS Datareviews Series No. 13, 1995
- [1.27] L. S. Ramsdell, Am. Mineralogist 32 (1947) 64.
- [1.28] F. Bechstedt, P. Käckell, A. Zywietz, K. Karch, B. Adolf, K. Tenelsen, and J. Furthmüller, Phys. Stat. Sol. B 202 (1997) 35.
- [1.29] W.J. Choyke, D.R. Hamilton, and L. Patrick, Phys. Rev. 133 (1964) A1163.
- [1.30] H. Iwata, *Stacking Faults in Silicon Carbide*, Ph.D. Thesis No. 817, Linköping University, Linköping, Sweden, 2003.
- [1.31] M.H. Hong, A.V. Samant, and P. Pirouz, Phil. Mag. A80 (2000) 919.
- [1.32] A. Ellison, B. Magnusson, C. Hemmingsson, W. Magnusson, T. Iakimov, L. Storasta, A. Henry, N. Henelius, and E. Janzén, MRS Symposium Proc. 640 (2001) H1.2.
- [1.33] D.H. Hoffmann, M.H. Müller, Mater. Sci. Eng. B61 – 62 (1999) 29.
- [1.34] O. Kordina, C. Hallin, A. Henry, J. P. Bergman, I. Ivanov, A. Ellison, N.T. Son, and E. Janzén, Phys. Stat. Sol. B 202 (1997) 321.
- [1.35] T. Kimoto, *Step-Controlled Epitaxial Growth of  $\alpha$ -SiC and Device Applications*, Ph.D. Thesis, Kyoto University, Japan, 1995.
- [1.36] O. Kordina, A. Henry, J. P. Bergman, N.T. Son, W.M. Chen, C. Hallin, and E. Janzén, Appl. Phys. Lett. 66 (1995) 1373.
- [1.37] H. Jacobson, *Structural Investigation and Lateral Growth of Silicon Carbide Crystals*, Ph.D. Thesis No. 789, Linköping University, Linköping, Sweden, 2002.
- [1.38] H.H. Woodbury and G.W. Ludwig, Phys. Rev. 124 (1961) 1083.
- [1.39] R.F. Davis and J.T. Glass, *Advances in Solid State Chemistry*, C.R.A. Catlow ed., Jai Press, 2 (1991) 1.
- [1.40] [www.hoya.co.jp](http://www.hoya.co.jp)
- [1.41] W.F. Knippenberg, *Philips Research Reports*, 18 (1963) 161.
- [1.42] Carl-Mikael Zetterling ed., *Process Technology for Silicon Carbide Devices*, EMIS Processing Series No. 2, 2002
- [1.43] K. Rüschemschmidt, H. Bracht, N.A. Stolwijk, M. Laube, G. Pensl, and G.R. Brandes, J. Appl. Phys. 96 (2004) 1458.
- [1.44] M. K. Linnarsson, M. S. Janson, J. Zhang, E. Janzén, and B. G. Svensson, J. Appl. Phys. 95 (2004) 8469.
- [1.45] Giber János, Gyulai József, Vargáné Josepovits Katalin, Bíró László Péter, *Diffúzió és implantáció szilárdtestekben*, Műegyetemi Kiadó, 1997

## Chapter 2

- [2.1] M. Ikeda, H. Matsunami, and T. Tanaka, Phys. Rev. B 22 (1980) 2842.
- [2.2] M. Bockstedte, M. Heid, and O. Pankratov, Phys. Rev. B 67 (2003) 193102.
- [2.3] H.A. Jahn and E. Teller, Proc. Roy. Soc. 161 (1937) 220.
- [2.4] W. Kohn, Solid State Phys. 5 (1957) 257.
- [2.5] L. Torpo, M. Marlo, T.E.M. Staab, and R.M. Nieminen, J. Phys.: Condens. Matter. 13 (2001) 6203.
- [2.6] R.N. Hall, Phys. Rev. 87 (1952) 387.
- [2.7] W. Shockley and W.T. Read, Phys. Rev. 87 (1952) 835.
- [2.8] H.G. Grimmeis, Ann. Rev. Mater. Sci. 7 (1977) 341.
- [2.9] A. Ellison, B. Magnusson, C. Hemmingsson, W. Magnusson, T. Iakimov, L. Storasta, A. Henry, N. Henelius, and E. Janzén, Mater. Res. Soc. Symp. 640 (2001) H1.2.
- [2.10] St. G. Müller, M.F. Brady, W.H. Brixius, G. Fechko, R.C. Glass, D. Henshall, H.McD. Hobgood, J.R. Jenny, R. Leonard, D. Malta, A. Powell, V.F. Tvestkov, S. Allen, J. Palmour, and C.H. Carter, Jr., Mat. Sci. Forum 389-393 (2002) 23.
- [2.11] F. Seitz and J.S. Koehler, in *Solid State Physics*, Vol. 2, F. Seitz and D. Turnbull ed., Academic Press, New York, 1956.
- [2.12] H. Hensel, and H.M. Urbassek, Nucl. Instrum. Methods Phys. Res. B 142 (1998) 287.
- [2.13] L. Pauling, *The Nature of the Chemical Bond*, Cornell University Press, Ithaca, New York, 1940.
- [2.14] L. Storasta, *Electrically Active Defects in 4H Silicon Carbide*, Ph.D. Thesis No. 801, Linköping University, Linköping, Sweden, 2003.
- [2.15] J.W. Steeds, F. Carosella, G.A. Evans, M.M. Ismail, L.R. Danks, and W. Voegli, Mater. Sci. Forum 353-356 (2001) 381.
- [2.16] A.L. Barry, B. Lehmann, D. Fritsch, and D. Bräunig, IEEE Trans. Nucl. Sci. 38 (1991) 1111.
- [2.17] H.J. von Bardeleben, J.L. Cantin, L. Henry, and M.F. Barthe, Phys. Rev. B 62 (2000) 10841.
- [2.18] R. Devanathan, W.J. Weber, and F. Gao, J. Appl. Phys. 90 (2001) 2303.
- [2.19] [www.physics.nist.gov/PhysRefData/Star/Text/](http://www.physics.nist.gov/PhysRefData/Star/Text/)
- [2.20] H.J. von Bardeleben, J.L. Cantin, I. Vickridge, and G. Battistig, Phys. Rev. B 62 (2000) 10126.
- [2.21] A. Matsunaga, C. Kinoshita, K. Nakai, and Y. Tomokiyo, J. Nucl. Mater. 179-181 (1991) 457.

## Chapter 3

- [3.1] W. Gerlach and O. Stern, Zeitschrift fur Phys. 8 (1922) 110.
- [3.2] C.J. Gorter, *Paramagnetic Relaxation*, Elsevier, Amsterdam, 1947.
- [3.3] J.H. van Vleck, *The Theory of Electric and Magnetic Susceptibilities*, Oxford University Press, 1932.
- [3.4] E. Zavoiski, J. Phys. USSR, 9 (1945) 211.
- [3.5] N.M. Atherton, *Principles of Electron Paramagnetic Resonance*, Ellis Horwood Limited, Chichester, England, 1993.
- [3.6] T. Umeda, J. Isoya, N. Morishita, T. Ohshima, and T. Kamiya, Phys. Rev. B 69 (2004) 121201(R).

- [3.7] R.G. Humphreys, D. Bimberg, and W.J. Choyke, J. Phys. Soc. Japan 49, Suppl. A (1980) 519.
- [3.8] R.G. Humphreys, D. Bimberg, and W.J. Choyke, Solid State Commun. 39 (1981) 163.
- [3.9] C. Persson and U. Lindefelt, J. Appl. Phys. 87 (1997) 5496.
- [3.10] R.P. Penrose, Nature 163 (1949) 992.
- [3.11] N.T. Son, P.N. Hai, and E. Janzén, Phys. Rev. Lett. 87 (2001) 045502.
- [3.12] N.T. Son, W.M. Chen, J.L. Lindström, B. Monemar, and E. Janzén, Mater. Sci. Eng. B61-62 (1999) 202.
- [3.13] J. Franck, Trans. Faraday Soc. 21 (1925) 536.
- [3.14] E.U. Condon, Phys. Rev. 32 (1928) 858.
- [3.15] H.J. von Bardeleben, J.L. Cantin, I. Vickridge, and G. Battistig, Phys. Rev. B 62 (2000) 10126.

## Chapter 4

- [4.1] N.T. Son, P.N. Hai, and E. Janzén, Phys. Rev. B 63, (2001) R201201.
- [4.2] V.Ya. Bratus, I.N. Makeeva, S.M. Okulov, T.L. Petrenko, T.T. Petrenko, and H.J. von Bardeleben, Mater. Sci. Forum 353-356 (2001) 517.
- [4.3] N.T. Son, B. Magnusson, and E. Janzén, Appl. Phys. Lett. 81 (2002) 3945.
- [4.4] L. Torpo, M. Marlo, T.E.M. Staab and R.M. Nieminen, J. Phys.: Condens. Matter 13 (2001) 6203.
- [4.5] A. Zywietz, J. Furthmüller, and F. Bechstedt, Phys. Rev. B 59 (1999) 15166.
- [4.6] A. Gali, P. Deák, N. T. Son, E. Janzén, H. J. von Bardeleben, and J. L. Monge, Mater. Sci. Forum (2003) 511.
- [4.7] M. Bockstedte, M. Heid, A. Mattausch, and O. Pankratov, Mater. Sci. Forum 389-393, (2002) 471, and Mater. Sci. Forum 433-436, (2003) 471.
- [4.8] M. Bockstedte, M. Heid, and O. Pankratov, Phys. Rev. B 67 (2003) 193102.
- [4.9] N.T. Son, P.N. Hai, and E. Janzén, Phys. Rev. Lett. 87 (2001) 045502.
- [4.10] C.C. Ling, C.D. Beling, and S. Fung, Phys. Rev. B 62 (2000) 8016.
- [4.11] E. Rauls, Th. Frauenheim, A. Gali, and P. Deák, Phys. Rev. B 68 (2003) 155208.
- [4.12] N.T. Son, P.N. Hai, and E. Janzén, Mater. Sci. Forum 353-356 (2001) 499.
- [4.13] H. Itoh, A. Kawasuso, T. Ohshima, M. Yoshikawa, I. Nashiyama, S. Tanigawa, S. Misawa, H. Okumura, and S. Yoshida, Phys. Stat. Sol. (a) 162 (1997) 173.
- [4.14] Th. Lingner, S. Greulich-Weber, J.-M. Spaeth, U. Gerstmann, E. Rauls, Z. Hajnal, Th. Frauenheim, and H. Overhof: Phys. Rev. B 64 (2001) 245212.
- [4.15] V.Ya. Bratus, I.N. Makeeva, S.M. Okulov, T.L. Petrenko, T.T. Petrenko, and H.J. von Bardeleben, Physica B 308-310 (2001) 621.
- [4.16] T. Umeda, J. Isoya, N. Morishita, T. Ohshima, and T. Kamiya, Phys. Rev. B 69 (2004) 121201(R).
- [4.17] A. Ellison, B. Magnusson, N.T. Son, L. Storasta, and E. Janzén, Mater. Sci. Forum 433-436 (2003) 33.
- [4.18] N.M. Pavlov, M.I. Iglitsyn, M.G. Kosaganova, and V.N. Solomatin, Sov. Phys. Semicond. 9 (1976) 845.
- [4.19] V.S. Vainer and V.A. Il'in, Fiz. Tverd. Tela (Leningrad) 23, (1981) 3659 [Sov. Phys. Solid State 23 (1981) 2126].
- [4.20] N.T. Son, Mt. Wagner, E. Sörman, W.M. Chen, B. Monemar, and E. Janzén; Semicond. Sci. Technol. 14 (1999) 1141.
- [4.21] E. Rauls, Th. Lingner, Z. Hajnal, S. Greulich-Weber, Th. Frauenheim, and J.-M.

- Spaeth, Phys. Stat. Sol. (b) 217 (2000) R1.
- [4.22] W.E. Carlos, E.R. Glaser, B.V. Shanabrook, and T.A. Kennedy, in *Proceedings of APS Meeting*, Austin, Texas, March 2003, Bull. Am. Phys. Soc. 48 (2003) 1322.
  - [4.23] E. Sörman, N.T. Son, W.M. Chen, O. Kordina, C. Hallin, and E. Janzén, Phys. Rev. B 61 (2000) 2613.
  - [4.24] N. Mizuochi, J. Isoya, S. Yamasaki, H. Takizawa, N. Morishita, T. Ohshima, and H. Itoh, Mater. Sci. Forum 389-393 (2002) 497.
  - [4.25] S. B. Orlinski, J. Schmidt, E. N. Mokhov, and P. G. Baranov, Phys. Rev. B 67 (2003) 125207.
  - [4.26] H. J. von Bardeleben, J. L. Cantin, I. Vickridge, and G. Battistig, Phys. Rev. B 62 (2000) 10126.
  - [4.27] Mt. Wagner, B. Magnusson, W. M. Chen, and E. Janzén, Phys. Rev. B 62 (2000) 16555.
  - [4.28] N. Mizuochi, J. Isoya, S. Yamasaki, H. Takizawa, N. Morishita, T. Ohshima, and H. Itoh, Phys. Rev. B 66 (2002) 235202.
  - [4.29] Mt. Wagner, N. Q. Thinh, N. T. Son, P. G. Baranov, E. N. Mokhov, C. Hallin, W. M. Chen, and E. Janzén, Mater. Sci. Forum 389-39, (2002) 501.
  - [4.30] Mt. Wagner, N. Q. Thinh, N. T. Son, P. G. Baranov, E. N. Mokhov, C. Hallin, W. M. Chen, and E. Janzén, Phys. Rev. B 66 (2002) 155214.
  - [4.31] T. Wimbauer, B. K. Meyer, A. Hofstaetter, A. Scharmann, and H. Overhof, Phys. Rev. B 56 (1997) 7384.
  - [4.32] J. Schneider and K. Maier, Physica B 185, (1993) 199.
  - [4.33] Th. Lingner, S. Greulich-Weber, and J. -M. Spaeth, Physica B 308-310, (2001) 649.
  - [4.34] A. Ellison, B. Magnusson, N. T. Son, L. Storasta, and E. Janzén, Mater. Sci. Forum 433-436 (2003) 33.
  - [4.35] N. T. Son, B. Magnusson, Z. Zolnai, A. Ellison, and E. Janzén, Mater. Sci. Forum 433-436 (2003) 45.

## Chapter 5

- [5.1] J.R. Tesmer and M. Nastasi, *Handbook of Modern Ion Beam Materials Analysis*, MRS. Pittsburgh, 1995.
- [5.2] S.T. Thornton and A. Rex, *Modern Physics for Scientists and Engineers*, Saunders College Publishing, 1993.
- [5.3] J.P. Biersack and L.G. Haggmark, Nucl. Instrum. Methods 174 (1980) 257.
- [5.4] A. Simionescu, S. Herzog, G. Hobler, R. Schork, J. Lorenz, C. Tian, and G. Stinger, Nucl. Instrum. Methods Phys. Res. B 100 (1995) 483.
- [5.5] M. Posselt, L. Bischoff, J. Teichert, and A. Ster, J. Appl. Phys. 93 (2003) 1004.
- [5.6] F. Gao, and W.J. Weber, Phys. Rev. B 63 (2000) 054101.
- [5.7] W. Jiang, C.M. Wang, W.J. Weber, M.H. Engelhard, and L.V. Saraf, J. Appl. Phys 95 (2004) 4687.
- [5.8] W.J. Weber, Nucl. Instrum. Methods Phys. Res. B 166-167 (2000) 98.
- [5.9] F. Gao, and W.J. Weber, Phys. Rev. B 66 (2002) 024106.
- [5.10] J. Lindhard, Mat. Fys. Medd. Dan. Vid. Selsk. 34 (1965) 1.
- [5.11] J. H. Barrett, Phys. Rev. B 3 (1971) 1527.
- [5.12] L. C. Feldman, J.M. Mayer, and S.T. Picraux, *Materials Analysis by Ion Channeling*, Academic Press, New York, 1982.
- [5.13] L. Mayer, Phys. Status Solid. 44 (1971) 253.
- [5.14] P. Sigmund and W.K. Winterbon, Nucl. Instrum. Methods 119 (1974) 541.



- [5.15] J.F. Ziegler, J.P. Biersack, and U. Littmark, *The Stopping and Range of Ions in Matter*, Pergamon Press, New York, 1985.
- [5.16] <http://www.srim.org>
- [5.17] J.H.R. dos Santos, P.L. Grande, M. Behar, H. Boudinov, and G. Schiwietz, Phys. Rev. B 55 (1997) 4332.
- [5.18] G. de M. Avezedo, J.R.A. Kaschny, J.F. Dias, P.L. Grande, M. Behar, Ch. Klatt, and S. Kalbitzer, Nucl. Instrum. Methods Phys. Res. B 148 (1999) 168.
- [5.19] O.S. Oen and M.T. Robinson, Nucl. Instrum. Methods 132 (1976) 647.
- [5.20] M. Posselt, Radiat. Eff. and Defects in Solids 130-131 (1994) 87.
- [5.21] A. Ster, M. Posselt, A. Hallén, and M. Janson, Proc. 2000 International Conference on Ion Implantation Technology (IEEE, Piscataway, NJ, 2000) 220.

## Chapter 6

- [6.1] R.J. van de Graaff, Phys. Rev. 38 (1931) 1919A.
- [6.2] F. Pászti, A. Manuaba, C. Hajdu, A.A. Melo, and M.F. Da Silva, Nucl. Instrum. Methods B 47 (1990) 187.
- [6.3] J.R. Tesmer and M. Nastasi, *Handbook of Modern Ion Beam Materials Analysis*, MRS. Pittsburgh, 1995.
- [6.4] E. Szilágyi, F. Pászti, and G. Amsel, Nucl. Instrum. Methods B 100 (1995) 103.
- [6.5] M. K. Leung, Ph.D. dissertation (1972) Univ. of Kentucky
- [6.6] Y. Feng, Z. Zhou, Y. Zhou, and G. Zhou, Nucl. Instrum. Methods B 86 (1994) 225.
- [6.7] E. Szilágyi, E. Kótai, N.Q. Khanh, Z. Zolnai, G. Battistig, T. Lohner, and J. Gyulai, Proc. 2000 International Conference on Ion Implantation Technology (IEEE, Piscataway, NJ, 2000) 131.
- [6.8] W. Jiang, W. J. Weber, S. Thevuthasan, D. E. McCready, Nucl. Instrum. Methods B 161-163 (2000) 501.
- [6.9] I. Nashiyama, T. Nishijima, E. Sakuma, S. Yoshida, Nucl. Instrum. Methods B 33 (1988) 599.
- [6.10] J. Lindhard, M. Scharff, Mat. Fys. Medd. Dan. Vid. Selsk. 27 (1953) 15.
- [6.11] W.K. Chu, Phys. Rev. A13 (1976) 2057.
- [6.12] P. Sigmund and W.K. Winterbon, Nucl. Instrum. Methods 119 (1974) 541.
- [6.13] M. Hofmann, A. Zywiets, K. Karch, and F. Bechstedt, Phys. Rev. B 50 (1994) 13401.
- [6.14] M. Posselt, Radiat. Eff. and Defects in Solids 130-131 (1994) 87.
- [6.15] E. Kótai, Nucl. Instrum. Methods B 85 (1994) 588; and E.Kótai, Proc. 14<sup>th</sup> Int. Conf. on Appl. Accelerators in Res. Ind. Nov 6-9, 1996, Denton, Texas USA, (AIP Press, New York 1997, J.L. Duggan and I.L. Morgan ed.) 631.
- [6.16] D. Schroyen, M. Bruggeman, I. Dézsi, and G. Langouche, Nucl. Instrum. Methods B 15 (1986) 341.

## Chapter 7

- [7.1] J. Gyulai, F. Pászti, and E. Szilágyi, Nucl. Instrum. Methods B 106 (1995) 328.
- [7.2] P. Musumeci, G. Calcagno, M.G. Grimaldi, and G. Foti, Nucl. Instrum. Methods B 116 (1996) 327.
- [7.3] V. Heera, J. Stoemenos, R. Koegler, and W. Skorupa, J. Appl. Phys. 77 (1995) 2999.
- [7.4] W. Fukarek, R. A. Yankov, W. Anwand, and V. Heera, Nucl. Instrum. Methods B 142 (1998) 561.

- [7.5] M.G. Grimaldi, L. Calcagno, P. Musumeci, N. Frangis, and J. Van Landuyt, *J. Appl. Phys.* 81 (1997) 7181.
- [7.6] M. Bruel, *Electron. Lett.* 31 (1995) 1201.
- [7.7] A. Agarwal, T.E. Haynes, V.C. Venezia, O.W. Holland, and D.J. Eaglesham, *Appl. Phys. Lett.* 72 (1998) 1086.
- [7.8] T. Lohner, M.A. Sherbiny, N.Q. Khanh, M. Fried, H. Wormeester, and J. Gyulai, *Proc. Ninth Int. Conf. Ion Beam Mod. Mater. (IBMM '95)*, Canberra, Australia (1995) 797.
- [7.9] E. Kótai, *Nucl. Instrum. Methods B* 85 (1994) 588; and E.Kótai, *Proc. 14<sup>th</sup> Int. Conf. on Appl. Accelerators in Res. Ind. Nov 6-9, 1996, Denton, Texas USA*, (AIP Press, New York 1997, J.L. Duggan and I.L. Morgan ed.) 631.
- [7.10] R. Nipoti, E. Albertazzi, M. Bianconi, R. Lotti, G. Lulli, M. Cervera, A. Carnera, *Appl. Phys. Lett.* 70 (1997) 3425.
- [7.11] W. Jiang, W.J. Weber, S. Thevuthasan, D.E. McCready, *Nucl. Instrum. Methods B* 148 (1999) 562.
- [7.12] A. Matsunaga, C. Kinoshita, K. Nakai, and Y. Tomokiyo, *J. Nucl. Mater.* 179-181 (1991) 457.
- [7.13] F. Gao, and W.J. Weber, *Phys. Rev. B* 66 (2002) 024106.
- [7.14] R. Devanathan, W.J. Weber, and F. Gao, *J. Appl. Phys.* 90 (2001) 2303.
- [7.15] N.Q. Khanh, Z. Zolnai, T. Lohner, L. Tóth, L. Dobos, and J. Gyulai, *Nucl. Instrum. Methods B* 161-163 (2000) 424.
- [7.16] F. Pászti, A. Manuaba, C. Hajdu, A.A. Melo, and M.F. Da Silva, *Nucl. Instrum. Methods B* 47 (1990) 187.
- [7.17] W. Jiang, W.J. Weber, S. Thevuthasan, and D.E. McCready, *Nucl. Instrum. Methods B* 161-163 (2000) 501.
- [7.18] M. Laube, F. Schmid, G. Pensl, and G. Wagner, *Mat. Sci. Forum* 389-393 (2001) 791.
- [7.19] D. Åberg, A. Hallén, P. Pellegrino, and B. G. Svensson, *Appl. Phys. Lett.* 78 (2001) 2908.
- [7.20] U. Gerstmann, E. Rauls, Th. Frauenheim, and H. Overhof, *Phys. Rev. B* 67 (2003) 205202.
- [7.21] J. Wong-Leung, M. S. Janson, and G. B. Svensson, *J. Appl. Phys.* 93 (2003) 8914.
- [7.22] E. Morvan, N. Mestres, F.J. Campos, J. Pascual, A. Hallén, M. Linnarson and A.Yu. Kuznetsov, *Mat. Sci. Forum* 338-342 (2000) 893.
- [7.23] M.S. Janson, A. Hallén, P. Godignon, A.Yu Kuznetsov, M.K. Linnarson, E. Morvan, and B.G. Svensson, *Mat. Sci. Forum* 338-342 (2000) 889.
- [7.24] M.S. Janson, J. Slotte, A.Yu Kuznetsov, K. Saarinen, and A. Hallén, *J. Appl. Phys.* 95 (2004) 57.
- [7.25] S. Ahmed, C.J. Barbero, T.W. Sigmon, and J.W. Erickson, *J. Appl. Phys.* 77 (1995) 6194.
- [7.26] M. Posselt, *Radiat. Eff. and Defects in Solids* 130-131 (1994) 87.
- [7.27] A. Ster, M. Posselt, A. Hallén, and M. Janson, *Proc. 2000 International Conference on Ion Implantation Technology (IEEE, Piscataway, NJ, 2000)* 220.
- [7.28] M.-A. Nicolet, H.R. Bilger, and O. Meyer, *Phys. Stat. Sol. (a)* 3 (1970) 1019.
- [7.29] A. Zywiets, K. Karch, and F. Bechstedt, *Phys. Rev. B* 54 (1996) 1791.
- [7.30] Y. Feng, Z. Zhou, Y. Zhou, and G. Zhou, *Nucl. Instrum. Methods B* 86 (1994) 225.
- [7.31] M. K. Leung, *Ph.D. dissertation (1972) Univ. of Kentucky*

- [7.32] W. Jiang, C.M. Wang, W.J. Weber, M.V. Engelhard, and L.V. Saraf, J. Appl. Phys. (2004) 4687.
- [7.33] Y. Zhang, and W.J. Weber, Appl. Phys. Lett. 83 (2003) 1665.
- [7.34] M. Kokkoris, S. Kossionides, R. Vlastou, X.A. Aslanoglou, R. Grötzschel, B. Nsouli, A. Kuznetsov, S. Petrovic, and Th. Paradellis, Nucl. Instrum. Methods Phys. Res. B 184 (2001) 319.
- [7.35] A. Simionescu, S. Herzog, G. Hobler, R. Schork, J. Lorenz, C. Tian, and G. Stinger, Nucl. Instrum. Methods Phys. Res. B 100 (1995) 483.
- [7.36] K. Rüschemschmidt, H. Bracht, N.A. Stolwijk, M. Laube, G. Pensl, and G.R. Brandes, J. Appl. Phys. 96 (2004) 1458.
- [7.37] Z. Zolnai, N. T. Son, C. Hallin, and E. Janzén, J. Appl. Phys. 96 (2004) 2406.
- [7.38] H. Itoh, A. Kawasuso, T. Ohshima, M. Yoshikawa, I. Nashiyama, S. Tanigawa, S. Misawa, H. Okumura, and S. Yoshida, Phys. Stat. Sol. (a) 162 (1997) 173.
- [7.39] W. Jiang, and W. J. Weber, Phys. Rev. B 64 (2001) 125206.
- [7.40] Y. Zhang, W.J. Weber, W. Jiang, V. Shutthanandan, S. Thevuthasan, M. Janson, and A. Hallén, Nucl. Instrum. Methods Phys. Res. B 219-220 (2004) 647.
- [7.41] F. Gao, and W.J. Weber, Phys. Rev. B 66 (2002) 024106.
- [7.42] L. Storasta, *Electrically Active Defects in 4H Silicon Carbide*, Ph.D. Thesis No. 801, Linköping University, Linköping, Sweden, 2003.
- [7.43] H.J. von Bardeleben, J.L. Cantin, L. Henry, and M.F. Barthe, Phys. Rev. B 62 (2000) 10841.
- [7.44] Y. Zhang, W.J. Weber, W. Jiang, C.M. Wang, V. Shutthanandan, and A. Hallén, J. Appl. Phys. 95 (2003) 4012.
- [7.45] E. Wendler, A. Heft, W. Wesch, G. Peiter, H.H. Dunken, Nucl. Instrum. Methods Phys. Res. B 127/128 (1997) 341.
- [7.46] C. Calcagno, M.G. Grimaldi, P. Musumeci, J. Mat Res. 12 (1997) 1727.
- [7.47] A. Gali, P. Deák, P. Ordejón, N. T. Son, E. Janzén, and W. J. Choyke, Phys. Rev. B 68 (2003) 125201.

## Appendix 1

- [A1.1] P. Emanuelsson, *Electron Paramagnetic Resonance Studies on Defects in Silicon*, Ph.D. Thesis, University of Lund, Lund, Sweden, 1991.
- [A1.2] <http://www.bruker-biospin.com/brukerepr/winepr.html>
- [A1.3] A. Rockenbauer, and L. Korecz, Applied Magn. Resonance 10 (1996) 29.

## Appendix 2

- [A2.1] W.J. Weber, Nucl. Instrum. Methods Phys. Res. B 166-167 (2000) 98.
- [A2.2] M.R. Pascucci, J.L. Hutchison, and L.W. Hobbs, Radiat. Eff. 74 (1983) 219.
- [A2.3] N. Hecking, K.F. Heidemann, and E. te Kaat, Nucl. Instrum. Methods B 15 (1986) 760.
- [A2.4] E. Wendler, A. Heft, and W. Wesch, Nucl. Instrum. Methods Phys. Res. B 141 (1998) 105.
- [A2.5] F. Gao, and W.J. Weber, Phys. Rev. B 66 (2002) 024106.
- [A2.6] Y. Zhang, W.J. Weber, W. Jiang, C.M. Wang, V. Shutthanandan, and A. Hallén, J. Appl. Phys. 95 (2003) 4012.
- [A2.7] A. Matsunaga, C. Kinoshita, K. Nakai, and Y. Tomokiyo, J. Nucl. Mater. 179-181 (1991) 457.

## List of used acronyms

BS	– Backscattering Spectrometry
BS/C	– Backscattering Spectrometry combined with Channeling
CVD	– Chemical Vapor Deposition
D-I/D-S	– Direct-Impact, Defect-Stimulated
DLTS	– Deep Level Transient Spectroscopy
EELS	– Electron Energy Loss Spectroscopy
EMT	– Effective Mass Theory
EPR	– Electron Paramagnetic Resonance
HF	– Hyperfine
HPSI	– High-Purity Semi-Insulating
HTCVD	– High Temperature Chemical Vapor Deposition
ITER	– International Thermonuclear Experimental Reactor
LPE	– Liquid Phase Epitaxy
MCDA	– Magnetic Circular Dichroism of Absorption
MCDA-EPR	– MCDA-detected Electron Paramagnetic Resonance
MD	– Molecular Dynamics
MESFET	– Metal-Semiconductor Field-Effect Transistor
MOSFET	– Metal-Oxide-Semiconductor Field-Effect Transistor
MS	– Multiple Scattering
MW	– Microwave
NN	– Nearest Neighbor
NNN	– Next Nearest Neighbor
ODMR	– Optically Detected Magnetic Resonance
PKA	– Primary-Knock-On Atom
PL	– Photoluminescence
PVT	– Physical Vapor Transport
RBS	– Rutherford Backscattering Spectrometry
r.m.s.	– root-mean-square
RT	– Room Temperature
SI	– Semi Insulating
SIMS	– Secunder Ion Mass Spectroscopy
SRIM	– Stopping and Range of Ions in Matter
TRIM	– Transport of Ions in Matter
XPS	– X-ray Photoelectron Spectroscopy
VPE	– Vapor Phase Epitaxy
ZBL	– Ziegler-Biersack-Littmark
ZFS	– Zero-Field Splitting
ZPL	– Zero-Phonon Line

## Acknowledgements

Financial support of the OTKA grants No. T030441, T025928, T034332, and of the EU project Marie Curie Training Sites is gratefully appreciated.

I would like to express my thanks to all the people whose contribution was indispensable for the completion of the work presented in this thesis.

- My supervisor, Dr. Tivadar Lohner for overall guiding and support, manuscript reading and corrections, as well as for help in organizing and official work.
- Prof. Peter Deák, Prof. József Gyulai, Dr. István Bársony, and Dr. György Hárs for the encouragement, continuous support, and that they provided good conditions for work.
- My colleague, Nguyen Quoc Khanh, whose help in backscattering spectrometry measurements and spectrum analysis was indispensable. Also the ion beam analysis and characterization group: Gábor Battistig, Edit Szilágyi, Endre Kótai, Zoltán Hajnal, Ferenc Pásztí, and Manuaba Asrama, for introducing me to ion beam techniques, and for helpful discussions.
- My colleague, András Ster and Dr. Matthias Posselt at Forschungszentrum, Rossendorf in Germany for the Crystal-TRIM code. Their work and cooperation was essential to perform computer simulation of the ion implantation process.
- The accelerator staff for operating de Van de Graaff generator and the Heavy Ion Cascade Implanter.
- The cleanroom personnel for cutting, chemical cleaning and annealing of samples, and their help in optical microscopy and profilometric measurements.
- The Groupe de Physique des Solides at Jussieu University in Paris, especially Ian Vickridge, H. Jurgen von Bardeleben, and Jean-Louis Cantin for kind hospitality and fruitful discussions.
- Prof. Bo Monemar and Prof. Erik Janzén at Linköping University in Sweden for the opportunity to spend one year at the SiC group.
- Many thanks to Dr. Nguyen Tien Son, my co-supervisor in Linköping, who has introduced me to EPR and related techniques and having helped me many ways during my stay, even at the cost of his free time.
- Thanks to my parents, sisters, and my best friends for the appreciation, patience and their support during the hard periods.